

Politecnico di Torino

ScuDo
Scuola di Dottorato ~ Doctoral School
WHAT YOU ARE, TAKES YOU FAR

Doctoral Dissertation
Doctoral Program in Energy Engineering (37^{th}cycle)

Runaway Electron termination dynamics in fusion plasmas

By

Lovepreet Singh

******

Supervisor(s):
Prof. F. Subba, Supervisor
Dr. D. Grasso, Co-Supervisor
Dr. D. Borgogno,Co-Supervisor

Doctoral Examination Committee:
Dr. E. Nardon, Referee, CEA Cadarache, France
Dr. M. Siccinio, Referee, EUROfusion Consortium, Germany
Prof. S. Dulla, Politecnico di Torino, Italy
Prof. M. Magali, Aix-Marseille Universitè, France
Dr. A. Tinguely, MIT, USA

Politecnico di Torino
2024

Declaration

I hereby declare that, the contents and organization of this dissertation constitute my own original work and does not compromise in any way the rights of third parties, including those relating to the security of personal data.

Lovepreet Singh
2024

* This dissertation is presented in partial fulfillment of the requirements for **Ph.D. degree** in the Graduate School of Politecnico di Torino (ScuDo).

To my family

Acknowledgements

I sincerely thank my supervisors, Dr. Dario Borgogno, Dr. Daniela Grasso, and Prof. Fabio Subba, for the opportunity to embark on a PhD focused on the fascinating field of Runaway electrons. Their mentorship has been invaluable, not only for the academic expertise they provided but also for their encouragement and unwavering support. I owe a special thanks to Dario and Daniela, whose office became my second home during countless days of deep discussion and exploration. Their knowledge and patience have been my guiding lights, and I am immensely grateful for the countless insights and advice they shared — both in research and in life. I am sure that as this journey comes to an end, they will feel my absence the most

I am also grateful to the JOREK community and NEMO group members, whose support has been essential for completing many of my research tasks. Their readiness to assist and share their knowledge has enriched my work and fostered a sense of collaboration and growth.

My heartfelt thanks go to my parents, who have been my silent pillars throughout this journey. To my sister, whose lighthearted conversations helped me step away from research to enjoy real-life moments, like our occasional dinner outings. And to my wife, who has been endlessly patient and understanding, even when work kept me busy on special days like her birthday (our first after marriage) — thank you for your love and support. Your sacrifices have not gone unnoticed, and I am deeply grateful for the strength you have given me.

Finally, I extend my gratitude to all my friends, especially Chiara, and my colleagues, who have each, in their own way, made this journey memorable and fulfilling. Thank you for your encouragement, companionship, and motivation that kept me going during challenging times.

Abstract

The presence of runaway electrons (RE) poses a significant challenge to the operation of tokamak fusion reactors. These high-energy particles can reach the surrounding walls and cause irreparable damage upon collision with tokamak components. To address this issue, the fusion community is exploring various mitigation techniques. However, the full impact of these mitigation strategies on the RE population and the background plasma is not yet fully understood. For instance, an SPI technique is utilized to suppress the RE generation by rapidly increasing plasma density and cooling it down in current reactors. In certain scenarios, the SPI injection can trigger bursts of plasma magnetohydrodynamic (MHD) activity. Among these activities, magnetic reconnection (MR) plays a crucial role. This instability is driven by the presence of RE, whose characteristics, in turn, are significantly affected by the topological changes (formation of magnetic island) in the plasma magnetic field. Understanding this mutual influence is crucial for developing strategies to ensure the safe termination of RE. Moreover, the behavior of the first wall materials when exposed to RE beam, potentially critical, requires comprehensive study.

The primary aim of this thesis is to investigate the termination dynamics of the RE current in a post-disruption fusion plasma. The research begins by studying the influence of the RE current on the evolution of MR (or tearing modes) in a 2D slab configuration characterized by a single magnetic island. In the initial phase, the nonlinear two-fluid reduced MHD code SCOPE3D was validated based on existing results. This allowed to focus on nonlinear studies about the island rotation and the presence of microscales in asymmetric configuration (mismatch between the radial current profile peak and island resonant surface position). This study identified the presence of microlayers in the RE current profile, which influenced the system transition from the linear to the nonlinear phase. The island rotation was found to become zero once the saturation was reached. The research further demonstrates that

electron inertia effects lead to the formation of microscales on the thermal electron current profile, which might impact plasma stability.

In the second phase of the research, the impact of plasma background resistivity on the benign termination of RE observed in the JET experiment #95135 after an SPI injection was investigated. The nonlinear MHD code JOREK was used in this study with RE transport modelled through advection at the speed of light. The RE termination is driven by magnetic stochasticity resulting from the interaction of a double tearing mode with secondary modes. In our study, higher resistivity values enhanced chaotic plasma dynamics, with the double tearing mode emerging as the dominant contributor to RE loss. In contrast, lower resistivity values allowed secondary modes to play a critical role in the evolution of magnetic stochasticity. This analysis indicated that, despite losing similar RE current amplitudes in various cases, the intense magnetic stochasticity observed with high resistivities resulted in a larger wetted area on the wall, contributing to a more benign termination of RE.

Finally, the thesis addresses the impact of the RE beam on the Tokamak First Wall. A detailed examination was conducted to assess the damage inflicted by a highly energetic RE beam on Beryllium (Be) and Tungsten (W) materials, employing FLUKA and FreeFEM++ simulation tools. FLUKA was utilized to calculate energy deposition profiles, beginning from a customized energy distribution function for RE, representing a novel approach in this work. The apparent heat capacity method was implemented in FreeFEM++ in collaboration with a PhD colleague to simulate the thermal response of the material following RE energy deposition. The findings revealed that W higher stopping power results in greater energy deposition near its surface due to elastic scattering and delta-ray production, making it a more effective material for limiting damage. Conversely, in Be, photon energy deposition becomes dominant near the opposite border, while in W, photons become the primary energy carriers after just a few millimetres of penetration. The thermal response analysis demonstrated that W effectively limits melting to the near-surface region, necessitating a higher RE current for melting initiation compared to Be.

Contents

List of Figures **xi**

List of Tables **xxii**

1 Introduction **1**

1.1 Aim of the thesis 3

1.2 Structure of the work 4

2 Runaway Electrons in Tokamaks **6**

2.1 Runaway electron generation 8

2.1.1 Primary generation mechanisms 9

2.1.2 Secondary generation mechanisms 12

2.2 Runaway electron losses 14

2.2.1 Partially ionized impurities effects 15

2.2.2 Radiation losses 16

2.2.3 Radial runaway electrons losses 18

2.2.4 Runaway electrons losses to the wall 19

2.3 Runaway electron mitigation 21

2.3.1 Massive gas injection 21

2.3.2 Shattered pellet injection 24

2.3.3 Resonant Magnetic Perturbation and Runaway Electron Mitigation Coil . . . 26
2.3.4 Sacrificial limiters . . . 29

3 MHD instabilities effects on Runaway electron termination 31

3.1 Reduced MHD equations . . . 34
3.1.1 Resistive RMHD equations . . . 35
3.1.2 Non resistive RMHD equations . . . 36
3.2 Single helicity reconnection event . . . 37
3.3 Multiple helicity reconnection event . . . 39
3.3.1 Magnetic stochasticity . . . 40
3.3.2 Influence of the resistivity on the stochasticity evolution . . . 41
3.4 Mutual interaction between Runaway Electrons and Magnetic reconnection . . . 45
3.4.1 Single helicity . . . 46
3.4.2 Multiple helicity . . . 50
3.5 RE termination dynamics during JET pulse 95135 . . . 57
3.5.1 Plasma stochastization . . . 59
3.5.2 RE regeneration . . . 61

4 Numerical Tools 63

4.1 SCOPE3D . . . 63
4.2 JOREK . . . 66
4.2.1 JOREK spatial discretization . . . 66
4.2.2 JOREK time discretization . . . 67
4.2.3 Simulation steps . . . 68
4.3 FLUKA . . . 69
4.4 FREEFEM++ . . . 72

5 Postdisruption plasma stability in the presence of a runaway electron current 76

5.1 Symmetric case . . . 78

5.1.1 Linear analysis . . . 79

5.1.2 Non Linear analysis . . . 80

5.2 Asymmetric case . . . 82

5.2.1 Linear analysis . . . 83

5.2.2 Non Linear analysis . . . 88

5.3 Comparison between SCOPE3D and JOREK . . . 93

5.4 Conclusions . . . 95

6 Runaway electron benign termination modelling in JET pulse 95135 98

6.1 Simulation setup . . . 99

6.2 Results . . . 99

6.2.1 Comparison between the two higher resistivity cases . . . 106

6.2.2 Comparison between the two lower resistivities cases . . . 109

6.2.3 Heat loads . . . 114

6.3 Conclusions . . . 120

7 Runaway electrons interaction with Plasma facing components 122

7.1 Impact of Runaway electrons beam on First Wall tiles . . . 123

7.1.1 Fixed impact angle . . . 125

7.1.2 Parametric scan in the impact angle . . . 129

7.2 Material thermal response to the RE beam impact . . . 132

7.2.1 Simulation setup . . . 133

7.2.2 Thermal analysis results . . . 135

7.3 Conclusions . . . 137

8 Conclusions **140**

References **145**

List of Figures

2.1 Evolution of the induced electric field, $E_{\|}$ (red curve), and electron temperature, T_e (blue curve), during the TQ (cian region), CQ (red region) and Runaway plateau (yellow region) phases on the left. On the right, the evolution of the plasma current, I_p (continuous curve), runaway current, I_{re} (dashed curve) and thermal current, I_Ω (dotted curve) 8

2.2 a) Normalized RE current density j_{run} radial distribution with (green curve) and without (red curve) hot tail and the initial ohmic current j_{ohm} (dashed black curve). b) Temporal evolution of the plasma current, I_{tot}, with (red plain curve) and without (green plain curve) hot tail. Temporal evolution of the RE current, I_{run}, with (green dashed curve) and without (red dashed curve) hot tail 12

2.3 a) Time evolution of the plasma current I_p in the absence (discharge number 117833, continuous curve) and presence (discharge number 117849, dashed curve) of large magnetic fluctuations. and Time evolution of the temporal variation s in the magnetic field in absence b) and presence c) of magnetic fluctuations 19

2.4 Observed melt damages of tungsten poloidal limiter after 400 disruptions in the tokamak T-10. Melting and craters on the tungsten plates at the torus outer board side 20

2.5 Comparison of the time evolution of electron density, n_e, at the plasma edge a) and core b) for Argon injected via SPI (blue curve) and MGI (red curve). At $t - t_{tq} = 0$ the disruption take place with a TQ followed by a CQ 25

2.6 a) Time evolution of the plasma current with MGI mitigated disruption (blue dashed curve) and SPI mitigated disruption (red continuous curve). b) Time evolution of the line integrated electron density with the same colors as in a) 26

2.7 a) Cross-section of the ITER RMP coils in blue and the unperturbed plasma magnetic equilibrium in green. b) flux-surface averaged magnetic perturbation as a function of radial position for n=3 configuration (black curve) and n=9 configurations (dashed lines). The current driven in the RMP coils is 60 kA 28

2.8 a) RE loss time in logarithmic scale as a function of starting position (ψ, θ) where $\theta = atan^2(Z,R)$ in radiants. b) Time evolution of particles lost percentage on the different flux surfaces $\psi = 0.5$ (blue), $\psi = 0.6$ (magenta), $\psi = 0.7$ (red), $\psi = 0.8$ (green) with particle initial energy of 1 MeV in configuration with n=3 called 'B' 28

2.9 (a) Poloidal location of the 4 different limiters on a DEMO sector. b) Top view of the plasma chamber showing the limiters in the 8 DEMO sectors 30

3.1 Representation of the magnetic island formation starting from a toroidal plasma a), cut open b) and laid out flat c), with transformation to $B*$ d) and a radial magnetic field perturbation B_r to show the formation of magnetic islands e) 33

3.2 Poincaré plots showing the evolution of magnetic stochasticity starting from (a) magnetic islands localized at different resonant surfaces and leading to (b) magnetic stochasticity with normalized flux on the y-axis and normalized toroidal angle on the x-axis 41

3.3 Initial q profile as a function of the radial coordinate (square root of the normalized poloidal flux ψ_N). From top to bottom, the horizontal lines correspond to q=4, 11/3, and 7/2 42

3.4 Evolution of I_p for different values of the resistivity. 43

3.5 Evolution of the magnetic energy in the toroidal harmonics $n = 1-5$ for $\eta = 1 \times 10^{-5}$ (dotted curves), $\eta = 1 \times 10^{-6}$ (plain curves), and $\eta = 3 \times 10^{-7}$ (dashed curves) 44

3.6 Comparison between the analytically and numerically derived linear growth rates of the tearing instabilities with (plain curve and stars) and without (dashed curve and squares) 48

3.7 a) The simulation computational domain is colored with the normalized RE density distribution and flux surfaces. b) Initial RE current (purple curve) and safety factor profiles (dashed green curve) as a function of the normalized poloidal flux ψ_N 52

3.8 Magnetic energy growth of the toroidal harmonics as a function of time 53

3.9 Poincaré plots showing the evolution of the magnetic field stochastization at different time points; starting from $t = 0.97ms$ corresponding to $t = 0\mu s$ in panel a), b) $t = 31\ \mu s$, c) $t = 81\ \mu s$, d) $t = 91\ \mu s$, e) $t = 122\ \mu s$, $t = 194\ \mu s$. The background plasma color indicates the RE density, whereas the RE current amplitude in the top right corner of each panel is noted at different times. 54

3.10 a) RE loss time in logarithmic scale as a function of starting position (ψ, θ) where $\theta = atan^2(Z,R)$ in radiants. b) Evolution of the RE density as a function of the normalized flux and time computed through ANTS code. c) Evolution of the RE density as a function of the normalized flux and time computed through the Rechester–Rosenbluth diffusion model. d) Evolution of the RE density as a function of the normalized flux and time computed through exponential loss model 56

3.11 a) Current density profiles and b) Safety factor profiles at different time points with $t = 0\ \mu s$ corresponding to $t = 0.97\ ms$ 56

3.12 a) RE flux (particles per square meter per unit time) distribution as a function of ψ_N and distance from the limiter point b) RE fluence $(1/m^2)$ distribution as a function of ψ_N and toroidal angle ϕ (shown as φ in the figure) during the time interval shown in panel a) 57

3.13 Comparison between three RE termination scenarios with no second injection (blue curves), high Z impurity second injection (red curves), and low Z impurity second injection (green curves). Evolution of the a) total current, b) average electron density, c) total neutron rate, and d) total radiated power from the thermal quench. e) Wall heat flux as a function of impacting RE current. The dashed vertical line indicates the D_2 SPI injection 59

3.14 Comparison between the (a) measured infrared synchrotron radiation image and (b) SOFT reconstructed synchrotron image 60

3.15 Evolution of the minor radial location of $m = 4$, $m = 5$ and $m = 6$ magnetic island chains derived from the IR synchrotron images starting from $t_{ref} = 48.0233\ s$ taken as reference 61

3.16 Evolution of the total current and radiated power 62

4.1 Left panel: Toroidal coordinate system used in JOREK. Right panel: A 2D Bezier element in R-Z space 66

4.2 Be (green) and W (red) radiation yield as a function of electron energy in MeV. 71

4.3 Be (green) and W(red) CSDA range in cm as a function of energy. . 72

4.4 Representation of the problem computational domain and the adopted boundary conditions. The slab width dimension has been cut to improve readability 74

4.5 Comparison between the position of the melting front x_M (left panel) and front and back face temperature (right panel) obtained with the AHC method developed in FreeFEM++ and the reference results. . . 75

5.1 Numerical and analytically derived linear growth rates, γ, for a pure resistive reconnecting mode driven by a runaway current (blue points and blue curve) compared with the case without runaway current (green points and green curve) along with the numerical γ with (red points) and without a RE current (magenta points) compared with the results of Eq. 5.5 in the presence of ρ_s (red curve) 80

5.2 Numerical and analytically derived saturation island widths, w, for the pure resistive reconnecting mode driven by a RE current (green dots and green curve) compared with the case without RE (red dots and red curve). The plus markers refer to the ρ_s cases 81

5.3 Total current density distribution at saturation for the case $\Delta' = 0.5$. Left panel: contour plot of the current density with superimposed magnetic surfaces. Right panel: radial profiles for island X-point (red curve) and O-point (blue curve) compared with the equilibrium profile (green curve). The dashed line defines the width of the magnetic island at saturation. 82

5.4 Analytical growth rate, $Re(\gamma)$ (blue line) and rotation frequency, $Im(\gamma)$ (rust curve) given by Eq. 3.38 compared with the numerical growth rate (blue points) and rotation frequency (rust points) for η in the $(1 \times 10^{-3}, 1 \times 10^{-6})$ interval, $\Delta' = 1.015$ and $c/v_A = 1$, $d_e = 0$, $\rho_s = 0$. 84

5.5 Analytical growth rate, $Re(\gamma)$ (blue line) and rotation frequency, $Im(\gamma)$ (rust curve) given by Eq. 3.38 compared with the numerical growth rate (blue points) and rotation frequency (rust points) for η in the $(1 \times 10^{-4}, 5\times^{-7})$ interval, $\Delta' = 6.057$ and $c/v_A = 1$, $d_e = 0$, $\rho_s = 0$. 85

5.6 Modulus of the eigenfunction of mode 1 for total current (blue curve), runaway current (red curve) and thermal electrons current (green curve) profiles showing the inner layer δ_2 on the runaway current profile and the resistive layer δ_1 on the thermal electrons profile for $\eta = 1 \times 10^{-4}$, $\Delta' = 6.057$ and $c/v_A = 1$, $d_e = 0$, $\rho_s = 0$ in the left panel and $\eta = 1e-4$, $\Delta' = 6.057$ and $c/v_A = 10$, $d_e = 0$, $\rho_s = 0$ in the right panel. 86

5.7 Numerically obtained inner layer widths, δ_2 in a purely resistive case compared with the analytical derivation given in Eq. 3.37 in the left panel and numerically obtained resistive layer widths, δ_1 compared with the analytical derivation given in Eq. 3.20 in the right panel for different values of γ corresponding to η in the $(1\times10^{-4}, 5\times10^{-7})$ interval, $c/v_A = 1, 10$ and $\Delta' = 6.057$. The green dashed line corresponds to the analytical curve for $c/v_A = 1$ and the magenta dashed line to the analytical curve for $c/v_A = 10$, while the blue curve represents the numerical results for $c/v_A = 1$ and the red curve for $c/v_A = 10$. The magenta curve in the right panel is absent since δ_1 is independent of c/v_A ratio 87

5.8 Left panel: radial profile of the modulus of the $m = 1$ mode eigenfunction for total current (blue curve), runaway current (red curve) and thermal electrons current (green curve) for $\eta = 1e-4$, $\Delta' = 6.057$ and $c/v_A = 10$. $d_e = 0.05$, $\rho_s = 0$. Right panel: Radial profile of the eigenfunction distortion of thermal electrons current observed for $d_e = 0.05$ (red line) and $d_e = 0.1$ (blue line). The curves have been obtained by the difference $J_{th}(x) - A\exp(-(x-x_s)^2/2\delta_1^2)$ where $A = 3.28e-5$ when $d_e = 0.05$ and $A = 3e-5$ when $d_e = 0.1$. In both cases, $\eta = 1e-4$, $\Delta' = 6.057$ and $c/v_A = 10$. 88

5.9 Temporal evolution of the eigenfunction modulus of mode m=1 associated with the runaway (green) and thermal (blue) current, and the width of the islands (rust) for a purely resistive regime $\eta = 1\times10^{-4}$, $c/v_A = 1$ and $\Delta' = 6.057$. The vertical dashed lines identify the time instants when the transition to the nonlinear stage occurs for runaway ($t_2 = 1400$) and thermal electrons ($t_1 = 1700$). The dashed horizontal lines identify the magnetic island widths corresponding to these times. The sizes of the island at t_1 and t_2 are comparable with δ_1 and δ_2, respectively. 89

5.10 RE radial profile distribution during the linear evolution (red) at t=1500 and during the runaways non-linear evolution at t=1800 for $\eta = 1\times10^{-4}$, $c/v_A = 1$ and $\Delta' = 6.057$, $d_e = 0$, $\rho_s = 0$. 90

5.11 Perturbed RE current distribution with the corresponding magnetic island (blue line) during the nonlinear phase (left) and RE radial profile (right) at t=2500 across the island $O-$point for $\eta = 1 \times 10^{-4}$, $c/v_A = 1$ and $\Delta' = 6.057$, $d_e = 0$, $\rho_s = 0$. 90

5.12 Temporal evolution of the X-point position of the magnetic island in a purely resistive case with $\eta = 1 \times 10^{-4}$, $c/v_A = 1$ and $\Delta' = 6.057$, $d_e = 0$, $\rho_s = 0$. The green line shows the numerical poloidal shift while the blue line corresponds to the theoretical prediction according to the formula (3.38). The rust line represents the displacement along the x direction. 91

5.13 Temporal evolution of ψ'_X w/o (blue curve) and with RE (rust curve) at the left panel and temporal evolution of island area w/o (blue curve) and with RE (rust curve) at the right panel for a purely resistive case with $\eta = 1e-4$, $c/v_A = 1$ and $\Delta' = 6.057$. 92

5.14 Temporal evolution of ψ'_X w/o (blue curve) and with RE (rust curve) at the left panel and temporal evolution of island area w/o (blue curve) and with RE (rust curve) at the right panel for a purely resistive case with $\eta = 1e-4$, $c/v_A = 1$ and $\Delta' = 3$. 92

5.15 Thermal electron current distribution over the magnetic island with $d_e = 0.05$ (left) and thermal electron radial profile across the island O-point at $d_e = 0$ (green), $d_e = 0.05$ (blue) and $d_e = 0.1$ (red) (right) for $\eta = 1e-4$, $c/v_A = 10$ and $\Delta' = 6.057$. 93

5.16 Comparison between the scaling law and the numerical growth rates as a function of the resistivity. The resistivity interval is $(1 \times 10^{-4}, 1 \times 10^{-6})$ 95

5.17 Comparison between the islands without (left panel) and with (right panel) RE with $\eta = 1 \times 10^{-5}$. 95

6.1 Left panel: Current (red) and q (blue) profiles as a function of normalized poloidal flux ψ_N. Right panel: Simulations computational domain coloured by the normalized RE density number. 100

6.2 Comparison between the numerical growth rates $\gamma_{numerical}$ (blue curve) and the FKR scaling law (red dashed curve). 101

6.3 Temporal evolution of the RE current amplitude with $\eta = 6.1 \times 10^{-4}$ Ωm (blue), $\eta = 1.84 \times 10^{-4}$ Ωm (red), $\eta = 3.3 \times 10^{-5}$ Ωm (green) and $\eta = 6.1 \times 10^{-6}$ Ωm (magenta) 101

6.4 Temporal evolution of the $n = 1$ (red), $n = 2$ (yellow), $n = 3$ (cyan), $n = 4$ (blue) and $n = 5$ (magenta) magnetic energy for a) $\eta = 6.1 \times 10^{-4}$ Ωm and b) $\eta = 1.84 \times 10^{-4}$ Ωm. The vertical dashed line underlines the start of the nonlinear phase. 102

6.4 Temporal evolution of the $n = 1$ (red), $n = 2$ (yellow), $n = 3$ (cyan), $n = 4$ (blue) and $n = 5$ (magenta) magnetic energy for c) $\eta = 3.3 \times 10^{-5}$ Ωm and d) $\eta = 6.1 \times 10^{-6}$ Ωm. The vertical dashed line underlines the start of the nonlinear phase. 103

6.5 Temporal evolution of the $n = 1$ E_{mag} (blue curve) and RE current amplitude (red curve) with a) $\eta = 6.1 \times 10^{-4}$ Ωm and b) $\eta = 1.84 \times 10^{-4}$ Ωm. The magenta and green vertical dashed line underlines the RE loss phase start and end. 104

6.5 Temporal evolution of the $n = 1$ E_{mag} (blue curve) and RE current amplitude (red curve) with c) $\eta = 3.3 \times 10^{-5}$ Ωm and d) $\eta = 6.1 \times 10^{-6}$ Ωm. The magenta and green vertical dashed line underlines the RE loss phase start and end. 105

6.6 Poincaré cross sections at different time points for $\eta = 6.1 \times 10^{-4}$ Ωm showing magnetic island formation, magnetic field stochastization and the reformation of the magnetic flux surfaces. The cross sections are coloured by the RE density and the RE current amplitude is also shown at different time points a) t=0 μs, b) 13 μs, c) 19 μs, d) 21 μs, e) 25 μs and f) 45 μs ($t = 0.973$ ms is taken as reference) 106

6.7 Poincaré cross sections at different time points for $\eta = 1.84 \times 10^{-4}$ Ωm showing magnetic island formation, magnetic field stochastization and the reformation of the magnetic flux surfaces. The cross sections are coloured by the RE density and the RE current amplitude is also shown at different time points a) t=0 μs, b) 41 μs, c) 58 μs, d) 68 μs, e) 78 μs and f) 168 μs ($t = 1.1$ ms is taken as reference). 107

6.8 Temporal evolution of the total current (top) and q profile (bottom) as a function of ψ_N for $\eta = 6.1 \times 10^{-4}$ Ωm 108

6.9 Temporal evolution of the total current (top) and q profile (bottom) as a function of ψ_N for $\eta = 6.1 \times 10^{-4}$ Ωm 109

6.10 Temporal evolution of the toroidal harmonics magnetic energy for $\eta = 6.1 \times 10^{-4}$ Ωm (dashed curve) and $\eta = 1.84 \times 10^{-4}$ Ωm (dash-dotted curve). The time is rescaled as explained in the text. 111

6.11 Temporal evolution of the toroidal harmonics magnetic energy for $\eta = 1.84 \times 10^{-4}$ Ωm (dash-dotted curve) and $\eta = 6.1 \times 10^{-6}$ Ωm (plain curve). The time is rescaled as explained in the text. 112

6.12 Poincaré cross sections at different time points for $\eta = 3.3 \times 10^{-5}$ Ωm showing magnetic island formation, magnetic field stochastization and the reformation of the magnetic flux surfaces. The cross sections are coloured by the RE density and the RE current amplitude is also shown at different time points a) t=175 μs, b) 277 μs, c) 380 μs, d) 441 μs, e) 564 μs and f) 831 μs ($t = 1.6\,ms$ is taken as reference). 113

6.13 Temporal evolution of the safety factor profile as a function of ψ_N for $\eta = 3.3 \times 10^{-5}$ Ωm 113

6.14 Poincaré cross sections at different time points for $\eta = 6.1 \times 10^{-6}$ Ωm showing magnetic island formation, magnetic field stochastization and the reformation of the magnetic flux surfaces. The cross sections are coloured by the RE density and the RE current amplitude is also shown at different time points a) t=185 μs, b) 410 μs, c) 626 μs, d) 728 μs, e) 827 μs and f) 1027 μs ($t = 2.94\,ms$ is taken as reference). 114

6.15 Temporal evolution of the magnetic field lines connection length as a function of ψ_N for $\eta = 6.1 \times 10^{-4}$ Ωm 115

6.16 Temporal evolution of the magnetic field lines connection length as a function of ψ_N for $\eta = 1.84 \times 10^{-4}$ Ωm 116

6.17 Temporal evolution of the magnetic field lines connection length as a function of ψ_N for $\eta = 3.3 \times 10^{-5}$ Ωm 116

6.18 Temporal evolution of the magnetic field lines connection length as a function of ψ_N for $\eta = 6.1 \times 10^{-6}$ Ωm 117

6.19 Heat loads as a function of wall area for a) $\eta = 6.1 \times 10^{-4}$ Ωm, b) $\eta = 1.84 \times 10^{-4}$ Ωm, c) $\eta = 3.3 \times 10^{-5}$ Ωm and d) $\eta = 6.1 \times 10^{-6}$ Ωm. 119

7.1 RE energy distribution at t= 0.931s (blue), t=0.952s (cyan) and t=0.962s (red) 124

7.2 2D representation of the tile geometry with the impact angle of the RE beam 124

7.3 1D projection of the ED along the Z direction for Be (green) and W (red) with a point beam impacting at (X,Y,Z)=(5,5,0) cm with 5 degrees impact angle with respect to the tile surface. 126

7.4 2D projection of the ED on the XZ plane for Be at the left panel and W at the right panel with a point beam impacting at (X,Y,Z)=(5,5,0) cm with 5 degrees impact angle with respect to the X direction. . . . 126

7.5 2D projection of the electron fluence in the XZ plane for Be at left and W at right with an impact angle of 5° for both materials. 127

7.6 1D projection of the ED in Be at the left panel and W at the right panel with default (blue) and high (red) photon threshold. 128

7.7 2D projection of the ED on the XZ plane for Be at the left panel and W at the right panel with a $10cm^2$ beam impacting at (X,Y,Z)=(5,5,0) cm with 5 degrees impact angle with respect to the X direction. . . . 129

7.8 1D projection of the ED in Be over the full thickness at the left panel and near the surface at the right panel for RE beam impact angles of 1 degree (blue curve), 5 degrees (red), 15 degrees (brown), 45 degrees (green) and 90 degrees (magenta) 130

7.9 1D projection of the ED in W over the full thickness at the left panel and near the surface at the right panel for RE beam impact angles of 1 degree (blue curve), 5 degrees (red), 15 degrees (brown), 45 degrees (green) and 90 degrees (magenta). 130

7.10 2D projection of the ED on the XZ plane for Be with 5° at the left panel and with 15° at the right panel. 131

7.11 2D projection of the electron fluence in the XZ plane for Be with 15° impact angle. 132

7.12 Characteristic times of the heat diffusion for Be (left panel) and W (right panel) at different temperatures up to the melting 133

7.13 Schematic representation of the tile with the RE beam (arrow) impacting at the centre with 10 cm^2 square area highlighted by the blue square. The results are shown on a cutting section (blue rectangle) parallel to the beam. 134

7.14 Temporal evolution of the maximum solid temperature for W (left panel) and Be (right panel) at 100 kA (blue curve), 200 kA (red curve), 300 kA (green curve), 400 kA (black curve) and 500 kA (magenta curve) RE current 136

7.15 Melted thickness as a function of the beam RE current for Be (red curve) and W (blue curve) tile materials 136

7.16 Temperature map of the entire solid region at the end of the energy deposition for a beam current of 500 kA for Tungsten (left panel) and Be (right panel). 137

7.17 Temperature profile within the solid domain for both Tungsten (blue curve) and Beryllium(red curve) in case of a 500 kA beam current. Only the first 10 mm of the total thickness are shown here, where relevant gradients can be observed 138

List of Tables

3.1 Simulation input parameters 52

6.1 Simulations input parameters 100

6.2 RE energy deposition area as a function of the resistivity 119

7.1 Energy deposited in C and W per primary electron at different beam incident angles 131

7.2 Melting temperature, latent heat of fusion and density of the considered materials adopted in the simulation. 134

7.3 Energy per unit volume to melt Tungsten and Beryllium (third column) given by the sum of the first two middle columns. 135

Chapter 1

Introduction

Nuclear energy is a crucial solution for achieving decarbonization goals due to its ability to produce large amounts of electricity with near-zero greenhouse gas emissions. As global energy demands continue to rise, nuclear energy provides a stable and reliable alternative to fossil fuels, complementing intermittent renewable sources like wind and solar.

Nuclear fusion is a promising mechanism for generating power. It is potentially better than fission, because it produces less radioactive waste, has lower nuclear waste output, and cannot undergo an uncontrolled reaction chain. Extensive research has been underway for many years to develop this power source. The next generation of Tokamak devices, such as the International Thermonuclear Experimental Reactor (ITER) and later the DEMOnstration Power Plant (DEMO), are expected to be the first to generate more power than is needed to sustain the nuclear reactions.

Private fusion companies such as Commonwealth Fusion Systems, Helion Energy, and Tokamak Energy are making rapid advancements, attracting billions in private investment and working toward reactor designs that could be commercially viable within the next twenty years. With significant government initiatives like ITER and DEMO, alongside private investors committing tens of billions to fusion research and development, the progress in fusion energy highlights a global commitment to a carbon-free energy future. However, several unresolved issues may pose significant challenges to maintaining this momentum.

This thesis focuses on runaway electrons (RE), which represent one of the main threads to the commercial deployment of fusion reactors. RE are generated during

a plasma disruption, which is a rapid, uncontrolled event where the stability of the plasma breaks down, leading to a sudden loss of confinement. This uncontrolled event can result in a few gigajoules of energy being deposited onto the walls of large machines, like ITER and DEMO, in a short time interval [1].

A disruption is either caused by Magnetohydrodynamic (MHD) instabilities, such as magnetic reconnection (MR) leading to topological changes in the magnetic field, or the presence of impurities, which leads to a sudden loss of plasma thermal energy. This increases the plasma resistivity, leading the plasma current and poloidal magnetic field to quench. During this quench, an intense electric field is generated.

This electric field accelerates a portion of the plasma electrons to the so-called runaway regime, where these electrons, called runaway electrons, travel at the speed of light. These electrons can carry up to 50% of the pre-disruptive plasma current and cause severe damage to the Plasma Facing Components (PFC).

The fusion community is actively exploring various solutions to prevent and mitigate RE. The issues related to RE are addressed multiple times in the EUROfusion roadmap for achieving fusion energy [2]. Specifically, ITER is tasked with demonstrating the optimal plasma conditions that minimize disruptions, therefore RE, and validating strategies for mitigating them.

Multiple systems are being studied to either suppress the RE generation or mitigate their effects on PFC. However, the use of mitigation strategies can lead the RE to trigger the evolution of magnetic reconnection events, which in turn strongly influence the RE current itself. On the other hand, the presence of multiple MR events can lead to the stochastization of the magnetic field, which can benefit the RE termination.

Another critical aspect of RE dynamics is the interaction between the RE beam and the reactor first wall (FW) materials. The RE impact on the FW can lead to significant material degradation, erosion, and even melting, depending on the intensity and duration of exposure. Therefore, understanding the behaviour of first-wall materials under these extreme conditions is essential for the design of future fusion reactors.

1.1 Aim of the thesis

The mutual influence between MR and RE is crucial for designing mitigation strategies to ensure the safe termination of RE. Therefore, this thesis aimed to investigate the termination dynamics of the RE current in a post-disruption plasma.

Previous studies carried out by Helander et al. in Ref. [3] and Liu et al. in Ref. [4] have analytically and numerically explored this topic using a fluid description of RE current with a single magnetic island. Ref. [3] calculated the linear growth rate and saturation amplitude of a magnetic island in the presence of a symmetric RE current profile peaking at the rational surface. However, the work in Ref. [3] had limitations, such as periodic boundary conditions and analytical formulations verified only for small values of the instability parameter Δ'.

Ref. [4] expanded this model to cylindrical geometry, introducing an asymmetric current profile (mismatch between the radial position of the rational surface and current peak). This revealed the formation of a new sublayer on the RE current profile and island rotation in the linear phase of the island evolution. However, the nonlinear regime has not been analyzed.

This PhD research used the SCOPE3D code, incorporating non-periodic boundary conditions and a two-fluid model to verify and extend the literature results. In particular, this allowed the study of magnetic island growth up to saturation without the interference of periodic boundary conditions. Moreover, the linear theory from Ref. [4] was verified in 2D slab geometry and extended to the nonlinear regime, where new behaviours of this complex interaction were uncovered.

The next step involved studying the mutual influence between multiple MR and a RE current. To do this, the modelling of the RE termination observed in the JET experiment #95135 was considered.

In particular, this modelling was first carried out by Bandaru et al. in Ref. [5] using the nonlinear MHD code JOREK. This study demonstrated the role of magnetic stochasticity in causing RE loss, where stochasticity originated from interactions between multiple magnetic islands. The transport of RE has been modelled through an ad-hoc diffusion mechanism due to the high computational demands of fully advective simulations. Recent advancements in the JOREK RE module have enabled advection for more accurate simulations.

In this thesis, the RE advection at the speed of light was used to model the RE loss observed during the experiment. Different resistivity values were also considered to account for plasma recombination effects following massive deuterium injection, replacing the fixed resistivity assumption of 10 eV used in [5]. This allowed to study the role of the primary and secondary instabilities in generating magnetic stochasticity at various resistivities. Moreover, the influence of the plasma resistivity on the RE footprint on the wall was studied.

The last point addressed in this work was the impact of the RE beam on the Tokamak FW. Several studies have numerically assessed RE-induced damage by generating energy deposition (ED) profiles using Monte Carlo codes like FLUKA and ENDEP to simulate the interaction between the RE beam and materials. These profiles are then used to model temperature evolution and material erosion with tools like ANSYS and MEMOS-U. In our work, we established a workflow using FLUKA and FREEFEM++ to evaluate the damage caused by realistic RE energy distribution functions, improving upon earlier studies that focused on monoenergetic or simplified distributions.

The influence of the different electron transport mechanisms on the energy deposited by RE was also studied. Moreover, different impact angles and areas were considered to assess the material response to different input conditions. Finally, the material thermal response was analyzed in terms of the melting front progression and temperature dynamics as a function of RE current amplitude. This part was done with a PhD colleague from Politecnico di Torino, who implemented the apparent heat capacity method in FREEFEM++ to study the melting problem.

1.2 Structure of the work

This thesis is organized as follows:

1. in Chapter 2 an introduction about the various mechanisms for RE generation, losses and mitigation is given.
2. in Chapter 3 a literature review of the mutual influence between MR and RE is presented. First, an introduction to single and multiple magnetic islands MR physics is given. Afterwards, the interaction of these MR events with the RE current is described.

3. in Chapter 4 the numerical tools used for the analysis are presented.

4. in Chapter 5 results of the work about the postdisruption plasma stability in the presence of a RE current are shown. This chapter is based on the work published in [6] and [7].

5. in Chapter 6 results of the work about the RE benign termination modelling in JET experiment #95135 are described.

6. in Chapter 7 results on the investigation of the damage caused by a RE beam onto the Tokamak First Wall tiles are reported. This chapter is based on the work submitted for publication in [8].

Chapter 2

Runaway Electrons in Tokamaks

Runaway electrons (RE) are high-energy particles that can accelerate to near-light speeds, posing significant challenges to the stability and safety of future fusion reactors like ITER and DEMO. Although RE can be generated during the start-up or flat-top operation phases in Tokamaks [9], the primary concerns are related to the RE generated during a disruption event. Indeed, RE generated during disruption can potentially cause severe damage to the plasma-facing components (PFC), making their control and mitigation a critical area of research in nuclear fusion technology.

A disruption is a rapid and sudden loss of plasma magnetic confinement, which causes the PFC to undergo extreme thermal and electromagnetic loads. Such an event is initiated by two significant phenomena in Tokamaks, such as the presence of impurities and a global MHD instability, and causes a rapid loss of plasma thermal energy. Indeed, in the presence of impurities, substantial radiative losses occur, whereas an MHD instability causes the stochastization of the magnetic field lines, leading to enhanced heat transport [10]. The consequences of a disruption in terms of the plasma parameters (electric field, temperature, and plasma current) evolution are shown in Fig. 2.1 [11].

The initial phase of disruption is called thermal quench (TQ) and takes place on a sub-millisecond time scale, underlined by the cian color in Fig. 2.1. The temperature (T_e) drop, shown by the blue curve in the left panel, translates into an increase in the plasma resistivity, which would, in principle, affect the plasma current. However, the toroidal current is characterized by longer inductive time scales and cannot undergo significant changes on such a short time scale. The inductive time is the characteristic

time it takes for current to adjust to changing electromagnetic fields and is defined as $\tau = L/\eta$ with L the inductance of the plasma. Therefore, to preserve such a current, the inductive electric field, $E_{\|}$, has to rise as shown by the red curve ($E_{\|}$ in the left panel). This results in a fraction of the thermal electrons reaching the "runaway" regime, as can be observed in the right panel of the exact figure showing the runaway current, I_{re}, with a dashed curve, the plasma current, I_p, with continuous curve and the thermal current,I_Ω, with dotted curve [10].

After the thermal quench, the second phase of a disruption, known as the current quench (CQ) (red region in Fig. 2.1), occurs. This event is characterized by an inductive time scale of the order of milliseconds. It is triggered by increased plasma resistivity, causing a rapid decay of the plasma current, as shown by the continuous curve in the right panel.

In most cases, the change in the plasma current disrupts the plasma vertical stability, giving rise to a Vertical Displacement Event (VDE), causing the PFC to undergo significant mechanical loads[12]. Moreover, a rapidly decaying plasma current induces a loop voltage, $V_{loop} = -LdI/dt$, leading to more electrons entering the runaway regime [13]. This causes an increase in the RE population, allowing the RE avalanche phenomena to take place where the RE increases exponentially, as can be observed in the right panel by the dashed curve. This happens due to RE knock-on collisions with thermal electrons and leads to the RE plateau phase [14], yellow region in Fig. 2.1. During this phase, the RE current intensity remains almost constant for a certain period, and RE can carry all the remaining plasma current. A brief description of the RE generation mechanisms leading to such a current is given in section 2.1.

If such a current arrives at the wall unmitigated, it can cause severe damage to the PFC. However, some mechanisms cause the RE to lose their energy, such as the radiation emitted by the RE spiral motion around the magnetic field lines, called synchrotron radiation, causing the RE population to lose a small fraction of its energy [11]. In addition, RE radial diffusion due to plasma MHD activity causes a RE current to lose energy. These RE loss mechanisms are briefly introduced in section 2.2.

In some cases, the plasma MHD activity, described in chapter 3, can lead to a RE termination, which does not cause any damage to the PFC, the so-called RE benign termination. For this reason, some mitigation strategies focus on influencing plasma

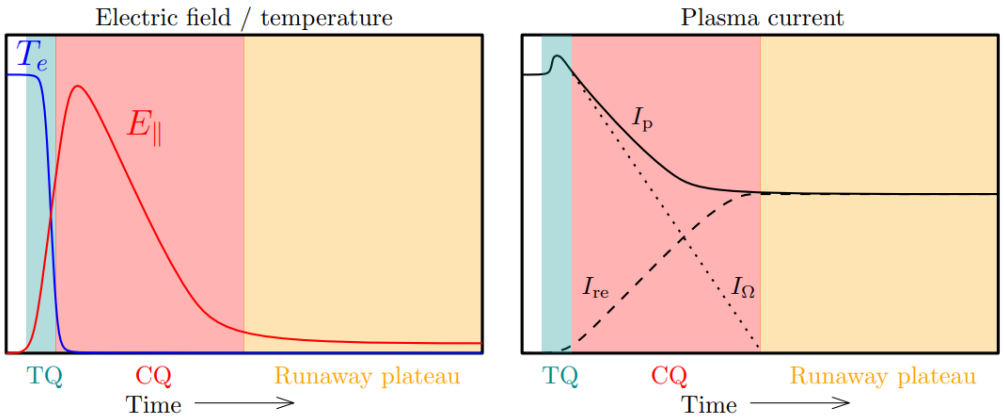


Fig. 2.1 Evolution of the induced electric field, $E_\parallel$ (red curve), and electron temperature, T_e (blue curve), during the TQ (cian region), CQ (red region) and Runaway plateau (yellow region) phases on the left. On the right the evolution of the plasma current, I_p (continuous curve), runaway current, I_{re} (dashed curve) and thermal current, I_Ω (dotted curve). Reproduced from [11].

MHD activity to enhance RE losses. These strategies are included in the so-called Disruption Mitigation System (DMS), which is under design for future Tokamaks like ITER and DEMO. Here, the ones relevant to RE mitigation are described in section 2.3.

2.1 Runaway electron generation

An electron subjected to a constant electric field experiences a force that accelerates it. At the same time, in a plasma, electrons frequently collide with other particles, which creates a resistance to electrons acceleration known as drag force. Due to $m_e/m_i \ll 1$, the contribution from electron-ion collisions can be neglected. Therefore, the electron-electron collision entirely determines the friction on electrons [15]. This force opposes the electron acceleration and tends to slow it down. Suppose the force exerted by the electric field, $F_E = -eE$, where e is the electron charge and E is the electric field, is stronger than the opposing drag force from collisions, $F_D = m_e v_e f_{ee}$, with m_e electron mass, v_e electron velocity, and f_{ee} electron-electron collision frequency. In that case, the electron will continue accelerating, and its energy will keep increasing. As the electrons gain energy and their velocities increase, the collision frequency f_{ee} decreases since $f_{ee} \propto v^{-3}$. When F_E becomes sufficiently strong compared to F_D, the electrons can escape the region of velocity space where

collisions are significant and enter the runaway regime, where the electric force predominantly accelerates them [16].

The processes causing electrons to become runaway are known as primary generation mechanisms and include Dreicer generation, hot tail generation, tritium decay, and Compton scattering of γ rays from the activated wall. Due to the absence of $D-T$ nuclear reactions in current fusion devices, Dreicer, and hot tail generation are the main contributors to runaway electron production, described in subsection 2.1.1. Details about all the mechanisms can be found in [17].

Once a RE seed is generated, the avalanche phenomenon occurs, leading to the formation of a highly energetic Multi-Mega Ampere (MA) RE beam capable of damaging the PFC. This secondary generation mechanism is described in subsection 2.1.2.

2.1.1 Primary generation mechanisms

The Dreicer mechanism for RE generation, as described in Ref. [18], results from the dynamic balance between collisional energy diffusion and electric-field acceleration in a plasma. In this process, the electric field accelerates electrons, while collisions tend to randomize their velocities, typically maintaining a thermal equilibrium. When the applied electric field exceeds a certain threshold, electrons present in the tail of the velocity distribution gain energy faster than collisions can thermalize them, allowing these electrons to enter the runaway regime where they are continuously accelerated to high velocities. In a steady-state plasma, where background conditions such as density, temperature, and electric field remain constant, this mechanism ensures a continuous flow of electrons into a runaway regime and is known as the Dreicer generation [19].

The value of the electric field, known as the Dreicer field E_D, necessary for the thermal electrons, characterized by a thermal velocity $v_{th} = \sqrt{kT/m_e}$ where k is the Boltzmann constant, to become runaways can be obtained by the balance between the electric force and the collisional drag force, $-eE = m_e v_{th} f_{ee}$ [20]. Considering the collision frequency $f_{ee}(v_{th}) = \frac{4\pi e^4 n_e \ln\Lambda}{m_e^2 v_{th}^3}$, where n_e is the electron density, $ln\Lambda$ is the Coulomb logarithm accounting for the effectiveness of small angle collisions over the large angle collisions, and solving the balance for E one can obtain the expression for the Dreicer field,

$$E_D = \frac{4\pi e^3 n_e \ln\Lambda}{m_e v_{th}^2} \tag{2.1}$$

If the induced electric field in the plasma equals E_D, then the accelerating electric force exceeds the maximum friction force that an electron can experience. As a consequence, the thermal electrons in the plasma become runaway. However, in a plasma the electric field is much lower than the Dreicer field ($E \ll E_D$) and, in this case, the analytical formulation of the runaway electron generation rate due to the Dreicer mechanism is given by Ref. [20] and is reformulated in Ref. [19] as

$$\gamma = \frac{dn_{re}}{dt} = C n_e f_{ee} \left(\frac{E}{E_D}\right)^{\frac{-3}{16}(1+Z_{eff})h} \exp\left[-\lambda\frac{E_D}{E} - \sqrt{\eta\frac{(1+Z_{eff})E_D}{E}}\right], \tag{2.2}$$

$$\lambda = 8\frac{E^2}{E_c^2}\left[1 - \frac{1}{2}\frac{E_c}{E} - \sqrt{1-\frac{E_c}{E}}\right],$$

$$\eta = \frac{1}{4}\frac{E^2}{E_c(E-E_c)}\left[\frac{\pi}{2} - \arcsin\left(1-\frac{2E_c}{E}\right)\right]^2,$$

$$h = \frac{1}{3}\frac{1}{\frac{E}{E_c}-1}\left[\frac{E}{E_c} + 2\left(\frac{E}{E_c}-2\right)\sqrt{\frac{E}{E-E_c}} - \frac{Z_{eff}-7}{Z_{eff}+1}\right].$$

where E_D is the Dreicer field defined in (2.1), $E_c = E_D T/(m_e c^2)$ is the critical electric field, $Z_{eff} = \sum_i n_i Z_i^2/n_e$ is the effective plasma charge. The parameters C is of order-unity and λ, η, and h are needed for the relativistic generalization of the runaway generation rate and were introduced in [20] to account for the electrons travelling at the speed of light. If the induced electric field is $E \approx E_c$, then the first seed of RE will be generated through electrons traveling at the speed of light. Therefore, E_c is the minimum electric field necessary for the RE generation. However, some mechanisms could increase the threshold electric field necessary for RE production.

The minimum electric field necessary for runaway generation is higher than E_c due to the pitch angle scatterings, energy losses caused by synchrotron and Bremsstrahlung radiation, and partial screening due to partially ionized impurities

[21], and these are described in section 2.2. The pitch angle (θ) of a charged particle in a magnetic field refers to the angle between the particle velocity vector and the direction of the magnetic field lines. Since the efficiency of electric field acceleration depends on the pitch angle, electrons at smaller pitch angles are more effectively accelerated. Indeed, the electric force acting on the electrons is $-eE\cos\theta$ [15]. Therefore, the effective critical field needed for RE generation is $E_{c,eff} \gg E_c$.

During a disruption, the assumptions of the Dreicer mechanism, which relies on a quasi-steady-state electron velocity distribution, may not apply due to a rapid thermal quench. In particular, during a thermal quench, the plasma cools down faster than the time needed for the high-speed electrons to decelerate through collision due to $f_{ee} \propto v^{-3}$. Therefore, these high-velocity electrons collide less frequently and take longer to slow down than low-velocity electrons. This discrepancy creates a hot tail of high-energy electrons in the otherwise cool post-thermal quench electron distribution. As the disruption progresses, the increasing electric field lowers the runaway threshold velocity, making it easier for these hot tail electrons to accelerate further into the runaway regime. Consequently, a significant portion of the hot tail electrons are converted into RE. This process is known as hot tail runaway generation or burst generation and is crucial in understanding RE dynamics during rapid thermal quenches in Tokamaks [16]. It is shown in Ref. [16] that for JET thermal quench durations of $t_0 < 3ms$, the hot tail generation mechanism dominates over the Dreicer mechanism.

The analytical derivation of the RE density generated due to the hot tail mechanism is derived in Ref. [16] and reported in Ref. [17] as,

$$n_{re,hot-tail} \approx n_{e0}\frac{2}{\sqrt{\pi}}u_{c,min}e^{-u_{c,min}^2} \tag{2.3}$$

$$u_{c,min}^3 = t_0 f_{ee}\left[2ln\frac{E_{D0}}{E_{\|0}} - \frac{4}{3}ln\left(\frac{4}{3}t_0 f_{ee}\right) - \frac{5}{3}\right]$$

where n_{e0} is the initial background density, f_{ee} is the predisruption thermal electron collision frequency, E_{D0} is the initial Dreicer field and $E_{\|0}$ is the initial parallel electric field.

Hot tail generation during tokamak disruptions has implications for the MHD stability of the post-thermal quench plasma. Indeed, if only Dreicer and avalanche

generation mechanisms are considered the final RE current, j_{run} (red curve) in Fig. 2.2 presents a significant peak on the axis with respect to the pre-disruption thermal current distribution (black dashed curve). If the hot tail generation is included, this tends to make the final RE current profile (green curve) less peaked on-axis [16]. The current densities are normalized with respect to the pre-disruption thermal current density on-axis. In addition, as can be observed in Fig. 2.2 b), the hot tail generation mechanism leads to a RE current (green dashed curve) higher than the case without considering such mechanism (red dashed curve).

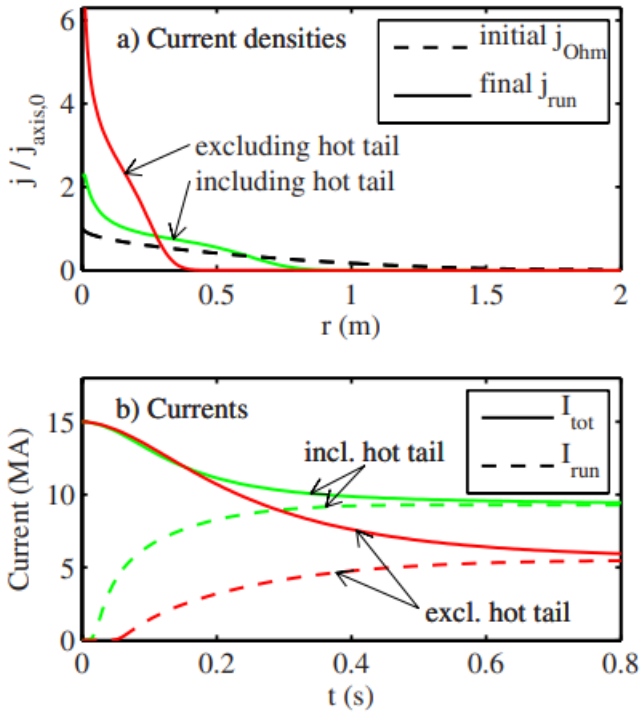


Fig. 2.2 a) Normalized RE current density j_{run} radial distribution with (green curve) and without (red curve) hot tail and the initial ohmic current j_{ohm} (dashed black curve). b) Temporal evolution of the plasma current, I_{tot}, with (red plain curve) and without (green plain curve) hot tail. Temporal evolution of the RE current, I_{run}, with (green dashed curve) and without (red dashed curve) hot tail. Reproduced from [16].

2.1.2 Secondary generation mechanisms

The RE seeds generated through the Dreicer and hot tail mechanisms undergo the avalanche phenomenon, which exponentially increases the RE population, leading to the formation of a RE beam capable of damaging the PFC.

The first formulation of the avalanche-like exponential growth was formulated in [22]. According to Ref. [22], an avalanche-like exponential growth of the runaway electron population can occur whenever these electrons acquire energies between 10-20 MeV from the electric field. This growth happens because high-energy RE can generate additional runaway electrons through collisions, sustaining and amplifying the runaway population.

The avalanche growth reported in [22] is obtained through the solution of an equation representing the generation of secondary RE, $n_{re,A}$, by collision with the RE seed n_{re},

$$\frac{dn_{re,A}}{dW_{re}} = \frac{dn_{re,A}}{dt}\frac{1}{ecE} = \frac{n_{re}}{2m_e c^2 a(Z_{eff})\ln\Lambda} \tag{2.4}$$

where W_{re} is the RE kinetic energy and $a(Z_{eff})$ is a parameter taking account of the plasma effective ionic charge. The solution of the Eq. 2.4 derived assuming no RE losses, neglecting the generation of secondary RE by nonrelativistic RE and indicating with n_{re} the overall generation of RE is,

$$n_{re} = n_{re0}\exp(t/t_0) \tag{2.5}$$

where $t_0 = \frac{2m_e c a(Z_{eff})\ln\Lambda}{eE}$ is the time needed for a relativistic RE to gain the energy of $a(Z_{eff})(10-20\,\mathrm{MeV})$ with $a(Z_{eff})$ a multiplication factor, from the E field. The e-fold increase in the RE density due to avalanche can be obtained through

$$\alpha \approx \frac{I_p}{I_A \ln\Lambda} \tag{2.6}$$

where $I_A = mc^3/e = 0.017MA$ is the Alfvèn current [1]. With a plasma current $I_p = 15MA$, the e-fold growth of the RE density would be around 50. The formulation allows a quick estimation of the avalanche growth rate. However, as shown in [1], the assumptions of non-relativistic limit and absence of pitch angle scattering overestimate the avalanche growth. This is because Eq. 2.5 does not consider the critical electric field, E_c, below which the runaway generation is impossible. For $E \geq E_c$, the avalanche growth rate is derived in [1],

$$\frac{1}{j_{re,A}}\frac{\partial j_{re,A}}{\partial t} = \frac{\frac{1}{\tau \ln\Lambda}\sqrt{\frac{\pi\gamma_L}{3(Z_{eff}+5)}}\left(\frac{E}{E_c}-1\right)}{\sqrt{\left(1-\frac{E}{E_c}+\frac{4\pi(Z_{eff}+1)^2}{3\gamma_L(Z_{eff}+5)(E^2/E_c^2+4/\gamma_L^2-1)}\right)}} \tag{2.7}$$

where $j_{re,A}$ is the RE current generated by avalanche, τ is the collision time, γ_L is the neoclassical function for a Lorentz gas defined in [1] and Z_{eff} is the plasma effective ionic charge.

For the evaluation of the RE energy generated through the avalanche mechanism, Eq. 2.8 is used by [1],

$$\frac{1}{n_{re,A}}\frac{dn_{re,A}}{dEn} \cong exp(-En/T) \tag{2.8}$$

where En is the energy, and

$$T\,(\mathrm{MeV}) \cong 17.0 + 3.4Z_{eff}$$

or

$$T \approx mc^2 \ln\Lambda\sqrt{\frac{3(Z_{eff}+5}{\pi\gamma_L}} \tag{2.9}$$

For plasmas characterized by high Z_{eff}, Eq. 2.8 predicts RE energy in the order of 50 MeV. However, due to the cold post-disruption plasma, impurity ions are only partially ionized. In this case, with most electrons being bound, the Coulomb logarithm can be as low as 10, further limiting the energy of runaway electrons. Consequently, the average energy of RE generated through avalanche will be around 10 to 15 MeV [1].

2.2 Runaway electron losses

As briefly mentioned in the previous section, several mechanisms strongly influence the generation and evolution of a RE current. These mechanisms include the effects

of partially ionized impurities, synchrotron radiation, bremsstrahlung, and RE radial diffusion, which are described in the following subsections.

2.2.1 Partially ionized impurities effects

The effects of the partially ionized impurities presence on the RE generation are derived in a series of papers by Hesslow et al. in [15, 21, 23, 24] and only briefly described here.

Experiments have demonstrated that injecting impurities with high atomic mass into plasmas can significantly enhance the shift of the energy distribution of fast electrons towards lower energies [23]. In a fully ionized plasma, fast electrons interact with the overall charge of the ions, leading to their deflection by elastic collision. On the contrary, in a partially ionized plasma like a cold postdisruption plasma, fast electrons also engage with the internal structure of the ion-bound electrons, leading to energy transfer from the fast electron to the bound electron by inelastic collisions. This means that the bound electrons partially shield or screen the nuclear charge. As a result, the fast electrons can experience a more significant and complex interaction with the nucleus and the ion's inner electrons, leading to greater energy dissipation.

The elastic collision between fast electrons and partially ionized ions leads to an increased pitch-angle scattering in terms of the deflection frequency, $\overline{f}_D$. Ref. [23] shows that the deflection frequency is doubled for electrons with energies around a few hundred keV. The slowing-down frequency, $\overline{f}_S$, between a fast and bound electron is enhanced by one order of magnitude already at energies around tens of keV.

As a result, the screening of impurity nuclei by the bound electrons in partially ionized plasmas leads to a dependence of the avalanche growth rate of RE on the electric field stronger than what is predicted in Ref. [1]. This causes a significantly enhanced growth rate in partially screened conditions at high electric fields caused by bound electrons being transformed in RE by highly energetic RE. At the same time, at lower electric fields, partial screening increases the threshold electric field needed for RE generation, thereby reducing the avalanche growth rate. Additionally, the energy spectrum of the RE, dominated by the avalanche process, decays exponentially and has an average energy that varies with the electric field. This average energy is

notably lower than in the case of complete screening, where the plasma is fully ionized with the same effective charge.

The complete formulation of the avalanche growth rate derived by Hesslow et al. reported in [25] is,

$$\Gamma = \frac{1}{n_{re}}\frac{\partial n_{re}}{\partial t} = \frac{e}{m_e c \ln\Lambda_e}\frac{n_{e,tot}}{n_e}\frac{E_{\parallel} - E_{c,eff}}{\sqrt{4+\overline{f}_s(p_*)\overline{f}_D(p_*)}} \tag{2.10}$$

where $\ln\Lambda_c$ is the relativistic Coulomb logarithm, n_e is the free-electron density, $n_{e,tot} = n_e + \sum_j n_j N_{e,j}$ is the total electron density with n_e being the free electron density, n_j the density of species j and $N_{e,j}$ the number of bound electrons for species j, $\overline{f}_D$ is the generalized deflection frequency as a function of the effective critical momentum p_*, $\overline{f}_s$ is the slowing-down frequency as a function of p_* [21]. The expressions of the quantities in Eq. 2.10 can be found in Ref. [25].

2.2.2 Radiation losses

When an electron beam passes through a plasma, it loses energy due to collisional friction with the plasma ions and electrons. Suppose the plasma is immersed in a magnetic field. In that case, relativistic electrons also lose energy through the emission of synchrotron radiation due to the spiral motion (gyro-motion) around the magnetic field lines. This synchrotron radiation emission creates a reaction force that reduces the energy of the electrons even if the electron beam travels parallel to the magnetic field lines. This is because collisional (pitch angle) scattering causes individual particles to gain momentum perpendicular to the field, initiating gyro-motion and thus emitting synchrotron radiation [26]. In contrast to collisional forces, the radiation reaction force increases with the energy of the electrons. Therefore, it alters the dynamics of the high-energy electrons. In a magnetized plasma subjected to a constant electric field, the emission of synchrotron radiation by the accelerated electrons creates a reaction force that counteracts their acceleration. Apart from increasing the $E_{c,eff}$, the energy losses due to synchrotron radiation can contribute to a saturation effect in the electron runaway mechanism, the RE plateau phase, preventing the RE population from further increasing their energy.

Since RE emits synchrotron radiation in the infrared and visible wavelengths, it is possible to use such radiation as a RE diagnostic tool [27]. Indeed, due to their relativistic speed, RE emits radiation predominantly along their velocity vectors. Therefore, this strong anisotropy in the emitted radiation provides valuable information about the electron energy, radial, and pitch-angle distributions. In addition, with numerical tools capable of simulating radiation emission, known as synthetic diagnostics, it is possible to measure and infer the properties of the RE distribution function, making it an essential method for studying runaway electrons in plasmas [28]. An example of the application of such a tool is given in chapter 3.

Bremsstrahlung radiation is emitted when relativistic electrons interact with ions present in the plasma [29]. Like the synchrotron radiation, also the bremsstrahlung emitted by runaway electrons during RE-ion collisions can be traced through diagnostics. In particular, the high-energy photons emitted in these collisions are traced by the Hard X-ray diagnostics (HXR) and allow to characterize the RE energy distribution [30]. Moreover, HXR emissions occur when a RE beam impacts the First Wall. The intensity of these emissions captured by the HXR diagnostics helps gauge the severity of the impact.

In the presence of partially ionized impurities, radiation emissions due to Brehmstrahlung and synchrotron lead to higher losses of energetic electrons [21]. This is because the screening effects enhance Brehmstrahlung whereas synchrotron radiation increases due to the increase of the pitch angle scatterings with partially ionized atoms. Therefore, the effective critical field $E_{c,eff}$ for RE generation is further shifted to values larger than the critical electric field E_c [31]. Indeed, in the presence of bound electrons, the expression for the critical field becomes [21],

$$E_{c,eff} = \frac{n_{e,tot}}{n_e} E_c \tag{2.11}$$

where $n_{e,tot} = n_e + \sum_j n_j N_{e,j}$ is the total electron density with n_e being the free electron density, n_j the density of species j and $N_{e,j}$ the number of bound electrons for species j.

A higher $E_{c,eff}$ has a beneficial effect on the RE current decay rate as well [31]. In particular, because of the faster avalanche time scale with respect to the inductive time scale, an electric field proportional to the current variation is induced in the plasma. This induced electric field is around the effective critical field in the case

of $I_{re} \gg 60$ kA [31]. As shown in [21], in the case of highly inductive devices like ITER the decay rate is

$$\frac{dI_{re}}{dt} = -\frac{2\pi R E_{c,eff}}{L} \tag{2.12}$$

where L is the inductance. Clearly, with a higher $E_{c,eff}$ the decay rate is increased.

2.2.3 Radial runaway electrons losses

Runaway electrons are highly sensitive to the topology of the magnetic field in a post-disruptive plasma due to their parallel motion with respect to the magnetic field lines [32]. In the presence of magnetic field perturbations, changes in magnetic field topology can occur leading to higher RE losses or higher RE confinement. In the former case, the radial losses of RE reduce the RE avalanche growth rate and increase the RE current decay. However, certain magnetic structures, called magnetic islands, in the latter case can also improve the RE confinement and increase their energy. The physical reasoning of these opposite RE behaviors is described in chapter 3. This subsection is limited to introducing the process affecting the RE losses.

The effect of the magnetic fluctuations on the RE current can be observed in Fig. 2.3 where the plot (a) shows the difference in the plasma current (I_p) evolution in the absence (discharge number 117833, continuous curve) and presence (discharge number 117849, dashed curve) of large magnetic fluctuations during a mitigated disruption in TEXTOR [33]. The plots (b) and (c) show the magnetic field time variation in the respective discharges. In the presence of magnetic perturbations the RE avalanche is significantly affected and the plateau phase is suppressed. This is because a certain fraction of RE can exit the plasma domain before contributing to the avalanche phenomenon.

The minimum level of the magnetic perturbation necessary for the reduction of the RE avalanche exponential factor below a desired maximum tolerable avalanche size N is derived in [34] and is found to be,

$$\frac{\delta B}{B} \geq \frac{a}{2.4}\sqrt{\frac{E-1}{\pi q c R \tau p_{crit}} \ln \frac{1}{N I_A \ln \Lambda}} \tag{2.13}$$

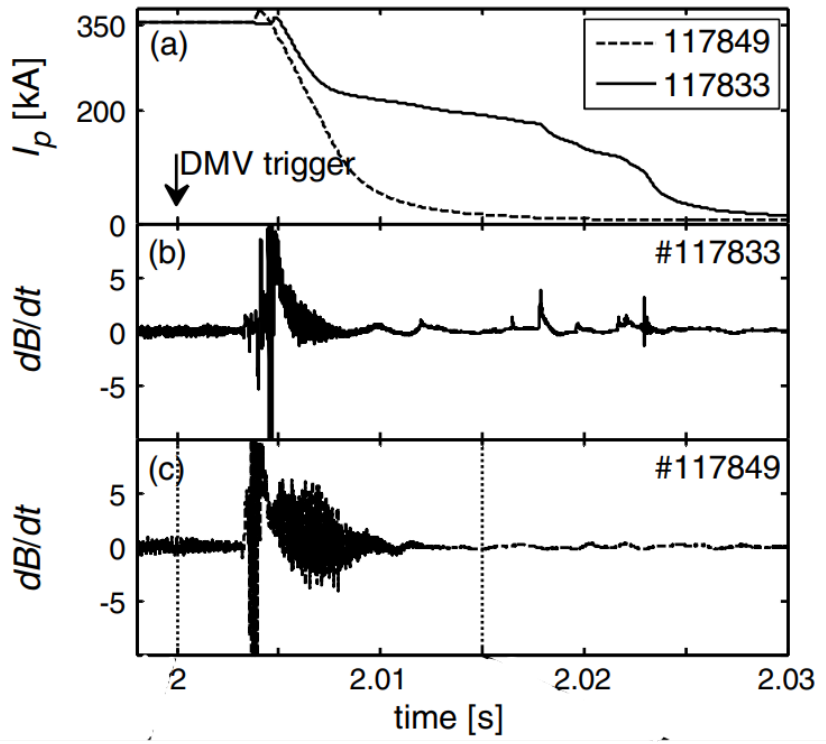


Fig. 2.3 a) Time evolution of the plasma current I_p in the absence (discharge number 117833, continuous curve) and presence (discharge number 117849, dashed curve) of large magnetic fluctuations. and Time evolution of the temporal variation s in the magnetic field in absence b) and presence c) of magnetic fluctuations. Reproduced from [33].

where a is the plasma minor radius, E is the ratio of the applied electric field to E_c, $q = rB_z/RB_\theta$ (where r is the minor radius, R is the major radius, B_z and B_θ are the toroidal and poloidal component of the magnetic field) is the safety factor, R is the major radius, p_{crit} is the critical momentum $p_{crit} = m_e c/\sqrt{E-1}$ [11], $I_A = 4\pi m_e c/\mu_0 e = 0.017$ MA is the Alfvèn current and τ is the collision time for the relativistic electrons.For JET plasmas, the level of magnetic perturbations required for RE radial diffusion is $\delta B/B \approx 10^{-3}$ and this value is valid also for other devices [35].

2.2.4 Runaway electrons losses to the wall

Significant RE losses due to enhanced radial transport by magnetic fluctuations can be benign for the PFC since RE would be distributed over a large area of a PFC. However, if a multi-MeV RE beam arrives at the wall, it can seriously damage the

components. The RE impact at the wall can cause local melting of the material and in extreme cases affect the cooling system of the components [36]. An example of material melting on a Tungsten limiter by RE beam after 400 discharges with disruption in $T-10$ is shown in Fig. 2.4.



Fig. 2.4 Observed melt damages of tungsten poloidal limiter after 400 disruptions in the tokamak T-10. Melting and craters on the tungsten plates at the torus outer board side. Reproduced from [37].

Since RE are characterized by energies in the order of tens of MeV, a RE beam can easily penetrate the PFC and interact with the material atomic structure. As a consequence, the energy carried by these electrons is deposited within the material through inelastic collisions with bound electrons, photon production, and elastic collisions with nuclei. These mechanisms are described in chapter 7.

In order to avoid severe damage to the PFC, RE mitigation strategies have to be used in the fusion devices. These strategies aim to reduce RE generation and enhance RE losses through the mechanisms described in this section. Section 2.3 briefly describes these mitigation processes.

2.3 Runaway electron mitigation

During the thermal quench, the plasma thermal energy, W_{th}, is lost on a time scale lower than a millisecond causing high heat loads on the PFC. The abrupt change in the electron temperature induces an electric field which leads to the primary generation of RE if $E > E_c$. During the current quench, the magnetic energy stored in the poloidal magnetic field $W_{mag} = \frac{1}{2}LI_p^2$ is released causing a Joule heating of the plasma and conducting structures [38]. This plasma reheating leads to a current quench duration large enough for a VDE to shift plasma to the divertor region causing extreme electromagnetic forces and thermal loads. Moreover, a RE avalanche occurs during this phase causing the formation of a multi-MA RE current which can further increase the damage to the plasma-PFC contact area. These consequences of disruption have to be avoided for the successful operation of future fusion devices with higher plasma currents than present Tokamaks.

A Disruption mitigation system (DMS) is designed to avoid three major disruption consequences: extreme thermal loads on PFC, electromagnetic forces, and RE generation and localized losses [39]. In other words, a DMS consists of techniques aiming to radiate the plasma energy, $W_{th} + W_{mag}$, through ultraviolet and visible radiations in an isotropic manner, increase the critical electron density above a certain limit to avoid RE generation and perturb the magnetic field lines to deconfine the RE seed. The focus of this section is to underline the effects of such techniques on RE generation and mitigation.

The principal mechanisms under investigation by the fusion community are massive gas injection (MGI), shattered pellet injection (SPI), resonant magnetic perturbation (RMP) and passive RE mitigation (REMC) coils [40]. For DEMO also certain structures called sacrificial limiters are planned to limit the damage induced by RE. These stratergies are described in the following subsections.

2.3.1 Massive gas injection

The massive injection of noble gases influences the evolution of disruption causing a rapid density increase and cool-down of the plasma by dilution and radiation through collision of plasma species with impurity atoms [41]. Therefore, it is used for RE suppression and reduction of heat loads in current fusion devices. Ideally, the

impurities are injected in a pre-thermal quench plasma to deliver sufficient neutral atoms to the core for a successful disruption mitigation.

An estimate of the critical electron density allowing for complete suppression of RE (primary and secondary) can be found in [41],

$$n_c = \frac{4\pi\varepsilon_0^2 m_e c^2}{e^3 \ln\Lambda} E = 1.961e22\frac{E}{\ln\Lambda} \tag{2.14}$$

where E is the toroidal electric field during the current quench,

$$E = \frac{L}{2\pi R}\frac{I_p}{\Delta t_{cq}} \tag{2.15}$$

with $L = \mu_0 R l_i/2$ the plasma internal inductance, R the major radius, I_p the plasma current and Δt_{cq} the duration of the current quench. For ITER, assuming $l_i = 0.9$, $I_p = 15MA$ and $\Delta t_{cq} = 35.6$ ms, the critical density accounting for both free and bound electrons is in the order of 10^{22} which is three order magnitude higher than the flat-top design value [41].

On the other hand, the radiation power of an injected gas can be evaluated as [30],

$$P_{rad} = n_e n_{imp} L_{imp} \tag{2.16}$$

where P_{rad} is the radiation from the impurity atoms, n_{imp} is the impurity density and L_{imp} is the impurity cooling rate. It is clear that a large free electron density increases the radiated power according to Eq. 2.16.

The injection of high Z impurities might seem an ideal option to reach a $n_c \approx 10^{22}\ m^{-3}$ due to the large number of bound electrons in the impurities. Also, high Z impurities would lead to a strong cooling rate of the plasma according to eq. 2.16. However, the injection of high Z impurities, such as Argon, leads to the generation of RE in certain conditions. This is because the effectiveness of an injected gas in suppressing the RE generation and radiating the plasma energy depends on its ability to reach the plasma core (hotter region).

The ratio between the gas atoms able to reach the plasma core and the total injected atoms is known as the mixing efficiency or assimilation fraction. A higher assimilation factor means a larger amount of impurity atoms can reach the plasma

center, where it ionizes, radiating the plasma energy and increasing the electron density to prevent RE generation. Argon has a mixing efficiency of around 3%, therefore, it is not possible to reach the desired n_c injecting an Argon quantity that is sustainable for the pumping system. As a consequence, the suppression of RE generation is not possible. On the other hand, a mixture of deuterium and argon has an efficiency of around 15% due to the ability of deuterium to penetrate deeper in the plasma [42]. Pure deuterium has a higher assimilation factor, however, it leads to a longer plasma shutdown time due to its lower cooling rate [30]. Longer current quench leads to damage to the vacuum vessel structure due to electromagnetic forces caused by the plasma vertical movement.

Since Argon causes rapid cooling of the plasma, but is not able to prevent RE formation, it is being used in the current Tokamaks to study runaway electron generation and mitigation physics through mitigated disruption. In other words, Argon is injected into a healthy plasma to cause a rapid loss of thermal energy leading to a thermal quench with the following RE generation. One of the most studied experiments where this has been used is JET pulse 95135 described in chapter 3.

The penetration of gas neutrals into the plasma is influenced by the safety factor profile (q). It has been shown in Ref. [43] that when the gas jet reaches a magnetic flux surface where $q = 2$ an MHD instability is triggered which causes a sudden loss of plasma core energy and initiates the thermal quench. This is because a massive injection of impurities in the plasma causes drastic changes in plasma temperature, density, and current profiles giving rise to large MHD instabilities [44]. As a consequence, the gas atoms are not able to reach the plasma core where the plasma thermal energy is concentrated before a TQ takes place. Part of the energy lost in this process ionizes the neutral gas atoms around the $q = 2$ surface preventing the impurity atoms from penetrating further. In case this flux surface is near the plasma edge, the gas jet would be strongly opposed in its path toward the center of the plasma. Similar conclusions have also been drawn in [38] through MHD modeling of the disruption physics in MGI mitigated disruptions.

Furthermore, in large-scale reactors such as ITER, an impurity gas injected through MGI would not be able to penetrate deeply into the plasma due to the gas diffusivity once it reaches the plasma edge [44]. However, an MGI system is still considered for compact fusion devices like SPARC [45].

Due to the reasons underlined so far, an MGI system is not considered to be used for disruption mitigation in large-scale reactors such as ITER [44]. Indeed, a shattered pellet injection system has been studied to improve the effectiveness of the disruption mitigation system and it represents the current stratergy for mitigating disruption consequences.

2.3.2 Shattered pellet injection

Impurity injection through a shattered pellet injection (SPI) is more efficient in cooling down the plasma and suppressing the RE generation [46]. Therefore, it represents a better candidate for a disruption mitigation scheme. In particular, an SPI system guarantees a factor 2 higher assimilation of the impurity with respect to an MGI system [40].

The SPI technique in Tokamaks involves injecting solid cryogenic pellets, which are shattered before entering the plasma to avoid damage to the first wall and to enhance pellet ablation. These pellets, typically made of impurities like deuterium or neon, have specific lengths and diameters tailored to the disruption characteristics of the Tokamak. The injection velocity is precisely controlled to ensure optimal penetration and distribution within the plasma. Shattering the pellets increases their surface area, facilitating more efficient and rapid ablation, which in turn cools the plasma and increases its density, effectively stabilizing it and mitigating disruptions [46].

In Ref. [44], a comparison is carried out between experiments utilizing Argon MGI and Argon SPI. The results indicated that SPI systems are characterized by deeper penetration into the plasma. Additionally, it was observed that impurities injected by SPI trigger larger MHD instabilities with respect to the MGI at the flux surface with a safety factor of 1.

In Fig. 2.5, a comparison of the time evolution of electron density at the plasma edge (a) and core (b) can be seen for Argon injected via SPI (blue) and MGI (red). For SPI injections, the density increases earlier during penetration compared to MGI, followed by a rapid rise during the CQ. The core density in the SPI case reaches higher levels than in the MGI case, while the edge density increase is much lower, indicating that impurities injected through SPI penetrate deeper into the plasma. Specifically, the radial density ratio n_{core}/n_{edge} for SPI can reach about 4, whereas

for MGI it is around 1 during CQ. This suggests that gas impurities from MGI tend to remain near the plasma edge and are ionized by the energy lost due to MHD instabilities as observed in Ref. [43]. Additionally, a significant increase in the electron density is observed during the CQ phase in both SPI and MGI shots. This demonstrates that ionization occurs mainly during the lower-temperature CQ plasma in the J-TEXT Tokamak. This is because the plasma thermal energy in J-TEXT is $1/10$ of the magnetic energy [44].The magnetic energy lost during the CQ is sufficient to ionize a significant amount of neutral impurities.

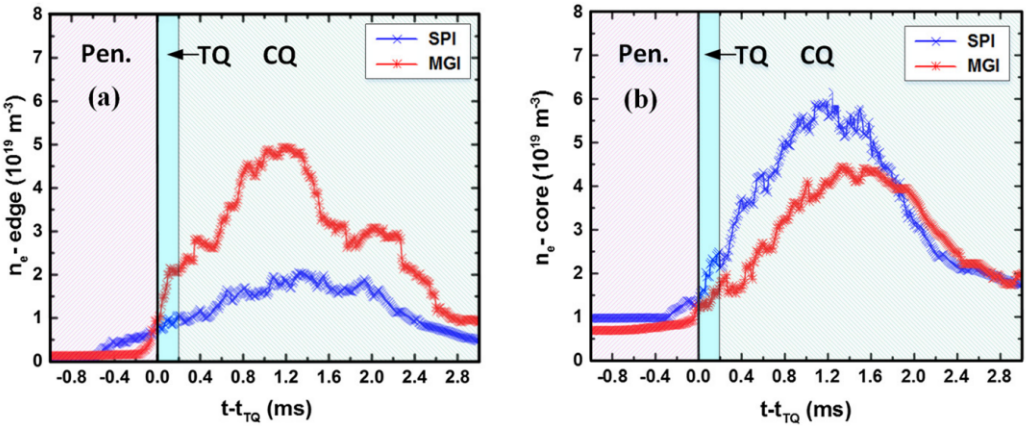


Fig. 2.5 Comparison of the time evolution of electron density, n_e, at the plasma edge a) and core b) for Argon injected via SPI (blue curve) and MGI (red curve). At $t - t_{tq} = 0$ the disruption take place with a TQ followed by a CQ. Reproduced from [44]

A higher core electron density allows for more efficient collisional mitigation of RE since it increases the critical electric field necessary for RE generation. As a consequence, as shown in Fig. 2.6 (a), the decay rate of the plasma current I_p is much higher in the SPI case (red) with respect to the MGI case (blue) [46]. This is because the maximum of the density expressed in terms of the line integrated electron density (density of the plasma along a chord or line passing through the center of the torus) (b) in the case of an SPI is reached earlier with respect to the MGI case. Indeed, the rapid increase in the density with SPI means the impurities reach the core in the earlier phase of the avalanche phenomena when the toroidal electric field is at its maximum.

The injection of impurities through MGI and SPI gives rise to large MHD instabilities which may play a major role in deconfining a RE current. These MHD instabilities occur also in the absence of impurity injection during a TQ and are responsible for the loss of plasma thermal energy. However, the presence of impurity

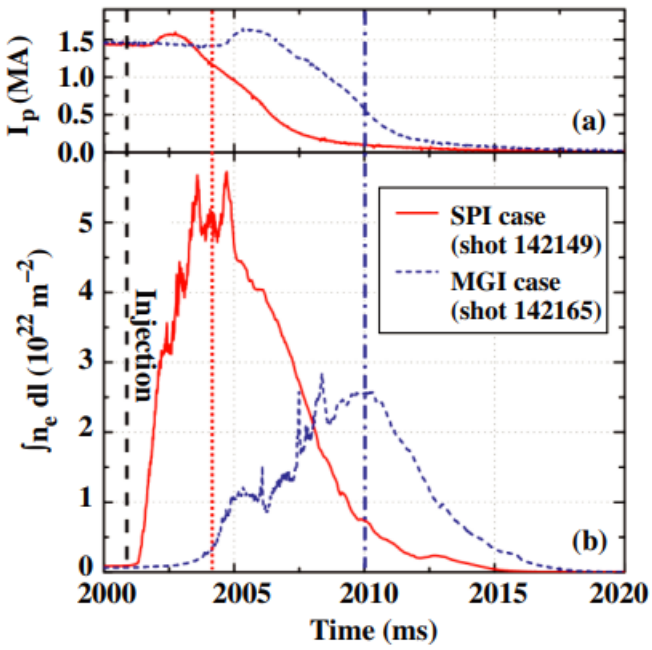


Fig. 2.6 a) Time evolution of the plasma current with MGI mitigated disruption (blue dashed curve) and SPI mitigated disruption (red continuous curve). b) Time evolution of the line integrated electron density with the same colors as in a). Reproduced from [46].

increases the severeness of these instabilities. In certain conditions, as in JET pulse 95135 which is described in chapter 3, the deuterium SPI injection in a mitigated disruption caused by Argon injection has led to a termination of RE current caused by a large MHD instability without causing any damage to the PFC. Apart from these naturally occurring MHD instabilities, it is possible to initiate plasma MHD activity through Resonant Magnetic Perturbation (RMP) or Runaway Electron Mitigation (REMC) coil to deconfine RE populations on open field lines [40].

2.3.3 Resonant Magnetic Perturbation and Runaway Electron Mitigation Coil

The MHD instabilities arising during the TQ after or in the absence of impurities injection can deconfine RE seeds generated through the primary generation mechanism [47]. However, when the magnetic flux surfaces reformation occurs due to the safety factor profile flattening during the CQ any remnant RE seed can give rise to the avalanche. The application of magnetic field perturbations through external coils

allows to deconfine RE by forcing an opening of the nested magnetic flux surfaces [40]. These coils aim to apply a level of magnetic perturbation $\delta B/B \approx 10^{-3}$ which can destroy the magnetic surfaces as described in subsection 2.2.3. In this way, the RE seeds are lost without giving rise to the RE avalanche. The scope of this subsection is to give an overview of the mitigation techniques based on enhancing plasma MHD instabilities. Further details about the nature of the MHD instabilities and their evolution are given in chapter 3.

The magnetic perturbations are applied through resonant magnetic perturbation coil (RMP) or passive RE mitigation coil (REMC). The RMP coils have been used in JT-60U [48] and TEXTOR [49] experiments to deconfine RE losses while the effectiveness of a passive REMC has been shown only through MHD simulations for medium-scale reactors like SPARC and DIII-D [47] [50]. Indeed, as observed in Ref. [51] the RMP coils can cause a stochastization of the magnetic flux surfaces only at the plasma edge in large-scale Tokamak like ITER.

The cross-section of the ITER RMP coils is shown in blue in Fig. 2.7 a) whereas the unperturbed plasma magnetic equilibrium is shown in green. A current flow in these could generate a perturbation field that decays radially towards the inside of the plasma As it can be observed in Fig. 2.7 b) in ITER, due to the large major radius, a magnetic perturbation, expressed in terms of the flux-surface averaged magnetic perturbation, larger than 10^{-3} is only possible for the region outside of the magnetic flux surface with toroidal flux $\psi = 0.5$. This is obtained using the maximum allowed current with a configuration of the coils having n=3 lead toroidal mode number (black line). The dashed blue and red lines depict the perturbation radial variation with n=9 specific configuration. Details about these specific configurations can be found in [35]. Configurations with n=3 toroidal mode number were found to create larger magnetic islands in the plasma edge with respect to a configuration with n=9 [35]. Larger magnetic structures lead to higher magnetic field stochastization which is beneficial for RE radial diffusion.

The effect of the edge $\psi > 0.5$ stochastization on the RE losses is shown in Fig. 2.8 [52] where the effect of island structures on RE losses time can be appreciated as well. Indeed, as can be observed in Fig. 2.8 a) showing the RE loss time as a function of starting position (ψ, θ) where $\theta = atan^2(Z,R)$ (in rad), RE localized in a region with preserved magnetic islands $(\psi = 0.5)$ are characterized by longer loss times as indicated by the black dots. These islands are characterized by $m/n = 7/6$

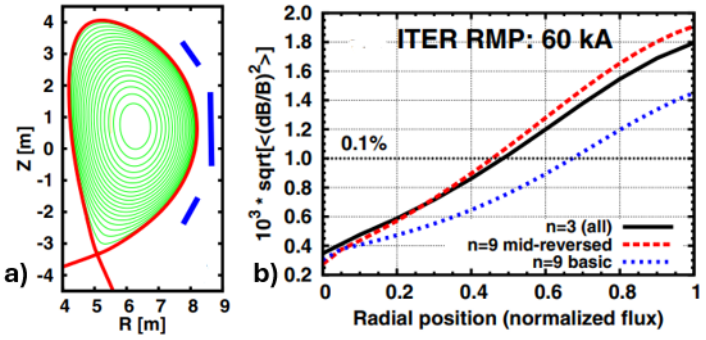


Fig. 2.7 a) Cross-section of the ITER RMP coils in blue and the unperturbed plasma magnetic equilibrium in green. b) flux-surface averaged magnetic perturbation as a function of radial position for n=3 configuration (black curve) and n=9 configurations (dashed lines). The current driven in the RMP coils is 60 kA. Reproduced from [35].

where the other broken islands shown in (a) have $m/n = 4/3$ and $m/n = 5/3$ with m and n being the poloidal and toroidal mode numbers. This translates into a lower percentage of particles lost present around this flux surface as shown by the blue line in Fig. 2.8 b). On the other hand, RE having an initial energy of 1 MeV presents on flux surfaces with $\psi > 0.5$ are almost totally lost in a configuration called $'B'$ in the figure, with n=3 toroidal mode number.

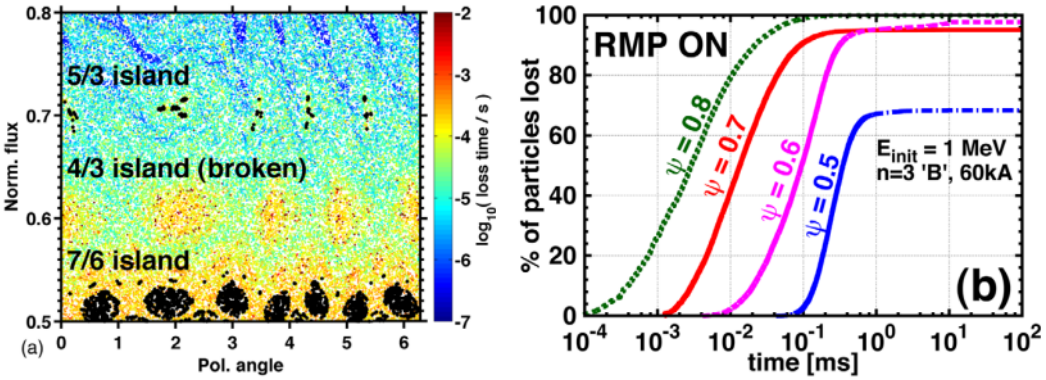


Fig. 2.8 a) RE loss time in logarithmic scale as a function of starting position (ψ, θ) where $\theta = atan^2(Z,R)$ in radiants. b) Time evolution of particles lost percentage on the different flux surfaces $\psi = 0.5$ (blue), $\psi = 0.6$ (magenta), $\psi = 0.7$ (red), $\psi = 0.8$ (green) with particle initial energy of 1 MeV in configuration with n=3 called 'B'. Reproduced from [52]

With respect to an RMP coil which requires an external current supply to generate a perturbation field, in a passive REMC coil the current is provided by the plasma itself during a disruption. The design of a passive REMC is based on the concept proposed in Ref. [53] and implemented in a cylindrical geometry in Ref. [54]. The

concept involves designing the wall so that any toroidal current it carries is compelled to follow a helical path. During a disruption, the induced toroidal electric field generates helical currents in the wall, leading to the formation of magnetic islands in the plasma outer region through magnetic field perturbation. Once the magnetic perturbation is generated the RE deconfinement works in the same way as with RMP coils. Indeed, the overlap of the islands causes magnetic field stochastization which increases runaway electron losses counterbalancing the RE avalanche exponential growth.

A stochastization of the core flux surfaces through RMP coils would require stronger currents, but this is not feasible due to the construction limits [53]. Nevertheless, edge stochasticity can trigger MHD instabilities in certain conditions that cause an RE flush out from the plasma core [54]. For instance, this is possible by combining the MHD instabilities triggered by impurities injected through MGI or SPI with magnetic perturbation induced by an RMP [35].

2.3.4 Sacrificial limiters

The consequences of a RE beam impact on the Tokamak first wall increase with increasing complexities of the Wall in future Tokamaks. In present fusion devices and ITER, the FW acts as a barrier to high radiation and particle loads exiting from the plasma. Along with it, FW is used to keep the vacuum in the plasma chamber. Therefore, there are no specific constraints related to the thickness of the FW even if the ITER FW will have some ports for testing the breeding blanket modules. In DEMO, however, the FW initial protective layer should have a limited thickness since it will act mainly as a breeding blanket. This blanket will serve two main purposes which are the production of tritium for the reactor tritium self-sufficiency and extraction of thermal power to generate electricity.

The requirements for the DEMO FW initial layer are, therefore, multiple. Indeed, the materials need to operate in a high neutron environment, as the neutrons generated from fusion reactions are essential for both tasks. In addition, the structure must not only minimize damage to the underlying structures but also allow sufficient high-energy neutrons to pass through it to facilitate tritium production and power extraction via neutron slowing down. Consequently, the FW protective layer will be a relatively thin structure (about 2 mm), capable of handling moderate heat loads. On

the other hand, the Breading blanket FW design of DEMO can withstand stationary heat loads around $1 - 1.5\ \mathrm{MW}/m^2$ [55]. This design underscores the necessity for systems that can mitigate plasma events that might otherwise damage the reactor components. Among the various events that could damage the components, here, the focus is on the RE.

If a multi-MeV RE beam arrives at the FW without being mitigated by the various techniques of a DMS it can cause severe damage to the Breeding blanket. Therefore, a system of sacrificial limiters is under design for the EU-DEMO and a sketch of this system is shown in Fig. 2.9 [56] [57]. Fig. 2.9 a) shows the poloidal location of the 4 different limiters on a DEMO sector. The total number of sectors is 8 and each of these sectors has 4 limiters at different poloidal locations as can be observed in Fig. 2.9 b).

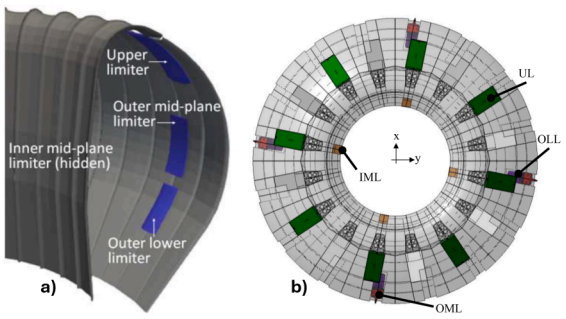


Fig. 2.9 a) Poloidal location of the 4 different limiters on a DEMO sector. b) Top view of the plasma chamber showing the limiters in the 8 DEMO sectors. Reproduced from [56, 57]

The dimensions of the limiters together with the surface characteristics and inclination area result from different studies on DEMO transient events such as RE impact. Moreover, RE-induced damage studies are in a preliminary phase [55]. These studies are focused on understanding the surface and in-depth energy deposition caused by an RE beam impact with the consequent thermal evolution. The main objective is to assess the capability of the limiters to stop the RE from depositing the energy in the breeding blanket.

Chapter 3

MHD instabilities effects on Runaway electron termination

Magnetohydrodynamic (MHD) instabilities, such as kink or tearing instability, are crucial in terminating runaway electrons in fusion plasmas [58][59]. These instabilities, resulting from the interplay between plasma and magnetic field structure, can halt the runaway electron beam prior to the effectiveness of mitigation strategies or can be utilized to reduce the risks posed by runaway electrons.

A kink instability occurs when the plasma current becomes too peaked along the magnetic axis, resulting in a q value on the axis (central safety factor) of less than 1 ($q_0 < 1$). This type of instability, known as an internal kink mode, mainly affects the central region of the plasma. On the other hand, when the safety factor at the edge of the plasma (q_{edge}) falls below 2, an external kink mode occurs. The external kink mode can cause significant disruptions in a tokamak, leading to loss of plasma confinement and potential interaction with the vessel walls. Theoretical principles of kink modes can be found in Ref. [60], and a demonstration of the kink instability effects on RE termination can be found in Ref. [58]. However, for the purpose of this discussion, the focus will be on the tearing instability.

A tearing instability causes the magnetic field lines in plasma to break and reconnect, forming magnetic islands. This process reduces the magnetic energy in the surrounding regions, leading to changes in plasma behavior and stability. A magnetic island is a topological change of the plasma magnetic field lines characterized by a set of nested flux surfaces surrounding a local magnetic axis. As these islands

expand, magnetic flux surfaces are drawn from above and below, converging at the x-points. These flux surfaces then separate, forming closed surfaces within the islands [60]. Magnetic islands can form in magnetically confined plasmas, such as those in Tokamaks, due to instabilities at mode rational surfaces with $q = m/n$. The poloidal mode number, m, refers to the number of perturbation oscillations around the toroidal plasma minor axis. In contrast, the toroidal mode number, n, refers to the number of perturbation oscillations around the toroidal plasma major axis. The MHD instabilities are characterized by a combination of poloidal and toroidal mode numbers (m,n).

The formation of the magnetic islands is represented in Fig. 3.1 starting from a toroidal plasma (a) characterized by a magnetic field with nested flux surfaces and finite shear, that is, $q(r)$ [60]. In addition, this configuration has a rational surface with $q = m/n$ where a tearing instability can occur. The toroidal plasma is cut open to form a cylindrical plasma (b) and laid out in a slab geometry (c). At this point, by constructing a hypothetical magnetic field with the same flux surfaces but zero shear (constant q=m/n everywhere) and subtracting this field from the original, a new magnetic field B_* can be defined which represents the deviation from the zero shear state (d). The poloidal, θ, component of B_* changes sign across the mode rational surface, highlighting the presence of shear. Introducing a small radial magnetic field perturbation, $B_x \sin(k_y y)$, with $k_y = m/a$ (where a is the dimension of the box along y), with a sinusoidal variation along the poloidal angle, θ, causes the field lines near the mode rational surface to move in a cyclic pattern (e). Where the radial field is positive, field lines just below the rational surface move upwards and rightward, crossing the surface and returning downward and leftward in regions of negative radial field. This repetitive movement forms magnetic islands, where field lines become trapped in closed loops. The point where the magnetic field line crosses the surface and returns is called the island X-point, whereas the center of these closed loops is called the island O- point. In the region far from the rational surface, the radial field cannot force the magnetic field lines to go through the rational surface. Consequently, a separatrix is formed by the last closed magnetic surface that separates the nested flux surfaces inside the island from the open surfaces above and below.

The fundamental process causing the magnetic field lines to reconnect and form a magnetic island is called magnetic reconnection. It is described in section 3.1 after introducing the physical model used to study this phenomenon both in resistive and

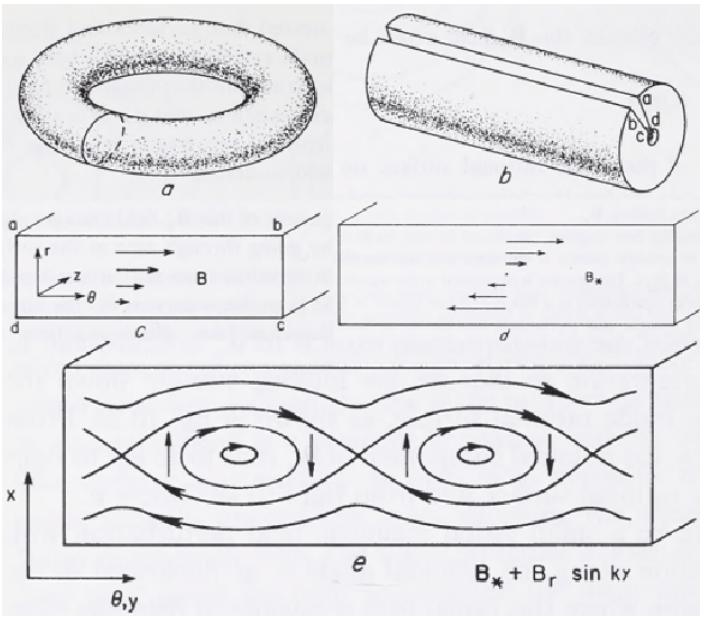


Fig. 3.1 Representation of the magnetic island formation starting from a toroidal plasma a), cut open b) and laid out flat c), with transformation to $B*$ d) and a radial magnetic field perturbation B_r to show the formation of magnetic islands e). Reproduced from [60].

nonresistive plasmas. The introduction of the physical models allows to describe the reconnection event with a single magnetic island in section 3.2 and multiple magnetic islands in section 3.3. In the latter case, the interaction between the magnetic islands can lead to a chaotic evolution of the magnetic field called magnetic stochasticity, where specific magnetic structures can act as magnetic barriers to the diffusion of the magnetic field lines. Moreover, magnetic stochasticity evolution follows different paths according to the background plasma parameters.

In a post-disruption plasma, since the RE generation is more intense in the plasma inner region due to higher temperatures, the RE current profile is more peaked with respect to the predisruption ohmic current [61]. Such a narrow current channel can give rise to MHD instabilities, and the mutual interaction of a RE current with these instabilities characterizes the stability of a postdisruption plasma [3]. On the other hand, mitigation strategies such as RMP and RMC are designed to deliberately perturb the plasma magnetic field. Enhancing MHD instabilities causes the loss of RE seeds, thereby preventing the formation of a multi-megaampere (MA) RE beam via the avalanche phenomenon. The destabilization of the seed population through these techniques reduces the likelihood of a full-scale runaway electron avalanche, which is critical for maintaining plasma stability and protecting the

reactor, as explained in subsection 2.3.3. In addition, techniques like MGI and SPI can terminate fully grown RE beams. These methods introduce impurities or cooling agents into the plasma, which can initiate MHD instabilities that lead to the safe termination of RE beams without causing damage to the reactor walls.

The mutual influence between a RE current and magnetic reconnection instability is described in section 3.4 first considering a slab geometry with a single magnetic island and then considering a toroidal geometry with multiple magnetic islands to show the effects of magnetic perturbations which can rise due to SPI injection on a RE population. The influence of the interaction between multiple magnetic islands on a RE current is described through the benign termination modeling done in Ref. [25]. Finally, an Argon MGI triggered disruption experiment is presented in section 3.5 to present the physics behind the RE benign termination observed in MHD simulations shown in [25].

3.1 Reduced MHD equations

MHD instabilities, characterized by scale lengths similar to the plasma size, are described by the MHD equations [62]. These equations apply to low-frequency, collision-dominated phenomena with spatial scales larger than the Debye length. The first restriction neglects the displacement current in Maxwell's equations. The second restriction implies that the pressure tensor can be approximated as a gradient, $\nabla \mathbf{p} = \nabla p$. The third restriction ensures quasi-neutrality, with $n_e \approx n_i$. Lastly, it is assumed that the ratio $m_e/m_i \to 0$. Therefore,

$$\frac{\partial \rho}{\partial t} + \nabla \cdot \rho \mathbf{v} = 0 \tag{3.1}$$

$$\frac{d(\rho v)}{dt} = -\nabla p - \frac{1}{c}\mathbf{J} \times \mathbf{B} \tag{3.2}$$

$$\mathbf{E} + \frac{\mathbf{v} \times \mathbf{B}}{c} = \eta \mathbf{J} \tag{3.3}$$

$$\nabla \times \mathbf{E} = -\frac{1}{c}\frac{\partial \mathbf{B}}{\partial t} \tag{3.4}$$

$$\nabla \times \mathbf{B} = \frac{4\pi \mathbf{J}}{c} \tag{3.5}$$

where 3.1 is the continuity equation, 3.2 is the momentum equation, 3.3 is the ohm law, 3.4 is the Faraday equation and 3.5 is the Ampèrè-Maxwell law. The equations are written with the CGS units to be consistent with the notation adopted in the numerical tools used for the work. Assuming the approximation of an incompressible fluid, this set of equations can be closed by an equation of state which reduces Eq. 3.1 to $\nabla \cdot \mathbf{v} = 0$.

The full MHD equations 3.1-3.5 can be further simplified, considering that the magnetic field in a Tokamak is almost uniform and unidirectional. In other words, the toroidal component of the magnetic field is much larger than the other components, which allows writing the magnetic field as a sum of two components $\mathbf{B} = \mathbf{B}_0 + \mathbf{B}_\perp$ where $\mathbf{B}_0$ is the toroidal component and the $\mathbf{B}_\perp$ is the perpendicular component of the magnetic field with $\frac{B_\perp}{B_0} = \varepsilon \ll 1$. Moreover, the presence of a strong toroidal component allows to assume a negligible plasma thermal pressure due to the dominance of the plasma magnetic energy over the thermal and kinetic energy [62]. These considerations lead to deriving the reduced resistive and nonresistive MHD (RMHD) equations widely used to study MHD instabilities [62].

3.1.1 Resistive RMHD equations

The detailed derivation of the resistive RMHD equations can be found in literature [63]. Here, the final result of this derivation normalized over the Alfvèn time ($\tau_A = L/v_A$ where v_A is the Alfvèn velocity) and the characteristic length L of variation of the equilibrium magnetic field is reported only. The equations are written assuming a magnetic field $\mathbf{B} = B_0\mathbf{e}_z + \nabla\psi \times \mathbf{e}_z$, where $B_0 = 1$ and a velocity field $\mathbf{v} = -\nabla\varphi \times \mathbf{e}_z$,

$$\frac{\partial \psi}{\partial t} + [\varphi, \psi] + \eta j - \frac{\partial \varphi}{\partial z} = 0 \tag{3.6}$$

$$\frac{\partial U}{\partial t} + [\varphi, U] - [j, \psi] - \frac{\partial j}{\partial z} = 0 \tag{3.7}$$

$$j = -\nabla^2{}_\perp \psi, U = \nabla^2{}_\perp \varphi \tag{3.8}$$

where $\nabla^2{}_\perp = \partial_x^2 + \partial_y^2$ and $[f,g] = \partial_x f \partial_y g - \partial_x g \partial_y f$ are the Poisson brackets. The Eq. 3.6 is the generalized ohm law with the normalized resistivity given by $\eta = \eta_\parallel R_0/\mu_0 v_A a^2$ with $\eta_\parallel$ being the plasma parallel resistivity, R_0 the major radius,

a the minor radius. The Eq. 3.7 is the momentum equation. The fields ψ and φ are the magnetic flux and the stream function, respectively, while $j = -\nabla^2\psi$ is the plasma current density, and U is plasma vorticity.

The equations 3.6-3.8 are valid for a 3D slab geometry (x, y, and z) and are used to study the MHD instabilities from a fundamental point of view. At the same time, specifically for Tokamaks, the following normalized equations written in toroidal coordinates (R, Z, ϕ) are used [64],

$$\frac{\partial \psi}{\partial t} = \eta\, j - F_0 \frac{\partial \varphi}{\partial \phi} - R[\varphi, \psi] \tag{3.9}$$

$$\nabla \cdot \left[\rho R^2 \nabla_{pol} \frac{\partial \varphi}{\partial t}\right] = \frac{1}{R}\left[R^4 \rho U, \varphi\right] - \frac{1}{2R}\left[R^2 \rho, R^2 |\nabla_{pol}\varphi|^2\right] + \frac{1}{R}\left[\psi, j\right] - \frac{F_0}{R^2}\frac{\partial j}{\partial \phi} \tag{3.10}$$

$$j = R^2 \nabla \cdot \left(\frac{1}{R^2}\nabla_{pol}\psi\right), U = \nabla \cdot \nabla_{pol}\varphi \tag{3.11}$$

Where F_0 is a constant, ρ is the plasma density, and ∇_{pol} is the gradient in the poloidal (R, Z) plane. The equations are written assuming a magnetic field $B = \frac{1}{R}\left[F_0 e_\phi + \nabla\psi \times e_\phi\right]$ and a velocity field $v = -R\nabla\varphi \times e_\phi$.

3.1.2 Non resistive RMHD equations

In plasmas with very low resistivity, known as collisionless plasmas, the resistive RMHD equations are unsuitable for describing the reconnection process. In this case, the generalized Ohm law 3.6 has to be modified to account for the electron inertia effects, which becomes the driver mechanism for the magnetic reconnection [65]. Consequently, the system is no longer described by a single-fluid model considering electrons and ions as a single fluid. Instead, a two-fluid model is adopted that treats the ions and electrons separately. The full derivation of the two fluid RMHD equations can be found in [65]. The inclusion of the electron inertia modifies the Ohm's laws reported in Eq. 3.6 which now becomes,

$$\frac{\partial F}{\partial t} + [\varphi, F] - \rho_s^2[U, \psi] + \eta\, j + \frac{\partial \varphi}{\partial z} + \rho_s^2 \frac{\partial U}{\partial z} = 0 \tag{3.12}$$

$$\frac{\partial U}{\partial t} + [\varphi, U] - [j, \psi] - \frac{\partial j}{\partial z} = 0 \tag{3.13}$$

$$F = \psi + d_e^2 j = \psi - d_e^2 \nabla^2{}_\perp \psi, U = \nabla^2{}_\perp \varphi \tag{3.14}$$

Where $d_e = c/\omega_{pe} = c/\sqrt{4\pi n_e e^2/m_e}$ is the electron skin depth which accounts for the electron inertia and $\rho_s = \sqrt{T_e/m_i}/\omega_{ci}$, accounting for the electron temperature contribution being not negligible in the case of low resistivity, is the ion sound Larmour radius.

The RMHD equations (3.6-3.8, 3.9-3.11, 3.12-3.14) are used to describe a fundamental process occurring in astrophysical and laboratory plasma known as magnetic reconnection [66]. In fusion plasmas, this phenomenon is responsible for resistive tearing instabilities that can initiate a plasma disruption or perturb the magnetic field lines, leading to a loss of plasma confinement and are described using (3.6-3.8, 3.9-3.11).

The evolution of a resistive or a collisionless magnetic reconnection event can be explained through the generalized Ohm law. For simplicity, we will consider the resistive equation in a 2D slab geometry,

$$\frac{\partial \psi}{\partial t} + [\varphi, \psi] = -\eta j \tag{3.15}$$

With negligible resistivity, Eq. 3.15 expresses the magnetic flux conservation and the magnetic field coupling with the fluid motion [62]. This is known as the Alfvèn theorem, which implies that the magnetic topology cannot change, so the reconnection event cannot occur. However, in the presence of a finite resistivity, such as in a Tokamak plasma or electron inertia in collisionless plasmas, the magnetic field motion is decoupled from the plasma motion, and the magnetic field can reconnect, leading to the formation of a magnetic island as previously shown in Fig. 3.1. This process converts magnetic energy into thermal and kinetic energy.

3.2 Single helicity reconnection event

A single helicity reconnection event is a process where the magnetic field lines with a specific helicity, α (defined by the ratio of a toroidal, $k_z = n/L_z$ and poloidal, $k_y = m/L_y$, wave vector numbers) break and reconnect. This reconnection event is usually studied assuming a Harris sheet [67] with an equilibrium magnetic field $B = -\tanh(x)\mathbf{e}_y$, a flux function $\psi = \log(\cosh(x))$, a stream function $\varphi = 0$ and in

the limit of $k_z = 0$, therefore $n = 0$. This limit allows us to treat the problem in a 2D slab geometry where the radial profile of the different fields is symmetric with respect to the rational surface at $x = 0$.

Linearizing the Eq. 3.6-3.8 and solving for the perturbed quantities,

$$\tilde{\psi} = \delta\psi(x)\exp(ik_y y + \gamma t), \tilde{\varphi} = \delta\varphi(x)\exp(ik_y y + \gamma t) \tag{3.16}$$

Where γ is the growth rate of the instability, two ordinary differential equations for $\delta\psi$ and $\delta\varphi$ can be obtained. The solution of this set of equations in the region where the reconnection occurs, called the inner layer, is referred to as the inner solution. Outside of this region, called the outer layer, the set of equations is solved, neglecting the resistive term in the equation. This gives the outer solution. The dispersion relation for the tearing instability can be obtained by matching these two solutions at the boundary between the two layers through the asymptotic matching method. Here, we focus on the small Δ' regime, that is, $\Delta'\eta^{1/3} \ll 1$ where Δ' depends on the solution for ψ in the outer layer and expresses its jump across the rational surface. In particular, the parameter Δ' measures the level of instability, with a larger value indicating a more unstable mode. For a Harris sheet and slab geometry, Δ' depends only on the k_y vectors and is given by [68],

$$\Delta' = 2\frac{1-(k_y)^2}{k_y} \tag{3.17}$$

The dispersion relation for the linear growth of the tearing instability in this regime is [69],

$$\frac{\gamma^{5/4}}{\eta^{3/4}k_y^{1/2}} = 0.47\Delta' \tag{3.18}$$

In the case of finite resistivity, a correction has to be made to Eq. 3.18, and the dispersion relation becomes [70],

$$\frac{\gamma^{1/4}(\gamma - 2b\eta)}{\eta^{3/4}k_y^{1/2}} = 0.47\Delta' \tag{3.19}$$

where $b = \frac{\psi_{eq}^{IV}}{\psi_{eq}^{II}}|_{x=0}$, ratio between the fourth and second derivative of ψ_{eq}. The full derivations of the dispersion relation for tearing instability can be found in [69] [70].

The linear phase of the tearing instability evolution is characterized by an exponential growth. The island enters the nonlinear regime when the island width becomes larger than the resistive layer present on the current layer and determined by,

$$\delta_1 = \gamma^{1/4}\eta^{1/4}k_y^{-1/2} \tag{3.20}$$

In the nonlinear phase, the instability enters the so-called Rutherford phase [71], during which it undergoes a slower algebraic growth until the magnetic island reaches saturation. The island reaches saturation when the system magnetic energy is no longer lowered by further island growth [3].

If a finite value k_z is adopted, a finite value of the helicity makes the problem 3D. However, it is still possible to study the reconnection event in a 2D approximation through a transformation of the sheared component of the magnetic field B_y to $B_y - \alpha$ corresponding to a rotation in the (y,z) plane [72]. In this case, the rational surface is located at a finite value of the x coordinate, and the field profiles are nonsymmetric with respect to the rational surface. Indeed, the equilibrium magnetic field is $B = -\tanh(x)\mathbf{e}_y - \alpha$, the flux surface is defined by $\psi = \ln\cosh(x) + \alpha x$.

3.3 Multiple helicity reconnection event

In a Tokamak, the magnetic field topology is characterized by the presence of multiple magnetic islands (multiple helicities), which causes large MHD instabilities responsible for the discharge termination during a disruption [58] [59]. Multiple helicity refers to the situation where various sets of (m,n) modes grow simultaneously in the plasma, leading to several helical perturbations with different winding patterns coexisting.

In the presence of multiple helicites, the system is characterized by a quasi-linear evolution where the growth of the primary modes causes the generation of secondary modes through the modes' nonlinear coupling. Since the nonlinearities present in Eq. 3.12 3.13 represented by the Poisson brackets are quadratic, the generation of

an (m,n)-mode is given by the coupling of a $(m-h,n-k)$ mode with a (h,k) mode. For instance, a (2,2) mode is generated by coupling a (2-1, 2-1) mode with itself. During the nonlinear evolution, a strong coupling between modes with different helicities occurs, triggering the so-called magnetic field stochastization [72].

3.3.1 Magnetic stochasticity

Without stochasticity, the field lines trajectories can be obtained through the solution of Hamilton equations [72]. This is possible by writing the magnetic field lines equations $dx/B_x = dy/B_y = dz/B_z$ in a Hamiltonian form with the Hamiltonian function proportional to the flux function $K = \psi(x,y,z)/B_0$ where x and y are conjugate variables with y being the momentum corresponding to the x position, z is a "time" variable, and the true time t is a parameter. Therefore,

$$\frac{dx}{dz} = \frac{1}{B_0}\frac{\partial \psi}{\partial y} = \frac{B_x}{B_0} \tag{3.21}$$

$$\frac{dy}{dz} = -\frac{1}{B_0}\frac{\partial \psi}{\partial x} = \frac{B_y}{B_0} \tag{3.22}$$

These equations describe a dynamics system with only one degree of freedom. The interaction between multiple helicities introduces an additional degree of freedom, making the Eq. 3.21,3.22 not integrable. Therefore, the magnetic field line trajectories become stochastic or unpredictable, which can be observed through Poincaré maps showing the result of the numerical integration of the field line equations. The Poincaré map provides a detailed representation of the magnetic field chaotic regions for a given magnetic field line Hamiltonian. This representation is achieved by numerically integrating the Hamilton equations, starting from a large number of initial conditions and extending over significant values of the parameter (position) along the field lines, which acts as an effective time [73].

The evolution of magnetic stochasticity is depicted in Fig. 3.2 through Poincaré plots with normalized flux on the y-axis and normalized toroidal angle on the x-axis [74]. Without a strong coupling between the modes (left panel), the Poincaré map shows magnetic islands localized at different resonant surfaces given by (m,n) pairs. The neighbouring magnetic islands interact once the nonlinearities dominate (panel

b), leading to global chaos. This stochastic magnetic field behaviour can cause a radial diffusion of the magnetic field lines, which can leave the plasma region.

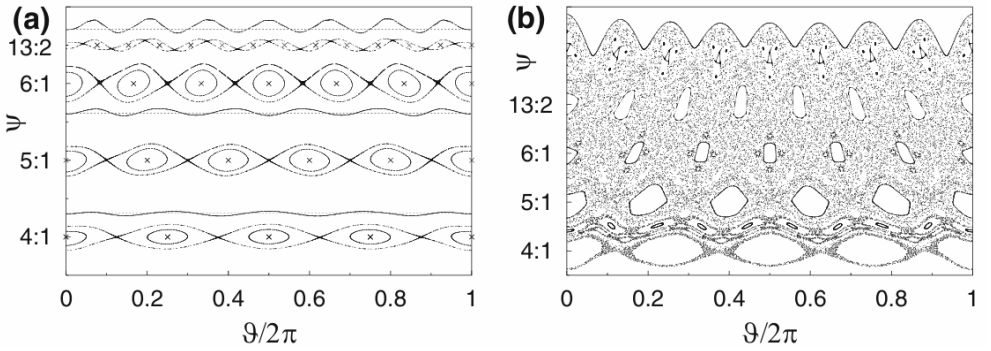


Fig. 3.2 Poincaré plots showing the evolution of magnetic stochasticity starting from (a) magnetic islands localized at different resonant surfaces and leading to (b) magnetic stochasticity with normalized flux on the y-axis and normalized toroidal angle on the x-axis. Reproduced from [74].

The criterion for the transition to global chaos is derived by Chirikov and is based on the overlapping of magnetic islands,

$$\sigma_{Chir} = \frac{w_{m,n} + w_{m+1,n}}{2\left|\psi_{m+1,n} - \psi_{m,n}\right|} \geq \sigma_c \tag{3.23}$$

Where the numerator is the average width of neighbouring magnetic islands while the denominator is the distance between them, once the average width of the islands becomes greater than the average distance, the Chirikov parameter σ_{Chir} becomes larger than a critical value $\sigma_c \approx 1$ leading to the onset of global chaos.

3.3.2 Influence of the resistivity on the stochasticity evolution

The background plasma can influence the evolution of magnetic stochasticity. In this section, the influence of resistivity on the stochasticity evolution in a resistive plasma is discussed by presenting the study done by Nardon et al. in Ref. [64]. In the paper, the authors studied the influence of the resistivity on the nonlinear dynamics of a double tearing mode (DTM) in a circular plasma using Eq. 3.9-3.11 in a fixed boundary configuration where $\psi = \psi(t=0), u = \omega = j_\phi = 0$ at the boundary. The authors have used the nonlinear MHD code JOREK, described in chapter 4, for the numerical work.

A DTM is characterized by two resonant surfaces whose interaction leads to faster dynamics than a single tearing mode [66]. Depending on the distance between these resonant surfaces Δx_s and the Lundquist number $S = \tau_R/\tau_A$, where $\tau_R = \mu_0 a^2/\eta$ is the resistive time, the linear evolution of a DTM behave differently as explained in Ref. [75]. In particular, for $S^{1/9}\Delta x_s$ large enough as it is the case studied in [64], the distance between the two resonant surfaces is significant, and a DTM behaves like two localized tearing structures with growth rate scaling as $\eta^{-3/5}$ as predicted by Eq. 3.18. In the nonlinear phase, the two magnetic islands can overlap, generating the so-called global reconnection (or global chaos), causing a loss of the plasma core confinement. The resistivity value strongly influences the dynamics leading to this full reconnection. The resistivity values used in this subsection are normalized with $\eta = \eta_{SI}/\sqrt{\mu_0/\rho_0}$ where $mu_0 = 4\pi 10^{-7}\ Vs/Am$ and $rho_0 = 2n_0 m_{proton}$ with $n_0 = 1e19m^{-3}$ and $m_{proton} = 1.673 \cdot 10^{-27}\ kg$.

The initial q profile used in Ref. [64] is shown in Fig. 3.3 as a function of the radial coordinate expressed as the square root of normalized poloidal flux ψ_n where horizontal lines underline the locations of the resonant surfaces corresponding to the different unstable modes seen through the numerical investigation. In particular, starting from the top, the first line corresponds to the (4,1) mode (DTM), the second to (11,3), and the third to (7,2). The structure of the secondary modes ($(11,3)$ and $(7,2)$) have been found by observing the poloidal cross-section of the $n = 3$ and $n = 2$ (cosine) component of the poloidal magnetic flux ψ.

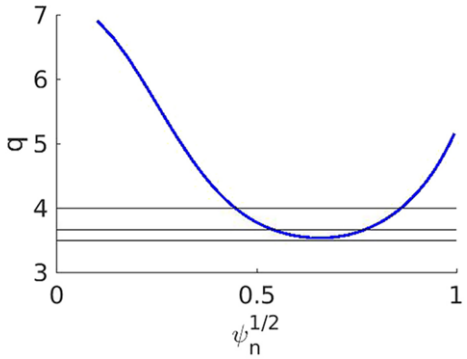


Fig. 3.3 Initial q profile as a function of the radial coordinate (square root of the normalized poloidal flux ψ_N). The horizontal lines correspond, from top to bottom, to q=4, 11/3, and 7/2. Reproduced from [64]

For resistivity values in the interval $[3\times10^{-6}, 5\times10^{-7}]$ Ωm corresponding to 13 eV and 47 eV, a violent MHD relaxation was observed in the simulations due to the overlap of the two $4/1$ magnetic island chains. This violent relaxation causes a significant spike in the plasma current, I_p, as observed in Fig. 3.4. The current spike is not observed for resistivity values outside of the interval.

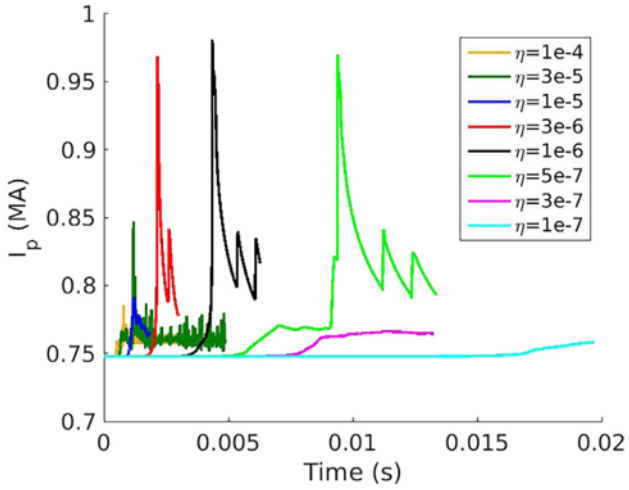


Fig. 3.4 Evolution of I_p for different values of the resistivity. Reproduced from [64]

The reason for this behaviour at different resistivities has been explained by the growth of the magnetic energies of the different toroidal harmonics shown in Fig. 3.5. In the panel, the magnetic energy (E_{mag}) growth of toroidal harmonics $n = 1-5$ for $\eta = 1\times10^{-6}$ (plain curves), $\eta = 3\times10^{-7}$ (dashed curves) and $\eta = 1\times10^{-5}$ (dotted curves) are shown as a function of the rescaled time. The time has been rescaled to overlap the nonlinear phase of the $n = 1$ mode for the different resistivities.

First, the two lower resistivities $(\eta = 1\times10^{-6}, \eta = 3\times10^{-7})$ cases are compared. During the quasi-linear growth of the (4,1) DTM primary mode, the evolution of the different modes is similar. In this phase, secondary modes (with $n > 1$) are generated due to the coupling of the (4,1) mode. In toroidal geometry, a (m,n) mode can couple with itself (like in slab as described in subsection 3.3) or with $(m+1,n)$ and $(m-1,n)$ due to the background magnetic field which depends on (R,Z) coordinates. For instance, the generation of (7,2) is given by the coupling of (4,1) mode with (3,1) mode. Moreover, the linear growth rate of a generic n secondary mode is n-times the growth rate of the (4,1) primary mode.

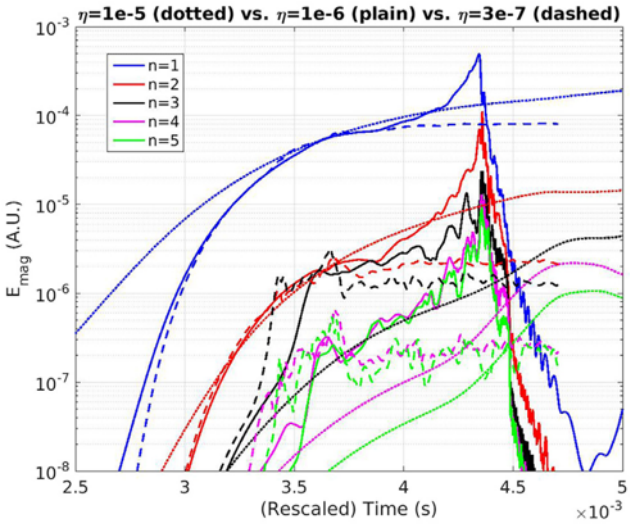


Fig. 3.5 Evolution of the magnetic energy in the toroidal harmonics $n = 1-5$ for $\eta = 1\times10^{-5}$ (dotted curves), $\eta = 1\times10^{-6}$ (plain curves) and $\eta = 3\times10^{-7}$ (dashed curves). Reproduced from [64]

After the quasi-linear phase, ending when $E_{mag,n=1}$ reaches 10^{-6}, the nonlinear phase starts. In the early nonlinear phase, the $n = 1$ and $n = 2$ modes E_{mag} growth curve overlap for the two resistivities. However, the higher-order toroidal harmonics ($n > 2$) show faster and higher growth at lower resistivity. In particular, at $t = 3.40ms$, the E_{mag} of $n = 3$ mode (dashed black curve for $\eta = 3\times10^{-7}$), which has been demonstrated to be an $11/3$ tearing mode in Ref. [64], is significantly higher with respect to $\eta = 1\times10^{-6}$ case (plain black curve). This $11/3$ mode generates magnetic stochasticity at the edge of the 4/1 island in the outer region due to the growth of the n=3 relative to the primary n=1 mode. In particular, the n=1 mode reaches the nonlinear regime earlier than the secondary modes, and its growth scales like η, whereas the growth rate of the secondary modes scales like $\eta^{3/5}$ (still in the linear regime). Therefore, the relative growth of the secondary modes with respect to the primary is $\eta^{-2/5}$, which is more prominent at lower resistivities. In addition, at higher resistivity, the growth rate of a tearing instability is lower than $\eta^{3/5}$, which further lowers the relative growth of the secondary modes with respect to the primary mode in $\eta = 1\times10^{-6}$ case. This reduction is due to the corrections needed for the finite resistivity effects demonstrated in Ref. [70].

The growth of the $11/3$ secondary mode is assumed to affect the distribution of the toroidal current j_ϕ, reducing the drive for the other modes responsible for the

violent relaxation. In particular, comparing the growth rates of the $n = 2$ modes for $\eta = 1 \times 10^{-6}$ and $\eta = 3 \times 10^{-7}$ in the nonlinear phase in Fig. 3.5, it can be observed that after $t = 4ms$ in the higher resistivity case $E_{mag,n=2}$ is characterized by a higher and more robust growth. This mode is associated with a $7/2$ secondary mode, which is assumed to trigger the violent relaxation in the $\eta = 1 \times 10^{-}6$ case. Indeed, in the lower resistivity case, the $n = 2$ is not excited enough due to the early relaxation of j_ϕ caused by the stochasticity generated by the $11/3$ mode growth.

Comparing now the two higher resistivities cases ($\eta = 1 \times 10^{-5}, \eta = 1 \times 10^{-6}$), it can be observed in Fig. 3.5 (dotted curve for the higher resistivity and plain curve for the lower resistivity) that the secondary modes grow much slower in the higher resistivity case with respect to the lower resistivity case. This is in agreement with what has been said above. The absence of solid growth of the secondary modes, particularly the $7/2$ mode, explains the nonoccurrence of global relaxation.

3.4 Mutual interaction between Runaway Electrons and Magnetic reconnection

So far, the treatment of the MHD instabilities has been carried out in collisionless and resistive plasmas without considering the presence of a RE current. In particular, as described in this section, the RE current undergoes a mutual influence with magnetic reconnection and the presence of a RE current alters or adds new features to the evolution of magnetic islands. In addition, the linear growth rate of a tearing mode is no longer lowered by the finite resistivity effects. Therefore, the growth of the secondary modes at large resistivity would scale like $\eta^{3/5}$ as the small resistivity case. As a consequence, the evolution of the stochasticity could be affected as well.

On the other hand, the evolution of a reconnection event can significantly affect the distribution of a RE current. As noted in section 2.3.3, the perturbation of the MHD modes can enhance RE losses, slowing down the avalanche phenomena. At the same time, the evolution of magnetic stochasticity can lead to a benign termination of a fully grown RE beam, as observed during the JET discharge #95135 [59].

In subsection 3.4.1, the mutual influence between RE and magnetic reconnection is described for the single helicity case in slab and cylindrical geometry. In subsection 3.4.2, multiple helicity cases are considered where, among others, the experiment

#95135 and the numerical modeling of the MHD dynamics carried out so far are presented.

3.4.1 Single helicity

A RE current alters the MHD stability of a post-disruption plasma due to its generation mechanisms (more prominent in the hotter region). Indeed, the generation of RE leads to a current profile that is strongly peaked in the core plasma with respect to the predisruption Ohmic current [61]. This distribution of the RE current facilitates the generation of MHD instabilities, which can cause a deconfinement of RE and the bulk resistive plasma [4].

The mutual influence between a RE current and MHD instabilities, such as tearing or kink instability, is generally studied during the RE plateau phase, during which RE carries all the plasma current. The problem was first studied analytically and numerically by Ref. [3] in slab geometry. The study considered the evolution of a tearing instability in the presence of a RE current.

The normalized (on the Alfvèn time and the equilibrium scale) RE current density, j_{RE} evolution is described in Ref. [3] by a fluid equation derived from the drift kinetic equation for the runaway electron distribution function in the zero-gyroradius limit,

$$\frac{1}{\tau_A}\frac{\partial f}{\partial t} + \left(\frac{v_{\|}\mathbf{B}}{\mathbf{B}} + \frac{\mathbf{E}\times\mathbf{B}}{B^2}\right)\cdot\nabla f = 0 \tag{3.24}$$

where $v_{\|}$ is the particle parallel velocity to the magnetic field and the second term in the parenthesis is the $E \times B$ drift. Assuming the RE to travel at the speed of light, the drift kinetic equation can be integrated over the velocity space to get the equation for j_{RE},

$$\frac{\partial j_{RE}}{\partial t} + [\varphi, j_{RE}] + \frac{c}{v_A}([\psi, j_{RE}] - \frac{\partial j_{RE}}{\partial z}) = 0 \tag{3.25}$$

Where the third term expresses the advection of the RE with the speed of light normalized with respect to the Alfvèn velocity. Eq. 3.25 is coupled with the two fluid RMHD equation through the current coupling scheme, which consists of subtracting the RE current density from the total current density in the resistive term of the generalized Ohm's law 3.12. This is because the resistive contribution comes only

from the thermal electrons, and the RE are assumed to be collisionless. Therefore, the Eq. 3.12 becomes,

$$\frac{\partial F}{\partial t} + [\varphi, F] - \rho_s^2 [U, \psi] + \eta (j - j_{RE}) + \frac{\partial \varphi}{\partial z} + \rho_s^2 \frac{\partial U}{\partial z} = 0 \tag{3.26}$$

In order to have the three equations of interest in one place, the system of equations is written here for a slab geometry,

$$\frac{\partial F}{\partial t} + [\varphi, F] - \rho_s^2 [U, \psi] + \eta (j - j_{RE}) + \frac{\partial \varphi}{\partial z} + \rho_s^2 \frac{\partial U}{\partial z} = 0 \tag{3.27}$$

$$\frac{\partial U}{\partial t} + [\varphi, U] - [j, \psi] - \frac{\partial j}{\partial z} = 0 \tag{3.28}$$

$$\frac{\partial j_{RE}}{\partial t} + [\varphi, j_{RE}] + \frac{c}{v_A} ([\psi, j_{RE}] - \frac{\partial j_{RE}}{\partial z}) = 0 \tag{3.29}$$

$$F = \psi + d_e^2 j = \psi - d_e^2 \nabla^2{}_\perp \psi, U = \nabla^2{}_\perp \varphi \tag{3.30}$$

Where $x = (R - R_0)/a$, $y = Z/a$, $z = -\zeta$, and (R, ζ, Z) are cylindrical coordinates defined relative to the torus symmetry axis. In Ref. [3], the solution of the Eq. 3.27-3.30 is derived by linearizing the equations and assuming an initial equilibrium with normalized flux $\psi = \psi_0(r)$, stream function $\varphi_0 = 0$, equilibrium total and RE current density $j_0(r) = j_{RE,0}(r) = -\nabla_\perp^2 \psi_0$ with $r^2 = x^2 + y^2$. Therefore, the normalized poloidal equilibrium field is equal to $-\psi_0'(r)$, and the safety factor is $q(r) = -r/\psi_0'(r)$ (with $B_z = 1$ and $R = 1$). Moreover, the contribution of the electron skin depth and the ion sound Larmour radius are neglected. The linearized equations become,

$$\gamma \psi + i k_\parallel' x \varphi = \eta (\psi'' + j_{RE}) \tag{3.31}$$

$$\gamma \phi'' + i k_\parallel' x \psi'' = -i k_\parallel' J_0' \psi \tag{3.32}$$

$$(k_\parallel' x + i \gamma v_A / c) j_{RE} = k_\parallel' J_{RE,0}' (\psi + v_A \varphi / c) \tag{3.33}$$

The Eq. 3.31-3.33 are valid for the resistive layer where $x = r - r_s \approx w \ll 1$ and with the approximation $k_\parallel = n - m/q(r) = k_\parallel' x$. From Eq. 3.33, an expression for the perturbed RE current can be derived in the inner layer [3],

$$j_{RE} = \frac{mJ'_{RE,0}}{k_{\|} r_s} \frac{\psi + v_A \varphi / c}{x + i\gamma v_A / k'_{\|} c} \approx \frac{mJ'_{RE,0} \psi}{k_{\|} r_s x} \tag{3.34}$$

where $J'_{RE,0}$ is the derivative of the equilibrium runaway current density at the rational surface. In Eq. 3.34 the approximations $\gamma v_A / c \ll w$ and $v_A \varphi / c \ll \psi$ have been made. As a consequence, the runaway current density is infinite at $x = 0$. Therefore, $J'_{RE,0} = 0$.

It has been analytically demonstrated in [3] that RE does not influence the linear evolution of a tearing instability. However, RE does not require the higher-order corrections needed to estimate the linear growth in the case of finite resistivity. Indeed, as shown in Fig. 3.6, in the presence of RE, the numerical linear growth rates (star marker) of the tearing instability agree with those predicted by Eq. 3.18 (plain curve). Whereas, without RE, the numerical linear growth rates (square marker) of the tearing instability agree with those predicted by Eq. 3.19 (dashed curve), which accounts for the higher order corrections.

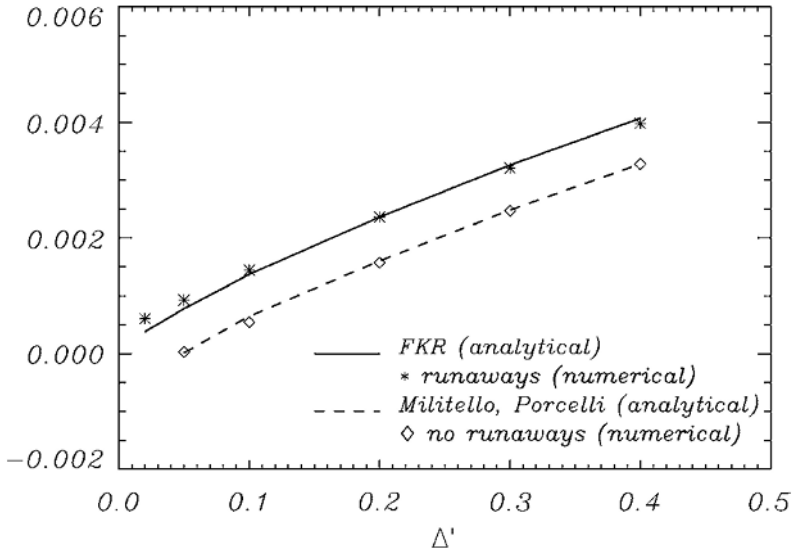


Fig. 3.6 Comparison between the analytically and numerically derived linear growth rates of the tearing instabilities with (plain curve and stars) and without (dashed curve and squares) [3]

The nonlinear evolution of the magnetic island is analytically studied in Ref. [3] by assuming that $j_0(x)$ has a maximum at the resonant surface location, $x = 0$. It has been shown that the presence of RE leads to an amplitude of the magnetic island at

saturation, which differs from the case without RE. In particular, the RE distribution is characterized by a different profile with respect to the ohmic current which leads to a different saturation mechanism for the magnetic island with RE than without RE.

The different widths have been derived analytically in Ref. [3]. In particular, in the presence of RE,

$$w = -\frac{1}{b}\frac{\Delta'}{0.272} \tag{3.35}$$

whereas in the absence of RE,

$$w = -\frac{1}{b}\frac{\Delta'}{0.411} \tag{3.36}$$

According to Eq. 3.35, the island's width at saturation with RE is around 50% higher than the case without RE. This has been also confirmed numerically, however, at high Δ' a bifurcation was found in the simulations around $\Delta' \approx 0.44$. As explained in [3], this was due to the periodic equilibrium assumed for the simulations causing the formation of magnetic islands at the boundary, which interact with the central island in case of a high Δ' leading to larger island widths during the nonlinear phase.

If the assumption of a symmetric current profile with respect to the resonance surface, considered in Ref. [3], is rested, new features related to the growth of tearing instability with RE are found. In Ref. [4], the evolution of a tearing instability with asymmetric RE current profile has been considered in cylindrical geometry based on the equations of Ref. [3]. It has been found that the presence of RE causes the mode to have a real frequency, causing a rotation of the tearing mode. This is because $J'_{RE,0} \neq 0$ and a finite value of v_A/c leads to an imaginary correction to j_{RE} for $x \to 0$. This correction is valid in the sublayer on which the RE current is distributed and is defined as,

$$\delta_2 = \gamma v_A/(k_c c) \tag{3.37}$$

where $k_c = nq'/(Rq)$. Moreover, $|\delta_2| \ll |\delta_1|$ with δ_1 defined as Eq. 3.20. Due to this correction, the dispersion relation for the growth of the tearing instability is characterized by the presence of an imaginary term [4],

$$\frac{\gamma^{5/4}}{\eta^{3/4}k_c^{1/2}}\frac{2\pi\Gamma(3/4)}{\Gamma(1/4)} = \Delta' - i\pi\frac{mJ'_{RE,0}}{|k_c|r_s} \tag{3.38}$$

where $\Gamma(3/4)$ and $\Gamma(1/4)$ are numerical coefficients. Having $J'_{RE,0} \neq 0$ adds an imaginary term to the dispersion relation responsible for the tearing mode real frequency. Indeed, the assumption of a symmetric current profile in slab geometry with a maximum at x=0 leads to $J'_{RE,0} = 0$. In Ref. [4], the numerical results agree with what is predicted by Eq. 3.38, however, the study is limited only to the linear regime. In addition, due to the width of the microlayer δ_2, it is pointed out that effects characterized by small scales, such as the electron inertia, may become necessary in this configuration.

In chapter 5, the study by Ref. [4] was extended to the nonlinear regime in a slab geometry, and the electron inertia's influence on the instability evolution was analyzed. This was done after reproducing the results shown in Ref. [3] and extending them to values of $\Delta' \approx 1$

3.4.2 Multiple helicity

The presence of multiple magnetic islands can lead to the stochastization of the magnetic field as described in section 3.3. In the presence of RE, the magnetic chaos can lead to the radial diffusion of the RE population. Indeed, as described in section 2.3.3, RMP and REMC coils aim to perturb specific modes in the plasma to trigger the stochastic process. However, in large Tokamaks such as ITER, the perturbations induced by these coils cannot reach the plasma core where RE generation occurs. Therefore, alternative strategies are needed to mitigate RE.

One of the strategies being investigated is the benign termination of RE [59, 5, 76]. In a benign termination, a RE population is lost at the wall with a large wetted area without damaging it. This strategy exploits large MHD instabilities arising after an SPI injection by interacting with multiple magnetic islands characterized by different helicities. The experimental evidence of a benign termination has been observed in the JET discharge number 95135 [59]. The dynamics of this discharge leading to the final crash of RE is described in section 3.5. Here, the interaction between the RE and the plasma MHD activity responsible for the final crash is described. This work has been done in Ref. [5], which is taken as a reference for this subsection.

The interaction of RE with the plasma MHD activity is investigated through JOREK with Eq. 3.9-3.11, which are coupled with a RE fluid equation via the current coupling scheme as done with the equations in slab geometry. The system of equations is,

$$\frac{\partial \psi}{\partial t} = \eta \left(j - c n_{re} \frac{F_0}{BR} \right) - F_0 \frac{\partial \varphi}{\partial \phi} + R[\varphi, \psi] \tag{3.39}$$

$$\nabla \cdot \left[\rho R^2 \nabla_{pol} \frac{\partial \varphi}{\partial t} \right] = \frac{1}{R} \left[R^4 \rho U, \varphi \right] - \frac{1}{2R} \left[R^2 \rho, R^2 |\nabla_{pol} \varphi|^2 \right] + \frac{1}{R} [\psi, j] - \frac{F_0}{R^2} \frac{\partial j}{\partial \phi} + \mu \nabla^2 U \tag{3.40}$$

$$\begin{aligned} \frac{\partial n_{re}}{\partial t} = (i_D - 1) \left[\frac{-c}{BR} \left([n_{re}, \psi] + \frac{F_0}{R} \frac{\partial n_{re}}{\partial \phi} \right) \right] + R[n_{re}, u] \\ + \nabla \left(i_D D_{re,\parallel} \nabla_{\parallel} n_{re} + D_{re,\perp} \nabla_{\perp} n_{re} \right) \end{aligned} \tag{3.41}$$

$$j = R^2 \nabla \cdot \left(\frac{1}{R^2} \nabla_{pol} \psi \right), U = \nabla \cdot \nabla_{pol} \varphi \tag{3.42}$$

with $j = j_{th} + j_{RE}$ and $j_{RE} = -ecn_r \hat{b}$ where $\hat{b}$ is the unit vector along the magnetic field. With respect to Eq. 3.10, in Eq. 3.40, the term related to viscosity μ is also considered to remove small-scale fluctuations. Moreover, differently from the RE fluid equation in slab geometry where only the advection of RE is considered, Eq. 3.41 contains also the parallel diffusion,$D_{re,\parallel}$, and perpendicular diffusion,$D_{re,\perp}$ of RE. The model allows to switch between the parallel advection and the diffusion of RE through the boolean value i_D. In the work carried out in [5], only the diffusion of RE is considered since simulations with advection are more computationally demanding. At the same time, it is also mentioned that using parallel diffusion with transport timescale equivalent to advection gives similar results without losing meaningful physical effects.

The numerical investigation of the RE crash is started using the computational domain shown in the left panel of Fig. 3.7, where the initial distribution of the normalized RE density (color) can also be observed with the domain's boundary approximating the first wall surface. This distribution of the RE density corresponds to a hollow RE current profile (purple) as depicted in the right panel of Fig. 3.7. This profile has been selected by performing forward synchrotron pattern modeling using SOFT, which consisted of matching the real synchrotron diagnostic image with the

one obtained through SOFT by using different RE current profiles. This profile was further adjusted by observing the position of the various magnetic islands in the synchrotron image to get a realistic profile for the safety factor (dashed green curve). Further details about the derivation of the starting profiles can be found in Ref. [5]

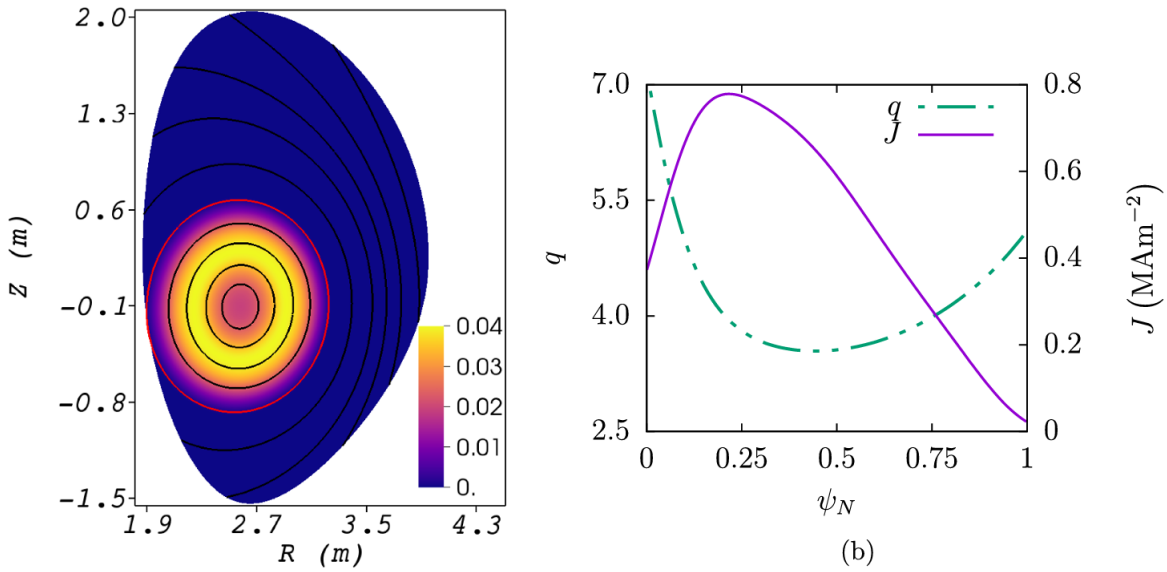


Fig. 3.7 a) Simulation computational domain colored with the normalized RE density distribution and the flux surfaces. b) Initial RE current (purple curve) and safety factor profiles (dashed green curve) as a function of the normalized poloidal flux ψ_N. Reproduced from [5]

The simulation input parameters are summarized in Tab. 3.1 where B_0 is the on-axis toroidal magnetic field, η corresponds to a Spitzer resistivity ($\eta_{\parallel} = 1.65e-9 \ln\Lambda(T_e[keV])^{-3/2}$) at $T = 10\,eV$ and n are the toroidal mode numbers (or harmonics) considered for the simulation.

I_p	0.747 MA
B_0	3.49 T
n_e	1e19 m^{-3}
η	3.3 e-5 Ωm
μ	1.6e-6 $kgm^{-1}s^{-1}$
$D_{r,\parallel}$	1e10 m^2s^{-1}
n	0,...,8

Table 3.1 Simulation input parameters

The magnetic energy growth of the different modes is shown in Fig. 3.8. As in the case without RE seen in section 3.3, the quasi-linear phase is characterized by a primary mode $n = 1$ whose nonlinear coupling with itself and the other modes gives rise to the other toroidal modes. After $t = 0.97$ *ms* the modes growth enters the nonlinear regime where the interaction between the modes causes the magnetic field stochastization.

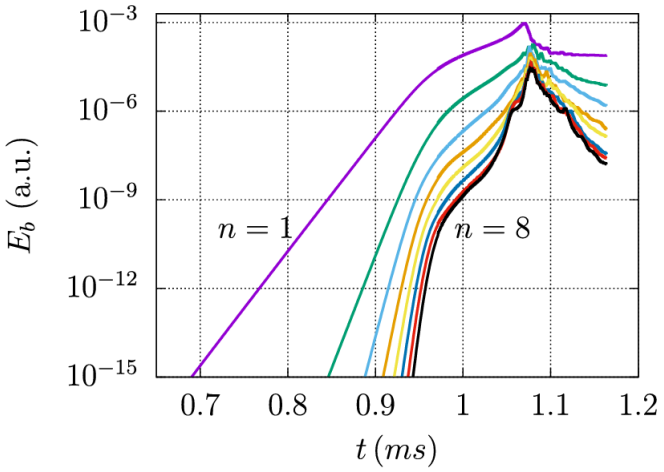


Fig. 3.8 Magnetic energy growth of the toroidal harmonics as a function of time [5]

The evolution of magnetic stochasticity and its effects on the RE population in density and current amplitude is depicted in Fig. 3.9, where the Poincaré plots are shown with the background plasma colored with the RE density. At $t = 0\ \mu s$ (frame a), the magnetic field is characterized by the presence of magnetic islands. In particular, at the position where $q = 5$, there is one (5,1) magnetic island chain and two (4,1) magnetic island chains where $q = 4$. The stochastization occurs due to the interaction between two island chains (4,1) and (5,1) at the edge ($t = 31\ \mu s$, frame b). At $t = 81\ \mu s$ (frame c), the stochasticity reaches the inner (4,1) island chain. Afterward, the shrinkage of the core occurs due to the interaction of higher poloidal mode numbers, and the remnant flux surfaces in the core are destroyed (frames d and e). At last, the reformation of flux surfaces occurs ($t = 194\ \mu s$, frame f).

The evolution of the stochasticity is accompanied by the loss of the RE current, as noted by the amplitude of the RE current in different frames of Fig. 3.9. Almost the entire population of RE is lost in $100\mu s$ starting from $t = 31\mu s$ until $t = 122\mu s$. This is due to the radial diffusion of the magnetic field lines transporting RE to the wall. At the same time, as can be noticed in frame c, the RE loss is faster in the

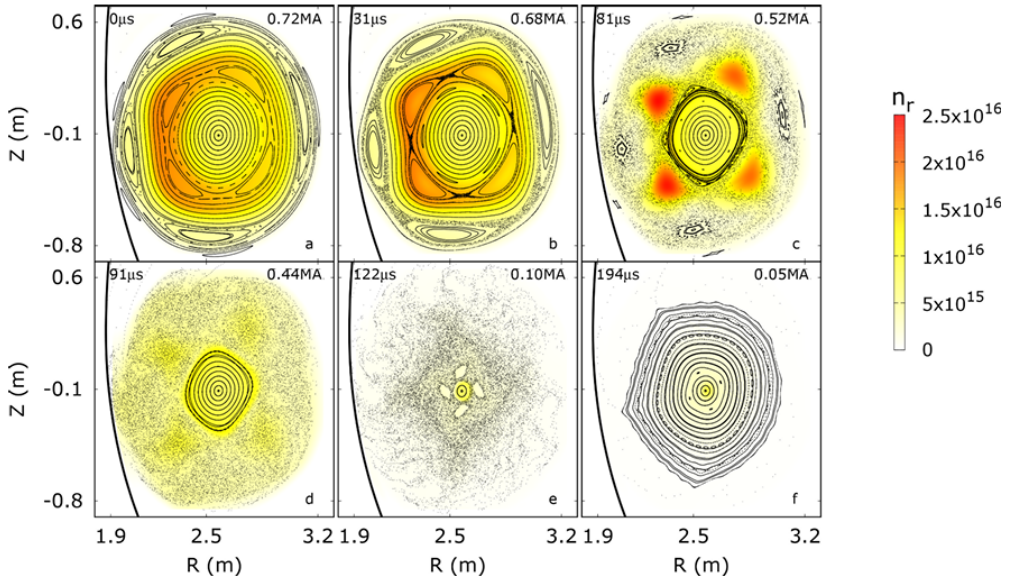


Fig. 3.9 Poincaré plots showing the evolution of the magnetic field stochastization at different time points, starting from $t = 0.97ms$ corresponding to $t = 0\mu s$ in panel a), b) $t = 31\ \mu s$, c) $t = 81\ \mu s$, d) $t = 91\ \mu s$, e) $t = 122\ \mu s$, $t = 194\ \mu s$. The background plasma color indicates the RE density, whereas in the top right corner of each panel, the RE current amplitude is noted at different times. Reproduced from [5]

stochastic regions than from within the island regions (high localized RE density in the islands). This was also observed in Fig. 2.8, where the RE undergoes higher loss times in the presence of magnetic islands.

In magnetic topologies characterized by stochastic regions and island regions, the RE population located within the island regions can be trapped in them, leading to a much higher confinement time than in the stochastic region [32]. That is, the magnetic islands act as barriers to transport RE to the wall [77]. As shown in Ref. [32], in fully enclosed stochastic regions, the RE radial transport is governed by Rechester-Rosenbulth (RR) diffusion coefficient, $D_{RR} = \pi q v_{\|} R(\delta B/B)^2$ where $v_{\|}$ is the RE parallel velocity $v_{\|} \approx c$. However, in the case of mixed topologies, the radial diffusion is lower than what is predicted by D_{RR}. At the same time, in an open chaotic system (where the field lines touch the wall), D_{RR} is not valid anymore because the region of enhanced transport region extends up to the wall, leading to a higher loss of RE. Consequently, different models have been proposed in the literature to compute the diffusion coefficient in such topologies [32], [77].

In Ref. [32], a position-dependent exponential particle loss has been proposed for the RE loss to account for the presence of magnetic islands. That is, $N_{lost} \propto 1-\exp -t/\tau(\psi)$ where $\tau(\psi)$ is the characteristic time loss depending on the particle initial position evaluated as $\tau(\psi) \propto \exp -\psi/\psi_0$ where $\psi_0 \propto \delta B/B$. To accurately predict the fraction of the lost RE, the RE density has been expressed as $n(\psi,t) = n_c(\psi) + n_{nc}(\psi,t)$ where the exponential formulation is used to estimate the non confined RE density $n_{nc}(\psi,t)$ whereas the confined RE density $n_c(\psi)$ is given by a numerical simulation carried with the ANTS code [32].

The results of the RE loss evolution given by the ANTS simulation have been found to agree with the exponential loss model rather than the diffusive model for the magnetic configuration provided in the frame a) of Fig. 3.10 (similar to the panel a) in Fig. 2.8). In the presence of remnant of the magnetic island chains corresponding to the positions $\psi = 0.5, \psi = 0.6$ and $\psi = 0.7$, a higher RE confinement time can be observed in panel b) of Fig. 3.10. The figure was obtained through a numerical simulation using the ANTS code. The RR diffusion model cannot capture this modified transport due to magnetic islands, as seen in panel c). In contrast, the exponential loss model results agree with the numerical simulation (panel d)).

During the RE loss observed in Fig. 3.9, the flattening of the total current occurs due to fast magnetic reconnection. This can be observed in the left frame of Fig. 3.11, showing the total current density profile with the corresponding safety factor profile in the right frame. Until $t = 116\,\mu s$ so, during the stochastization of the magnetic field, a minor-radially inward shift of the current profile or the position of high shear in the q profile occurs. This leads to the evolution of instability with high poloidal mode numbers, causing the core shrinkage observed in Fig. 3.9. When the current and q profile become flat, the magnetic flux surfaces reformation occurs.

The RE loss to the wall occurring during the stochastization does not cause any damage to the wall. Indeed, stochasticity starting at the edge leads to a poloidal broadening of the deposition at the wall with respect to a core-stochastization, which would lead to a deposition concentrated near the point of contact between the plasma and the limiter. The poloidal broadening of the deposition can be observed in panel a) of Fig. 3.12 showing the RE flux ($1/m^2$ per unit time) distribution as a function ψ_N and distance from the point where the plasma touches the wall corresponding to $\psi_N = 1$. As shown in panel a), the deposition is spread until $\psi_N = 1.2$ corresponds to a distance from the contact point of 50 cm, which is considered a poloidal broadening

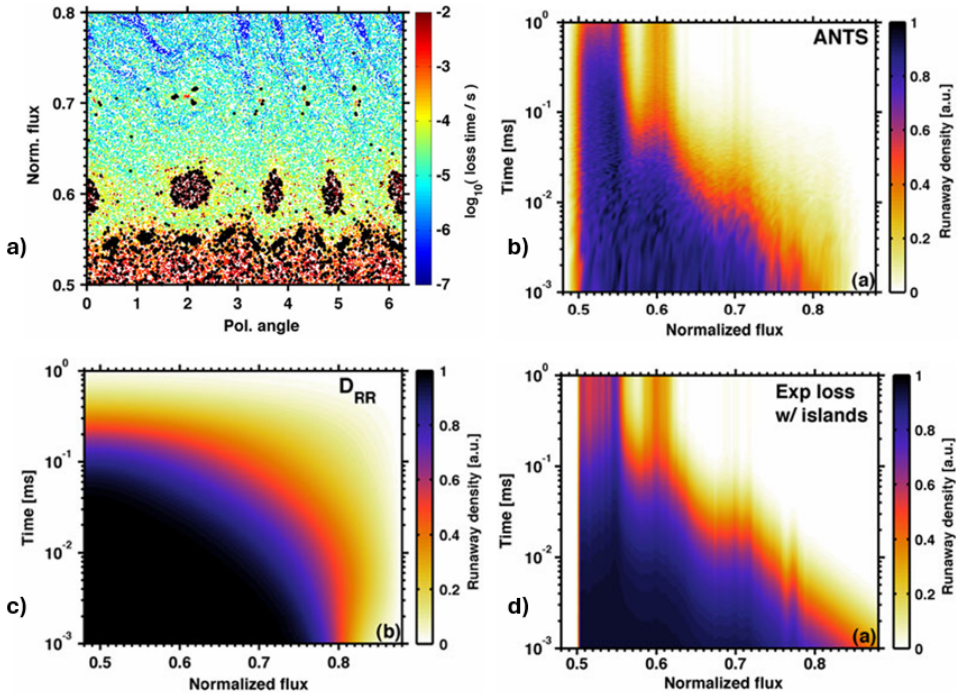


Fig. 3.10 a) RE loss time in logarithmic scale as a function of starting position (ψ, θ) where $\theta = atan^2(Z,R)$ in radiants. b) Evolution of the RE density as a function of the normalized flux and time computed through ANTS code. c) Evolution of the RE density as a function of the normalized flux and time computed through the Rechester–Rosenbluth diffusion model. d) Evolution of the RE density as a function of the normalized flux and time computed through exponential loss model. Reproduced from [32]

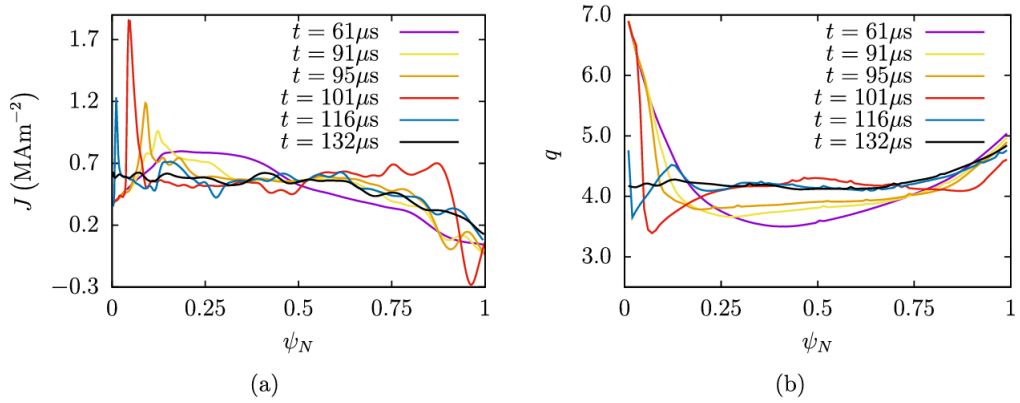


Fig. 3.11 a) Current density profiles and b) Safety factor profiles at different time points with $t = 0\mu s$ corresponding to $t = 0.97ms$. Reproduced from [5]

of the RE deposition. Moreover, most RE deposition occurs in approximately 20 μs, which aligns with the experiment.

On the other hand, by observing the RE fluence in panel b) of Fig. 3.12 plotted as a function of ψ_N, toroidal angle ϕ and distance from the limiter point, it can be noticed that the toroidal distribution does not present any localized hot-spot. This is attributed to the dominance of the $n = 1$ mode in all simulation phases.

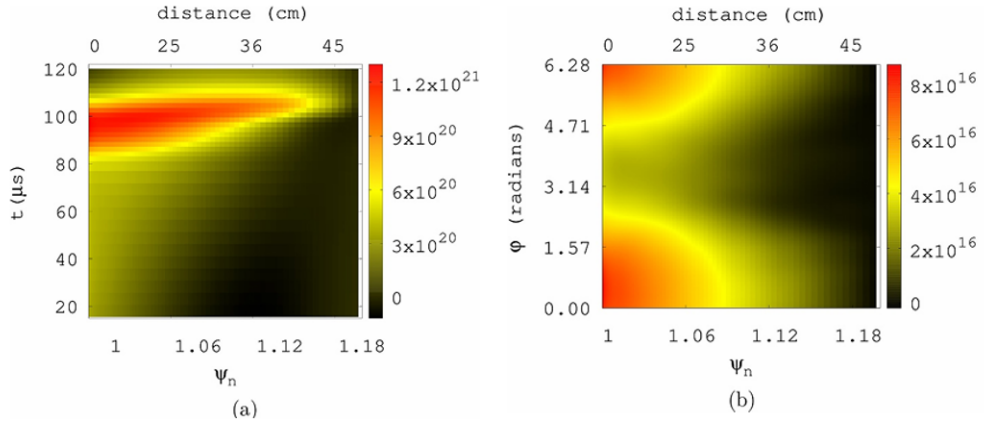


Fig. 3.12 a) RE flux (particles per square meter per unit time) distribution as a function of ψ_N or distance from the limiter point b) RE fluence $(1/m^2)$ distribution as a function of ψ_N and toroidal angle ϕ (shown as φ in the figure) during the time interval shown in panel a), reproduced from [5]

The numerical work in Ref. [5] assumed a specific value for background plasma resistivity and ion density and used the RE diffusion instead of advection. As seen in subsection 3.3, the resistivity significantly influences the evolution of the magnetic stochasticity. Therefore, a scan of resistivity and ion density was performed in this PhD to analyze their impact on the system evolution assuming purely advective RE. The results of this work are presented in section 6.

3.5 RE termination dynamics during JET pulse 95135

The MHD modeling of the JET discharge #95135 described in subsection 3.4.2 has clearly shown the role of the magnetic field stochastization behind the harmless RE impact onto the wall. This was possible thanks to a particular experimental setup presented and analyzed in Ref. [59, 76]. Here, a brief description of this experiment and the postprocessing done for the MHD modeling is given to show the implications of several theoretical concepts introduced in chapters 2 and 3.

Fig. 3.13 compares the RE termination dynamics from the TQ of three different JET discharges where disruption is triggered through Ar MGI [59]. The blue curves represent the evolution of a standard disruption without any second injection. In this case, the background plasma contains mainly Ar injected through the MGI system coexisting with the RE beam, whose impact at the wall leads to high heat fluxes, increasing with the RE current's amplitude (panel e, blue squares). The injection of high Z impurity such as Ne or Ar (red curves) in the RE beam at the instant depicted by the vertical line in Fig. 3.13 causes a faster decay of the RE current with respect to the case with no second injection as shown in panel a). However, this fast decay is characterized by significant heat loads on the wall, as seen in panel e) (red triangles).

A second deuterium injection leads to entirely different dynamics (green curves in Fig. 3.13). Indeed, the RE current increases (panel a) differently from the other discharges. This is caused by a series of events after the D_2 injection, starting with a flush out of the Ar. The reason for this expulsion has been studied in Ref. [78], where the second injection of D_2 is studied to terminate RE beams in DIII-D Tokamak. In particular, the study shows that the injection of D_2 neutrals causes an additional cooling of the background plasma, leading to the recombination of Argon ions. The recombined Ar is characterized by higher rates of outward radial transport with respect to the ions causing the removal of Ar from the core plasma [78]. The recombination event is also highlighted by the drop of free electrons population (panel b) and by the decrease of the Ar line radiation accompanied by the appearance of D_2 line radiation in the radiated power [76].

The expulsion of Ar causes a decrease in the plasma's effective resistivity, leading to an increase in the plasma current amplitude. When the plasma current reaches $I_p = 0.76\,MA$ after 220 ms of pellet arrival, a significant neutron spike is observed (panel c) due to the RE loss to the wall without any heat loads measured by the Infrared (IR) camera (panel e). At the same time, a large magnetic perturbation is measured during the RE collapse [76].

The benign termination of RE in JET pulse #95135 is found to be a consequence of two mechanisms observed in the discharge, which are a significant MHD instability causing the plasma stochastization and the absence of RE regeneration during the CQ due to the previous expulsion of Ar.

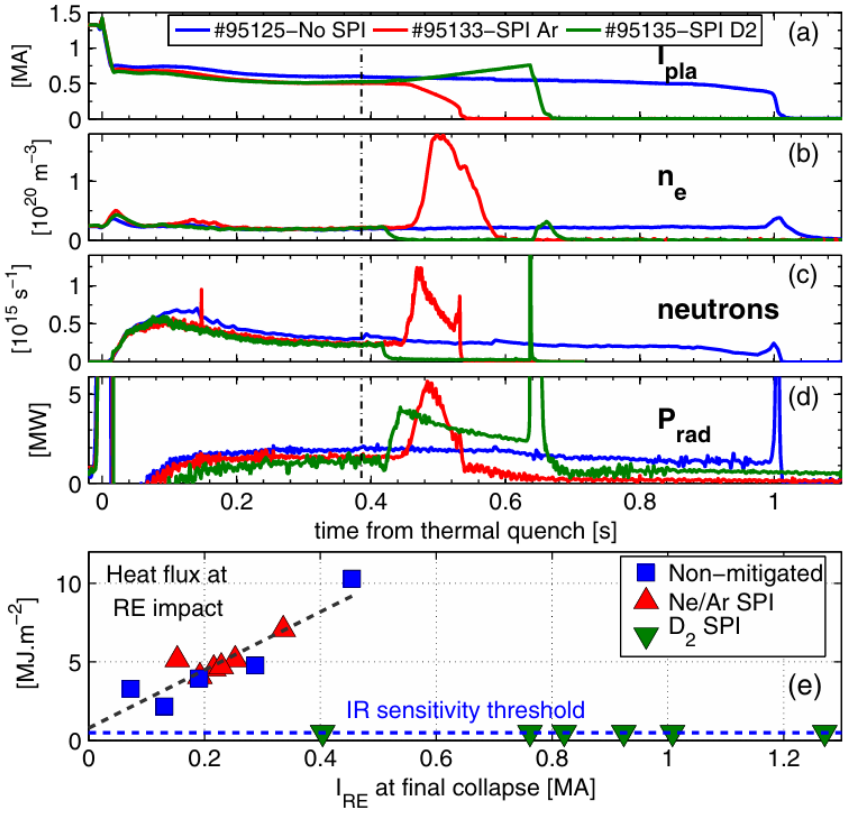


Fig. 3.13 Comparison between three RE termination scenarios with no second injection (blue curves), high Z impurity second injection (red curves), and low Z impurity second injection (green curves). Evolution of the a) total current, b) average electron density, c) total neutron rate, and d) total radiated power from the thermal quench. e) Wall heat flux as a function of impacting RE current. Dashed vertical line indicates the D_2 SPI injection. Reproduced from [76]

3.5.1 Plasma stochastization

A decrease of the edge safety factor q_{edge} occurs due to the increase in the plasma current, and the MHD instability responsible for the RE collapse is triggered when $2 < q_{edge} < 5$ [76]. This large interval of q_{edge} is thought to give origin to an MHD instability, and through numerical investigation in Ref. [25] described in subsection 3.4.2, it has been demonstrated that the evolution of a DTM triggers the plasma stochasticity. The RE current profile responsible for the evolution of a DTM seen in [5] has been reconstructed by comparing the experimental synchrotron image and the one obtained through SOFT simulations [76]. In Fig. 3.14, the best match of this reconstruction is shown and obtained, assuming a spatially uniform RE energy and

pitch angle distribution. The best match has been given by a pitch angle between $(0.1-0.3)$, a RE energy less than 15 MeV, and a hollow RE current density profile (represented in panel b) of Fig. 3.7).

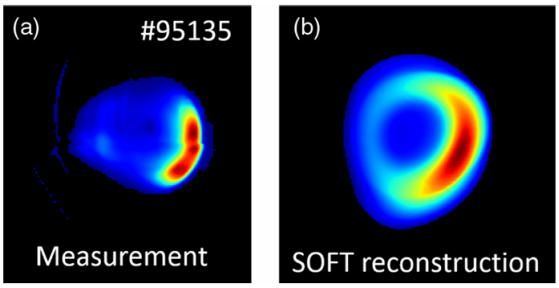


Fig. 3.14 Comparison between the (a) measured infrared synchrotron radiation image and (b) SOFT reconstructed synchrotron image. Reproduced from [76]

The IR synchrotron radiation images also allowed to determine the position of the different magnetic island chains before the RE collapse. The radial locations of $m = 4$,$m = 5$, and $m = 6$ magnetic islands are shown in Fig. 3.15 starting from $t_{ref} = 48.0233\ s$. The $m = 6$ structures (star symbol) move radially outwards and leave the plasma after 50 ms. The same happens with the m=5 structures (square symbol). However, these remain inside the last closed magnetic flux surface even if they become invisible after 47.58 s. The $m = 4$ islands, instead, appear just before the crash, highlighted by the red dashed line. The equilibrium profiles for the current and safety factor utilized in [25] are taken at $t = 0.63$ ms (green dashed line) some instants before the final crash.

The islands shown in Fig. 3.15 are all characterized by the toroidal mode $n = 1$. This has been observed to be the most probable mode of the magnetic perturbation through the Mirnov coil and is consistent with a $q = 4$ instability [76]. Therefore, the plasma stochastization is given by the interaction of the modes with $n = 1$, and its evolution is described in subsection 3.4.2.

Through the measurement of the experimentally observed instability growth rate, dB_{pol}/dt, in the three scenarios shown in Fig. 3.13, it has been found that the growth rate is more significant in the case with D_2 second injection. However, even if a considerable growth rate of the perturbation resulted in a significant RE loss, this is not the only ingredient behind the harmless RE impact on the wall [76]. Indeed, the absence of RE regeneration played a crucial role as well.

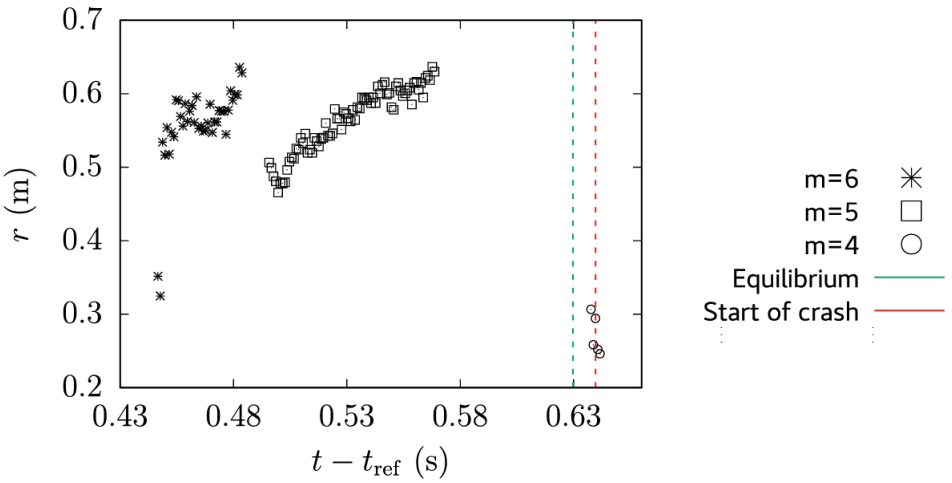


Fig. 3.15 Evolution of the minor radial location of $m = 4$, $m = 5$ and $m = 6$ magnetic island chains derived from the IR synchrotron images starting from $t_{ref} = 48.0233$ *s* taken as reference, reproduced from [25]

3.5.2 RE regeneration

The RE loss reduces the plasma current since RE are the main carriers of the plasma current during the RE current plateau phase. This reduction of the plasma current causes an increase in the electric field, which can, in certain conditions, lead to the generation of additional RE. Apart from that, this electric field can also induce a thermal current into the bulk plasma. Moreover, the generation of RE translates into the conversion of plasma magnetic energy, W_{mag}, into kinetic energy, E_{kin}, which the RE would deposit on the wall during the impact [79].

In JET discharge #95135, a thermal current is generated through the induction effect [25]. Therefore, the thermal electrons carry the plasma current and undergo the CQ phase (blue curve), as shown in Fig. 3.16. Moreover, the green curve shows that Ohmic reheating of the plasma occurs, leading to plasma reionization and a spike in the radiated power. At this stage, the radiated power is dominated by the line radiation from the weakly ionized Ar, indicating that a small fraction of Ar still survives in the core plasma.

However, the presence of a small amount of high-Z impurities in the core plasma does not lead to the generation of additional RE during the CQ following the RE loss. This is because, in the case of low high-Z impurity, the ohmic reheating of the cold plasma is not hindered by the RE Dreicer and avalanche generation mechanism,

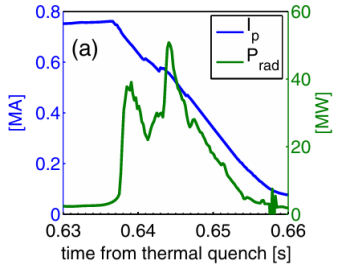


Fig. 3.16 Evolution of the total current and radiated power, reproduced from [76]

as demonstrated in Ref. [76]. These mechanisms dominate in the presence of a considerable amount of high Z impurities and lead to RE regeneration during CQ, as in cases with high Z-impurity second or no second injection. In addition, since RE regeneration is accompanied by the conversion of magnetic energy into kinetic energy deposited on the wall, in the case of low, high Z-impurity, this conversion is weak. Finally, the combination of magnetic stochastization with the following RE loss and absence of RE regeneration due to a weak conversion of W_{mag} into W_{kin} due to low high-Z impurity leads to a benign termination of RE.

Chapter 4

Numerical Tools

This section describes the numerical tools utilized for the studies conducted during the PhD. For studying the mutual interaction between a RE current and magnetic reconnection in a post-disruption plasma in a 2D slab geometry, a non-linear two-fluid RMHD code called SCOPE3D (Solver for COllissionless Plasma Equations in 3D geometry) was utilized and is described in section 4.1 [6]. Meanwhile, for modelling the RE benign termination in JET #95135, a nonlinear MHD code called JOREK [80] was used and it is introduced in section 4.2.

The interaction of a RE beam with the FW material was analyzed through a Monte Carlo code called FLUKA [81] and a finite element code-named FREEFEM++ [82] described in section 4.3 and 4.4, respectively.

4.1 SCOPE3D

SCOPE3D is a code used for the solution of the two fluid RMHD equations (Eq. 3.27-3.30) [6] in a 2D and 3D slab geometries. It has been mainly applied to studying magnetic reconnection in collisionless plasma in 3D slab geometry. However, in recent years, it was utilized to investigate the stability of a post-disruption plasma in the presence of a RE current. In this case, the code was mainly used in the 2D configuration since the aim was to study the interaction of an RE current with a single magnetic island.

SCOPE3D adopts an explicit third-order Adams-Bashforth time scheme, which gives an approximation of an ordinary differential equation $d\psi/dt = F(\psi)$ in the form,

$$\phi^{n+1} - \phi^n = \frac{\Delta t}{12}\left[23F(\phi^n) - 16F(\phi^{n-1}) + 5F(\phi^{n-2})\right] \tag{4.1}$$

where ϕ^n is the numerical approximation to $\psi(n\Delta t)$.

The code is parallelized along the periodic directions y and z along which Fast Fourier methods (FFT) are applied to approximate the spatial derivatives. Therefore, each processor applies the FFT to its respective y-slice of the global matrix if a 2D problem is considered. This is done through a transposition of the local matrix since the FFT requires access to all the domain points, and each processor contains only a few points in y and all the points in x.

The Fast Fourier method for computing derivatives of periodic functions involves transforming a function from the spatial domain to the frequency domain, differentiating it in the frequency domain (where differentiation becomes multiplication by a constant), and then transforming it back to the spatial domain.

In contrast, a compact finite difference scheme is utilized on a non-equispaced grid in the direction of the magnetic field shear, x. Adopting a non-equispaced grid allows for a higher spatial resolution in the reconnection region with respect to the remaining domain and, thus, saves computation time. The compact finite difference scheme implemented in SCOPE3D is based on the derivations presented in Ref. [83] for an equispaced grid, and the first order derivative is approximated as,

$$\alpha f'_{i-1} + f'_i + \alpha f'_{i+1} = \frac{a f_{i-1} + b f_i + c f_{i+1}}{h_i} \tag{4.2}$$

Where the coefficients α, a,b, and c are derived by matching the Taylor series coefficients of various order up to the third derivative. h_i is the grid spacing between x_i and x_{i+1} and h_{i-1} is the grid spacing between x_i and x_{i-1}. Since a fourth-order tridiagonal scheme is adopted in SCOPE3D to have a fourth-order accuracy, the additional constraint necessary to derive all five coefficients is given by $a+4b+9c = 6\alpha$.

The study done with SCOPE3D uses non-periodic boundary conditions. Therefore, a different formulation is adopted at the first and last node of the grid for the first derivative approximation [83]. For instance, for the first node $i = 1$, this is,

$$f_1' + \alpha(1) f_2' = \frac{1}{h_1}(a f_1 + b f_2 + c f_3 + d f_4) \tag{4.3}$$

The values of the coefficients in Eq. 4.3 are selected based on the order of accuracy needed. In particular, for second-order accuracy $\alpha = 0$,$a = -3/2$, $b = 2$, and $c = -1/2$ whereas for fourth-order accuracy $\alpha = 3$, a=$-17/6$, $b = 3/2$, $c = 3/2$, and $d = -1/6$ are used. The second-order derivative approximation is implemented similarly, and details about it can be found in [83].

Numerical filters are used along the periodic directions to eliminate short-length scales created by the nonlinear interactions, and physical dissipation effectively manages the numerical noise along the radial direction. Since the variables are periodic over the y and z domains, the filtering is done in the Fourier space by decomposing the function f into its Fourier coefficients [83],

$$f(y) = \sum_{k=-N/2}^{k=N/2} \hat{f}_k \exp\left(\frac{2\pi k y}{N}\right) \tag{4.4}$$

where N is the number of nodes in the y direction. To simplify the expression 4.4, a scaled wavenumber is used $w = 2\pi k/N$ with a domain $[0, \pi]$.

The filtered values at node y_i, $\hat{f}_i$, is approximated as [83],

$$\begin{aligned}\beta \hat{f}_{i-2} + \alpha \hat{f}_{i-1} + \hat{f}_i + \alpha \hat{f}_{i+1} + \beta \hat{f}_{i+2} = a f_i + \frac{d}{2}(f_{i+3} - f_{i-3}) \\ + \frac{c}{2}(f_{i+2} - f_{i-2}) + \frac{b}{2}(f_{i+1} - f_{i-1})\end{aligned} \tag{4.5}$$

The solution of Eq. 4.5 is associated with a transfer function, $T(w)$,

$$T(w) = \frac{a + b\cos(w) + c\cos(2w) + d\cos(3w)}{1 + 2\alpha\cos(w) + 2\beta\cos(2w)} \tag{4.6}$$

with $T(\pi) = 0$ required for the filters which means $(dT/dw)(\pi) = 0$. An additional constraint is imposed which is $\frac{d^2T}{dw^2}(\pi) = 0$. Imposing a sixth-order accuracy the different coefficients can be derived $\beta = \frac{3-2\alpha}{10}$, $a = \frac{2+3\alpha}{4}$, $b = \frac{6+7\alpha}{8}$, $c = \frac{6+\alpha}{20}$, and $d = \frac{2-3\alpha}{40}$. The value of the $\alpha \leq 0.5$ parameter is given by the user to select the degree of filtering with $\alpha = 0.5$, meaning that no filter is applied ($T = 1$).

4.2 JOREK

The nonlinear extended MHD code JOREK is used to solve the set of Eq. 3.39-3.42 in toroidal geometry. The code is structured in a modular way, allowing for the implementation of different physics models without impacting other parts of the code [84]. The model of interest for the RE studies is the so-called model600. This model solves a set of RMHD equations in terms of the normalized variables $[\psi, u, j, \omega, T, \rho, n_{re}]$ where u is the stream function φ, ω is the vorticity U, and T is the temperature. The complete set of equations can be found in Ref. [80]. Here, only the equations of interest for the study of the RE termination problem are described (Eq. 3.39-3.42).

4.2.1 JOREK spatial discretization

The JOREK spatial discretization uses a hybrid technique combining aspects of spectral and finite element methods. Fourier harmonics are used to take advantage of the Tokamak toroidal periodicity along the toroidal direction. This reduces the computational time and allow to isolate and study the different types of instabilities characterized by the toroidal mode number n and their non-linear interactions [84]. A 2D finite element basis constructed with Bézier surfaces is employed in the poloidal plane. In each element, the JOREK variables and the (R,Z) coordinates are interpolated with third-order Bernstein polynomials with local coordinates (s,t). This decomposes the poloidal plane into quadrilateral cells like the one shown in the right panel of Fig. 4.1. These surfaces can be easily shaped and aligned to the magnetic field topology to efficiently represent the radial and angular anisotropy of the MHD modes. The toroidal coordinate system (R,Z,ϕ) used in JOREK is also depicted in the left panel.

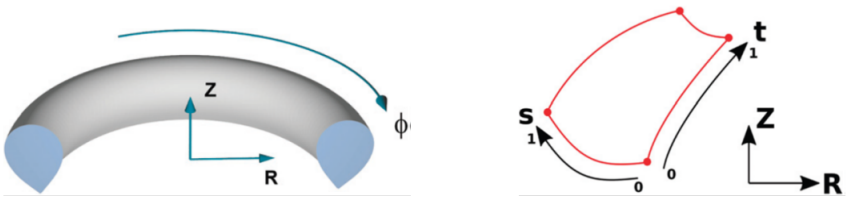


Fig. 4.1 Left panel: Toroidal coordinate system used in JOREK. Right panel: A 2D Bezier element in R-Z space. Reproduced from [80]

In the poloidal plane, the coordinates $\mathbf{R} \equiv (R,Z)$ and the JOREK variables, such as ψ, within a Bezier element are given as [84],

$$\mathbf{R}(s,t) = \sum_{i=1}^{4}\sum_{j=1}^{4} \mathbf{R}_{i,j} B_{i,j}(s,t) \tag{4.7}$$

$$\psi(s,t) = \sum_{i=1}^{4}\sum_{j=1}^{4} \psi_{i,j} B_{i,j}(s,t) \tag{4.8}$$

where $B_{i,j}(s,t)$ are polynomial basis functions. These functions include the geometrical properties of the element. The index i loops over the four vertices of the quadrilateral element and the j index loops over the four degrees of freedom related to the third order polynomials. The complete decomposition including the toroidal dependence is given by a real Fourier series

$$\psi(s,t,\phi) = \psi_0(s,t) + \sum_{n=1}^{N-1} \left(\psi_n^c(s,t)\cos(n\phi) + \psi_n^s(s,t)\sin(n\phi)\right) \tag{4.9}$$

where N is the total number of toroidal harmonics including the axisymmetric mode $(n = 0)$. This formulation allows writing the unknowns as a set of coefficients (ψ_{ijn}) which can be found through a set of linear equations written in the matrix form $\mathbf{A} \cdot \mathbf{x} = \mathbf{b}$. The matrices $\mathbf{A}$ and $\mathbf{b}$ are obtained through the Galerkin finite element method. An example of the application of this method can be found in Ref. [84].

4.2.2 JOREK time discretization

JOREK employs a fully implicit time scheme, preventing the time step from being affected by the CFL (Courant-Friedrichs-Lewy) condition. This condition ensures that the numerical solution of partial differential equations remains stable by limiting the size of the time step based on the spatial resolution and the speed of wave propagation in the system. In the case of an implicit technique, the ratio between time step δt and grid size δx is no longer constrained by numerical instabilities, as with the third-order Adam Bashford time scheme, which is explicit. Consequently, the time step can be adapted to instability characteristic time, which can go from $0.5-5$ Alfvèn times (in case of ELMs) to 10000 Alfvèn time (in case of slowly

growing resistive mode) [84]. However, an implicit scheme is more computationally demanding.

To perform the time discretization, the MHD equation are written as [84],

$$\frac{\partial \mathbf{F}(\mathbf{u})}{\partial t} = \mathbf{G}(\mathbf{u}) \tag{4.10}$$

where $\mathbf{u}$ is the unknowns variables vector and **F,G** are operators applied to $\mathbf{u}$. This system of equations can be linearized by a time-evolution scheme as [84],

$$\left[(1+\varepsilon)\left(\frac{\partial \mathbf{F}}{\partial \mathbf{u}}\right)^{k} - \delta t\theta\left(\frac{\partial \mathbf{G}}{\partial \mathbf{u}}\right)^{k}\right]\delta\mathbf{u}^{k} = \delta t\mathbf{G}^{k} + \varepsilon\left(\frac{\partial \mathbf{F}}{\partial \mathbf{u}}\right)^{(l-1)}\delta\mathbf{u}^{k-1} \tag{4.11}$$

where $\delta\mathbf{u}^{k} = \mathbf{u}^{k+1} - \mathbf{u}^{k}$ at the k time step and θ and ε are numerical parameters that depend on the adopted time scheme. The two time schemes implemented in JOREK are the Crank-Nicholson with $(\theta = 0.5, \varepsilon = 0)$ and Gears schemes with $(\theta = 1, \varepsilon = 0.5)$ [84].

4.2.3 Simulation steps

A JOREK simulation consists of different phases, briefly described in this subsection. First, a grid is generated, and a computational domain is defined. At this step, the indices and the coefficients $\mathbf{R}_{ij}$ of Eq. 4.7 are computed at each node. Once the grid is generated, which is usually a polar grid, the Grad-Shafranov (GS) equation is solved to find the initial equilibrium [85],

$$R^2\nabla\cdot\left(\frac{1}{R^2}\nabla\right)\psi = -R^2p'(\psi) - FF'(\psi) \tag{4.12}$$

where $p' = dp/d\psi$ is the pressure derivate, and $F = RB_\phi$ (with B_ϕ the toroidal magnetic field) is the poloidal current stream function with $F' = dF/d\psi$ its derivative, and both are a function of the poloidal flux ψ.

We consider a pressure-less system. Therefore, the Eq. 4.12 reduces to,

$$FF' = R^2\nabla\cdot\left(\frac{1}{R^2}\nabla\right)\psi = -Rj_\phi \tag{4.13}$$

Therefore, the solution of the GS equation provides the equilibrium toroidal current profile, which in turn gives the safety factor profile. To solve the Eq. 4.12, the user must provide the p', FF' and the poloidal flux on the domain's boundary.

The solution of the GS equation allows for the construction of a flux-aligned grid with the geometry of the found flux surfaces. This step is followed by the time evolution of the $n = 0$ mode to obtain a steady state. Once this is found, the Fourier harmonics chosen by the user can be initiated as small perturbations. When the toroidal modes become large enough, the non-linear phase occurs where the modes' nonlinear coupling can take place. In our case, this nonlinear coupling leads to the stochastizaton of the magnetic field, as shown in chapter 6.

4.3 FLUKA

FLUKA, which stands for FLUktuierende KAskade, is a versatile Monte Carlo code widely used for simulating particle transport and their interactions with materials. The code can simulate various particles such as electrons, photons, and neutrons, making it suitable for a wide range of applications. This study used FLUKA to obtain the energy deposition profiles in Beryllium and Tungsten.

FLUKA is a versatile tool that allows different ways to study electron transport in materials. In this analysis, we investigated the impact of Brehmstrahlung on the overall energy deposition pattern during RE-material interaction by adjusting the photon production threshold. This adjustment was made to examine energy deposition profiles far from the surface in different materials by artificially modifying the minimum energy at which photon generation begins.

In FLUKA, the optimal step length for sampling a particle's mean free path is automatically selected based on material and particle properties using the multiple scattering method [81]. This method ensures that the results remain insensitive to the step size while also enhancing accuracy by imposing a maximum fraction of total energy that can be lost in a step. This constraint governs the selection of the step size.

The simulations in our study used the default value for the maximum fraction of total energy lost in a step, which is set at 20% for electrons [81]. However, tests

were done to assess the appropriateness of this default value in the context of our studies, as discussed in chapter 7.

The FLUKA simulation software uses a multiple-scattering algorithm to simulate how electrons move through materials. It is based on the Moliere theory and is designed to save CPU time by allowing multiple small-angle scatterings during each step without tracking the particle trajectory after each scattering event. The Moliere theory assumes small-angle deflections of charged particles within the material. It calculates a probability distribution for the particle scattering angle, considering the cumulative effect of numerous small deflections during a step. After each step, the code randomly selects the scattering angle from this probability distribution based on material and particle properties. Any energy lost during the step is distributed over the entire step. Moreover, if the energy lost during the step exceeds the threshold set for delta ray production, secondary electrons are produced [81]. That is, by transferring kinetic energy to the electrons in the outer shells of the material atoms, an energetic electron can cause the atomic electron to leave the atom.

Moller and Bhabha scattering theories describe the cross-section for the collision-stopping power in the code [86]. This cross-section represents the mean energy loss per unit path length due to ionization and excitation and scales as Z. Whereas the mean energy loss per unit path length due to Bremsstrahlung radiation, scaling as Z^2, is represented by the cross-section for radiative stopping power. Information about this cross-section is given by the Berger and Seltzer (NIST) database [87]. The selected energy distribution function governs the relative importance of these events in our study. In particular, since a beam with the highest maximum energy of approximately 7 MeV was selected, the collision-stopping power dominates over the radiative stopping power for both materials [88]. At the same time, for Tungsten, radiation loss via Bremsstrahlung is comparable to ionization and excitation loss, resulting in significant photon production, as depicted in Fig. 4.2, showing the radiation yield as a function of electron energy for Tungsten (red) and Beryllium (green) [88].

The radiation yield, within the energy range of interest ($E_{kin} < 7\,\mathrm{MeV}$), refers to the average fraction of the initial electron energy that is converted into Bremsstrahlung energy as the electron slows down to a complete stop. Notably, this fraction is significantly higher for Tungsten compared to Beryllium.

The radiation length, which indicates the distance over which a particle energy decreases by a factor of 1/e, is greater for photons than for electrons. This property allows photons to penetrate deeply into a material and deposit their energy in regions far from the impact surface.

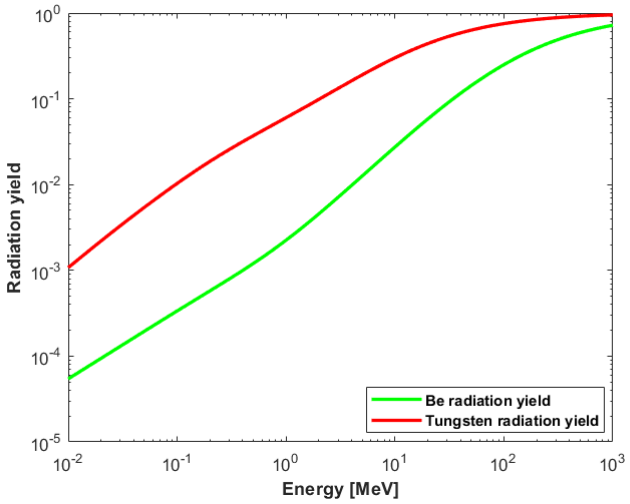


Fig. 4.2 Be (green) and W (red) radiation yield as a function of electron energy in MeV. Reproduced from [8]

The transport of particles characterized by energy below the threshold for secondary electron production is modelled through the continuous slowing-down approximation (CSDA) [86]. This method computes the distance a particle with a certain energy can travel before reaching the energy threshold at which it is supposed to deposit all its energy. The energy is deposited at the point where the threshold is met. This distance, known as the CSDA range, is computed through the total stopping power of the material given by the sum of collision and radiative stopping powers. The total stopping power is assumed to equal the energy loss rate along the particle path. [88].

To accurately simulate the energy deposition of low-energy particles, it is important to adjust the grid resolution in relevant directions and the threshold values for particle absorption by the material. Figure 4.3 shows the CSDA range for electrons as a function of energy for Beryllium (green) and Tungsten (red). The CSDA ranges for different materials, obtained from [88], were normalized by the material density ($d_{Be} = 1.8 g/cm^3$ and $d_W = 19.25 g/cm^3$) for comparison with the bin dimension in cm. A bin represents the length of each cell into which the energy deposition (ED)

detector spatial grid is divided along the X, Y, and Z axes. If the bin dimension along the analyzed direction exceeds the CSDA range, the particle will stop at an incorrect location. For instance, a transport threshold of 100 keV would mean a CSDA range of 1.6×10^{-3} cm for Tungsten. This means the bin dimension along the Z direction should be at most 1.6×10^{-3} cm to ensure an accurate stopping depth.

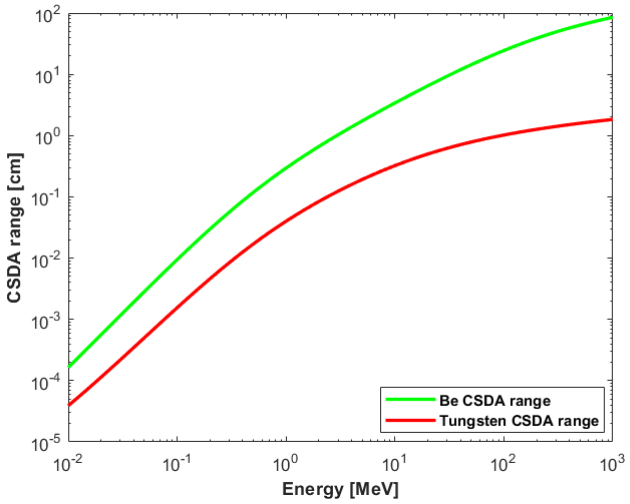


Fig. 4.3 Be (green) and W(red) CSDA range in cm as a function of energy. Reproduced from [8]

4.4 FREEFEM++

Runaway electrons can cause the melting of the plasma-facing components. To reliably assess the damage to the PFC, a detailed thermal model that can simulate the physics of the phase change in the material is required.

Modelling the melting process is considered a moving boundary problem because the location of the interface between the two phases is not known [89]. The moving interface problem has been addressed through the development of various techniques over the past few decades, such as the variable time step grids [90], integral methods [91], and boundary immobilization techniques [92]. However, these techniques are effective for 1D problems, with a single point unequivocally determining the interface position. In a 2D problem, instead, their applicability may be limited due to the complex shape of the two-phase interface. Therefore, this study has implemented the apparent heat capacity (AHC) formulation, previously used in Ref. [93]. This

formulation allows the computation of the moving interface by solving a single heat diffusion equation accounting for the latent heat of fusion through an implicit technique [94].

The AHC method considers the phase change to occur in a specific temperature range centred around the material melting temperature (T_m) with a width of δ. In this interval, the material is characterized by a mixture of the two phases and the fraction of the initial phase is represented by a differentiable function θ. The material density and its specific enthalpy are also expressed as a combination of the two phases.

$$\rho = \theta \cdot \rho_1 + (1-\theta) \cdot \rho_2 \tag{4.14}$$

$$h = \frac{1}{\rho} \cdot (\theta \rho_1 h_1 + (1-\theta)\rho_2 h_2) \tag{4.15}$$

Through the specific enthalpy definition, it is possible to compute the heat capacity as,

$$c_p = \frac{\partial h}{\partial T} = \frac{1}{\rho} \cdot (\theta \rho_1 c_{p,1} + (1-\theta)\rho_2 c_{p,2}) + \Delta h_f \cdot \frac{d\alpha_m}{dT} \tag{4.16}$$

where α_m is the mass fraction, set to $-1/2$ before the occurrence of the phase change and switches to $1/2$ following the transformation and is defined as,

$$\alpha_m = \frac{1}{2} \cdot \frac{(1-\theta)\rho_2 - \theta\rho_1}{\rho} \tag{4.17}$$

The AHC method is implemented in open-source Finite Element software called FreeFEM++ [82]. The FreeFEM++ solver has been incorporated into a Python wrapper, automatically generating the required inputs and commencing the execution process. This integration improves the adaptability of the tool, potentially enabling it to analyze any geometry and load configurations in FLUKA.

In this work, the tanh function was selected as the differentiable function θ, due to its derivability and possession of two horizontal asymptotes. The specific form of the chosen θ function is provided in equation 4.18, whereas the temperature interval considered for the melting is $\delta = 10.0\,K$.

$$\theta(T) = \frac{1}{2} \cdot (1 + \tanh(T_m - T)) \tag{4.18}$$

The assumption of a constant material density during the phase change allows to write the mass fraction as,

$$\alpha_m = \frac{1}{2} - \theta(T) \tag{4.19}$$

The expression for the latent heat contribution to the specific heat (c_L) valid within the temperature interval of the phase change is,

$$c_L(T) = \Delta h_f \cdot \frac{d\alpha_m}{dT} = \Delta h_f \cdot \frac{1}{2} \cdot \left(\frac{1}{cosh(T_m - T)} \right)^2 \tag{4.20}$$

Outside of the melting temperature interval, the contribution of the latent heat is zero.

This implementation was benchmarked against a problem from Ref. [89] to validate the thermal tool. The reference problem consisted of heating the front face of an infinite slab with a constant heat flux to initiate a melting front. This melting process is monitored through the temperature measurements of the front and back faces and the melting interface position. Details about the boundary conditions and material thermal properties can be found in Ref. [89].

The problem described in Ref. [89] is inherently 1D. However, to validate our 2D model, the infinite slab has been represented in 2D by a thin slice with the same length as the width of the slab. Furthermore, periodic boundary conditions have been imposed on the upper and lower faces. Fig. 4.4 depicts the computational domain and boundary conditions used for the benchmark.

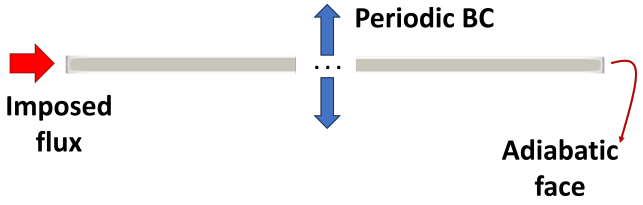


Fig. 4.4 Representation of the problem computational domain and the adopted boundary conditions. The slab width dimension has been cut to improve readability. Reproduced from [8]

The comparison between the results obtained from the AHC method implemented in FreeFEM++ and the findings reported in Ref. [89] is shown in Fig. 4.5. A good

agreement was reached between the two studies regarding the local temperature evolution and the position of the melting front, which validated our model. In particular, the left panel of Fig. 4.5 shows the temporal evolution of the melting front position. In contrast, the right panel shows the temporal evolution of the front and back face temperature.

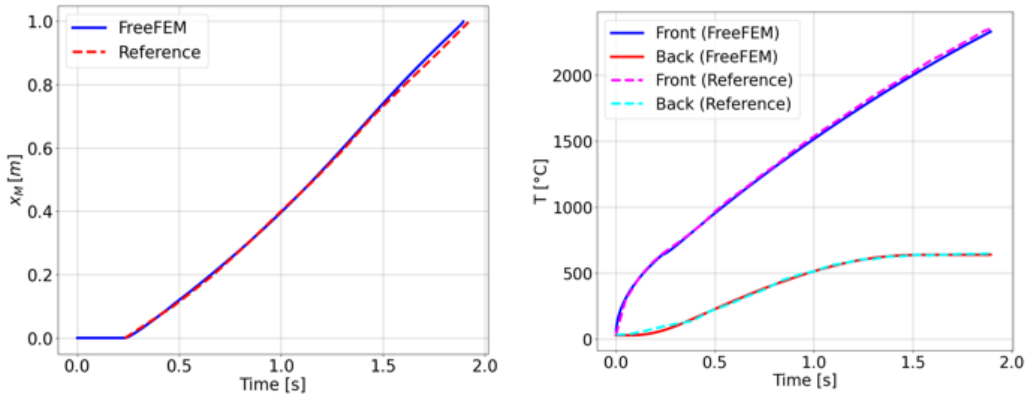


Fig. 4.5 Comparison between the position of the melting front x_M (left panel) and front and back face temperature (right panel) obtained with the AHC method developed in FreeFEM++ and the reference results [89]. Adapted from [8]

Chapter 5

Postdisruption plasma stability in the presence of a runaway electron current

The MHD stability of a post-disruption plasma can significantly be affected by the presence of a RE current as shown in section 3.4. As underlined in the mentioned section, the problem has been investigated analytically and numerically by Helander et al. in Ref. [3] and by Liu et al. in Ref. [4], assuming a fluid description of the runaway current. In the former study, the linear growth rate and the saturation magnetic island amplitude have been calculated analytically and confirmed numerically within the context of resistive MHD by considering an RE current that peaked at the rational surface where reconnection occurs. The limitation of a symmetric RE current profile with respect to the rational surface was rested in Ref. [4], and the linear theory presented in Ref. [3] has been expanded to cylindrical geometry. Adopting an asymmetric current profile in the presence of a single helicity perturbation in 3D configurations allowed the authors to observe the presence of a new inner layer within the resistive inner layer. The width of this inner layer is comparable with the electron skin depth, which could play a role in the evolution of the system.

However, the numerical investigation carried out in Ref. [3] leaves some questions unanswered. In particular, a slab geometry with periodic boundary conditions in the radial geometry and a simplified single-fluid model have been adopted in Ref. [3]. When a periodic magnetic equilibrium is used, each linearly unstable mode is

characterized by two resonant surfaces, leading to the formation and growth of identical magnetic islands. If the size of the islands is smaller than the distance between the corresponding resonant surfaces, their mutual interaction can be disregarded. However, their interaction affects the nonlinear evolution of large magnetic islands. In Ref. [3], a periodic magnetic equilibrium was used due to the boundary conditions of the numerical solver. This equilibrium prevented an assessment of the saturation magnetic island amplitude for values of $\Delta' > 0.4$. Moreover, adopting the single fluid approach in Ref. [3] neglected the effects of electron inertia and Larmour radius on the evolution of the magnetic island. Even though the scales related to these two parameters are small in a post-disruption scenario due to the electron mass and high resistivity, they could become relevant in the presence of localized current layers. These layers arise in the presence of RE current and can affect the evolution of the global process.

The research conducted in this PhD aimed to address the limitations mentioned and introduce new simulations using the SCOPE3D code. This code allows the adoption of non-periodic boundary conditions in the radial direction, which eliminates the influence of boundary conditions. This allowed us to study the growth of magnetic islands up to the saturation without the issues caused by periodic boundary conditions, thereby correcting previous findings in Ref. [3] about the occurrence of bifurcation behaviour. The results from the SCOPE3D simulations and the analysis of the electron temperature effects using the ion sound Larmour radius parameter, ρ_s, are presented in section 5.1.

The linear theory discussed in Ref. [4] was verified using SCOPE3D in a 2D slab geometry. Our study highlighted the inner layer impact on the RE current evolution and compared it with the resistive layer. Additionally, we explored the nonlinear regime to investigate how an asymmetric current profile affects the island evolution. This enabled us to analyze the island rotation during nonlinear evolution and the development of multiple inner layers on the RE current. The findings of this study are detailed in section 5.2 where the results on the investigation of the electron inertia role in determining the evolution of the magnetic reconnection are also presented using the two-fluid, collisional plasma model.

Moreover, a verification exercise carried out with the JOREK code in a cylindrical configuration and single helicity regime is described in section 5.3. This exercise

was necessary to assess JOREK capability to reproduce the results obtained with SCOPE3D before analyzing complex problems such as magnetic stochasticity.

5.1 Symmetric case

This part of the analysis aimed to verify the analytical derivations presented in Ref. [3] with SCOPE3D and to extend the study by also considering the effect of the electron temperature through the ion sound Larmour radius parameter in the Eq. 3.27-3.30. The electron inertia effects were neglected for this stage of analysis. Furthermore, Ref. [3] considered a 2D slab geometry, whereas, with SCOPE3D, it is possible to consider a 3D slab geometry to implement a perturbation dependent on the coordinate along the direction of the guiding magnetic field. This is the toroidal direction, z. Meanwhile, the other directions are x and y, corresponding to the radial and poloidal directions.

The perturbation considered for the study consists of a single helicity (SH) perturbation, giving rise to a spontaneous magnetic reconnection event in a sheared, unstable magnetic equilibrium configuration with $B_y = B_y(x)$. This SH perturbation has the following form for a generic field,f,

$$f(x,y,z,0) = \sum_{k_y,k_z} \hat{f}_{k_y,k_z}(x)\exp(ik_y y + ik_z z) = \sum_{k_y} \hat{f}_{k_y}(x)\exp[ik_y(y+\alpha z)] \tag{5.1}$$

The transformation introduced in section 3.2 was applied to Eq. 5.1 to study a 3D problem in a 2D approximation with $\alpha = k_z/k_y$. In the symmetric case, $\alpha = 0$ was considered for the purpose of the study.

As in Ref. [3], a static equilibrium with a Harris-type sheared magnetic field and equilibrium current carried by the runaway electrons was considered. That is,

$$\varphi(x) = 0 \tag{5.2}$$

$$\psi_{eq}(x) = -\log[\cosh(x)] + \alpha x \tag{5.3}$$

$$j_{RE_{eq}} = j_{eq}(x) = -\nabla^2 \psi_{eq}(x) \tag{5.4}$$

For the numerical simulation, a resolution of $ny = 96$ grid points was adopted along the y-direction in the SCOPE3D code. Meanwhile, for the x-direction, nx = 1200 grid points were adopted on the non-equispaced grid so as to guarantee a resolution of $dx = 0.0038$ $[A.U.]$ around x = 0, where the tearing instability takes place. Since we aimed to benchmark our results against those in Ref. [3], a pure resistive case ($d_e = 0$) and the limit $c/v_A = 1$ was considered. Equations 3.27-3.30 with $d_e = 0$ and $\rho_s = 0.1$ (when considering the electron temperature effects, otherwise $\rho_s = 0$) are integrated over the domain $[-L_x, L_x] \times [-L_y, L_y]$ with $L_x = 3\pi$ while L_y was varied to consider different degrees of instability according to Eq. 3.17.

Since a non-periodic equilibrium was considered, that is $B_{eq} = -\partial\psi/\partial x = \tanh(x)\mathbf{e}_y$, the evolution of a single magnetic island can be studied up to the saturation without the cross-talking between two islands as happens in the periodic equilibrium case of Ref. [3].

5.1.1 Linear analysis

For the linear analysis, a scan in the stability parameter, Δ', was carried out to verify the numerical results with those given by the analytical derivation present in Ref. [3]. This scan has a fixed normalized resistivity of $\eta = 3 \times 10^{-4}$. As shown in Fig. 5.1, in the absence of runaways and ρ_s, the analytical formula for the linear growth rate, γ, is given by Eq. 3.19 (green curve). In contrast, in the presence of runaways and the absence of ρ_s, the dispersion relation given by Eq. 3.18 was used (blue curve).

When the electron temperature effect is considered, the dispersion relation becomes [95],

$$\frac{\gamma^{3/2}}{\eta^{1/2} k_y}\gamma = 0.32\rho_s\Delta' \tag{5.5}$$

The relation 5.5 has been derived in [95] without considering the RE. However, in our case, the results of this relation (red curve in Fig. 5.1) are also compared with the numerical results obtained in the presence of RE.

As can be observed in Fig. 5.1, in the absence of ρ_s, the numerical results in the presence (blue dots) and absence (green dots) of RE perfectly agree with the respective analytical derivations. Meanwhile, in the presence of ρ_s, there is a good agreement between the analytical relation, Eq. 5.5, and the numerical results with (red dots) and without (magenta dots) RE.

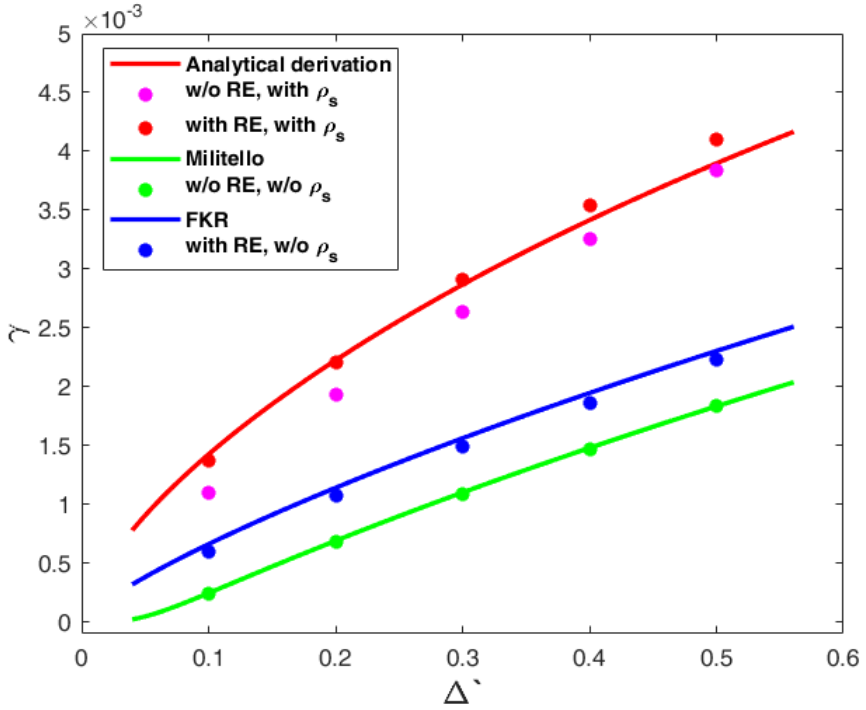


Fig. 5.1 Numerical and analytically derived linear growth rates, γ, for a pure resistive reconnecting mode driven by a runaway current (blue points and blue curve) compared with the case without runaway current (green points and green curve) along with the numerical γ with (red points) and without a RE current (magenta points) compared with the results of Eq. 5.5 in the presence of ρ_s (red curve). The growth rates are shown as a function of Δ'. Adapted from [7].

5.1.2 Non Linear analysis

For the nonlinear analysis, the analytical and numerical magnetic island widths at saturation, w, with and without RE, were compared, considering the effects of the electron temperature as well. In the presence of RE, the analytical relation given by Eq. 3.35 was used, whereas in the absence of RE, Eq. 3.36 was considered. The parameter, b, present in both relations is b=-2 for the magnetic equilibrium implemented in SCOPE3D. As a consequence, in the presence of RE, Eq. 3.35 becomes $w = 1.85\Delta'$ and in the absence of RE, Eq. 3.36 becomes $w = 1.22\Delta'$. These relations are plotted in Fig. 5.2 with the green curve representing the case with RE and the red curve representing the case without RE, both in the absence of ρ_s. Comparing these analytical curves with the numerical results with (green dots) and without (red dots) RE, a perfect agreement was found for values of the

stability parameter $\Delta' < 1$. However, a discrepancy between the theoretical and the numerically observed widths in the presence of RE becomes apparent at values of Δ' around unity. This is because, at these Δ' values, the simulation parameters are outside the range of validity of the analytical theory as they deviate from the asymptotic limit of the small Δ' regime ($\Delta'\eta^{1/3} \ll 1$). However, these simulations were essential to verify if a bifurcation exists in the sequence of saturated equilibria, as postulated in Ref. [3]. Our investigation found no bifurcation, and the island can reach saturation, even for values of Δ' around 1.

The numerical widths observed in the presence of ρ_s (blue plus marker with RE and yellow plus marker without RE) are equal to those without ρ_s as shown in Fig. 5.2. This is because the electron temperature does not affect the saturation width since microphysics at the ion sound Larmor radius scale does not play a role in determining the width of the saturated island.

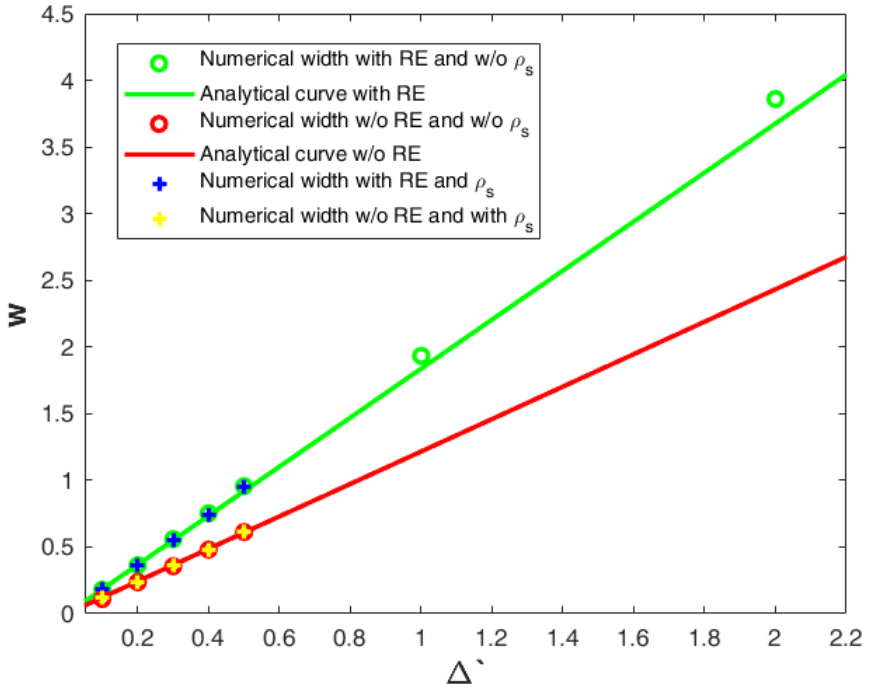


Fig. 5.2 Numerical and analytically derived saturation island widths, w, for the pure resistive reconnecting mode driven by a RE current (green dots and green curve) compared with the case without RE (red dots and red curve). The plus markers refer to the ρ_s cases. Adapted from [7].

The evolution of the total current distribution accounting for the thermal and RE current can be observed in Fig. 5.3 for the simulation with $\Delta' = 0.5$. The left panel displays the 2D distribution of the total current with highlighted closed magnetic surfaces to show the magnetic field topology. In the right panel, the current density profiles are plotted as a function of the radial coordinate for two different y locations. The blue curve represents a profile across the magnetic island O-point, the red curve across the X-point, and the green curve represents the initial equilibrium. Comparing the current profile across the island O-point with the initial distribution a homogenization of the current density within the magnetic island can be observed, which is typical of resistive tearing modes. On the other hand, the reduction of the current peak at the X-point is due to the movement of RE escaping along the open magnetic surfaces.

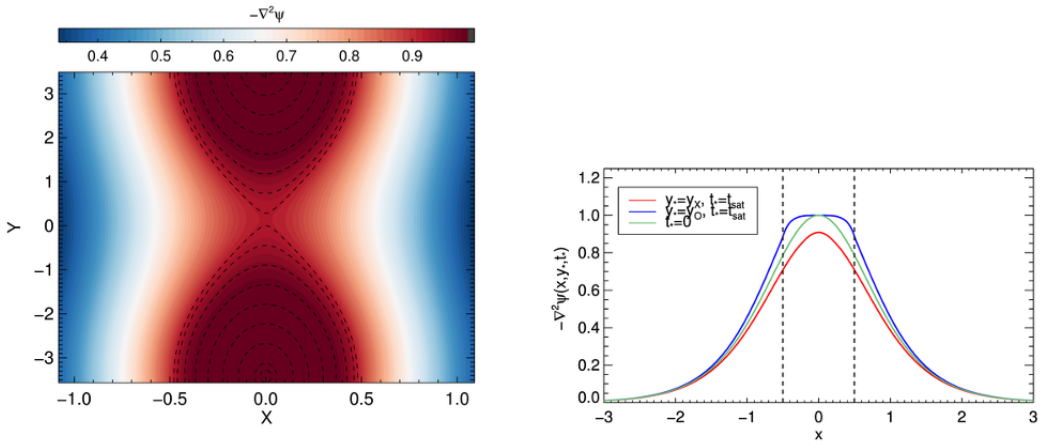


Fig. 5.3 Total current density distribution at saturation for the case $\Delta' = 0.5$. Left panel: contour plot of the current density with superimposed magnetic surfaces. Right panel: radial profiles for island X-point (red curve) and O-point (blue curve) compared with the equilibrium profile (green curve). The dashed line defines the width of the magnetic island at saturation. Reproduced from [6].

5.2 Asymmetric case

With respect to the symmetric case, for this analysis $\alpha = k_z/k_y \neq 0$, thus the equilibrium magnetic field is given by $B_{yeq} = \tanh(x) - \alpha$ with the rational surface located at $x_s = \tanh(\alpha)$ and the runaway current radial profile is peaked at $x = 0$. Therefore, a mismatch occurs between the peak and rational surface location and $J'_{RE0} \neq 0$ at the

rational surface. A finite value of the equilibrium RE current density radial derivative at the rational surface causes the island to undergo a rotation with frequency defined by Eq. 3.38. Moreover, the RE current is characterized by an inner layer whose analytical expression is given by Eq. 3.37, and it is much narrower than the resistive layer defined by Eq. 3.20.

Since the width of the microlayer is proportional to the c/v_A ratio for the asymmetric simulations, $c/v_A = 1, 10$ have been considered to study the inner layer behaviour. Moreover, in the presence of oblique mode ($k_z/k_y \neq 0$), the definition of the stability parameter has to be corrected according to Ref. [96],

$$\Delta' \approx 2\left(\frac{1}{k} - k\right)\left[1 + \frac{\tanh^2 x_s}{2}\left(1 + \frac{1}{1-k}\right)\right] \tag{5.6}$$

where $k \equiv |\mathbf{k}|$ with $\mathbf{k} = k_y\mathbf{e}_y + k_z\mathbf{e}_z$.

Regarding the initial conditions and the SH perturbation, the Eq. 5.2-5.4 and Eq. 5.1 are valid also here with the only difference that $\alpha \neq 0$.

The single fluid model (Eq. 3.27-3.30 with $d_e = 0$,$\rho_s = 0$) was used to reproduce the linear theory presented in Ref. [4] and to extend the numerical work to the nonlinear regime. At the same time, the effects of the electron inertia were also investigated through the two-fluid model (Eq. 3.27-3.30 with $\rho_s = 0$).

The equations are integrated over a domain $[-L_x, L_x] \times [-L_y, L_y]$. $L_x = \pi$ has been used for the linear simulation, while for nonlinear simulations, $L_x = 3\pi$. This was done to save computational time during the linear evolution and to avoid spurious boundary effects during the nonlinear evolution. Different resolutions ranging from $ny = 96$ to 192 have been used along the periodic direction y, depending on the box size given by the stability parameter. For the x direction, the number of grid points has been varied from 1200 to 4800 on the non-equispaced grid to have an adequate resolution in the reconnection region.

5.2.1 Linear analysis

To verify the dispersion relation, Eq. 3.38, with SCOPE3D, the simulations were performed with $\Delta' = 1.015$, $c/v_A = 1$ and normalized resistivity values in the $[1 \times 10^{-3}, 1 \times 10^{-6}]$ interval. The results of this verification are shown in Fig. 5.4 where a

perfect agreement can be observed between the analytical, linear growth rate ($Re(\gamma)$, blue curve) and rotation frequency ($Im(\gamma)$, rust curve) and the numerical $Re(\gamma)$ (blue dots) and $Im(\gamma)$ (rust dots).

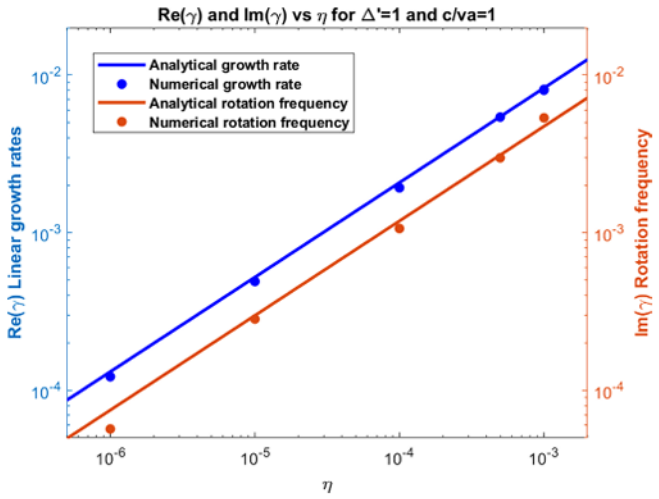


Fig. 5.4 Analytical growth rate, $Re(\gamma)$ (blue line) and rotation frequency, $Im(\gamma)$ (rust curve) given by Eq. 3.38 compared with the numerical growth rate (blue points) and rotation frequency (rust points) for η in the $[1\times10^{-3}, 1\times10^{-6}]$ interval, $\Delta' = 1.015$ and $c/v_A = 1$, $d_e = 0$, $\rho_s = 0$. Reproduced from [7].

For the analysis of the inner layer present on the RE current, $\Delta' = 6.057$ was chosen, even though the numerical growth rates (blue points) in Fig. 5.5 are not as close to the analytical results (blue curve) as they are for the more asymptotic case $\Delta' = 1.051$. Additionally, in this case, we have adjusted the resistivity range to $[1\times10^{-4}, 5\times10^{-7}]$ in order to stay within the small Δ' regime limit.

The value of $\Delta' = 6.057$ was chosen because $\Delta' = 1.051$ did not provide enough numerical precision to determine the inner layer widths at $c/v_A = 1$. Increasing the numerical resolution with $\Delta' = 1.051$ would have made the analysis with $c/v_A = 10$ computationally infeasible. Moreover, an accurate measurement of δ_2 requires increasing grid points along the radial direction with decreasing resistivity. This, however, led to reducing the radial extension of the domain to ensure sufficient spatial resolution in the reconnection region at small resistivity values. However, the choice of a smaller domain makes the system less asymptotic, which partially explains the differences observed between the numerical (blue dots) and analytical (blue line) growth rates in Fig. 5.5. Also, the numerically obtained rotation frequencies (rust dots) for $\Delta' = 6.057$ match the theoretical prediction (rust line) as seen in Fig. 5.5,

since the rotation frequency is independent of the value of Δ', in accordance with Eq. 3.38.

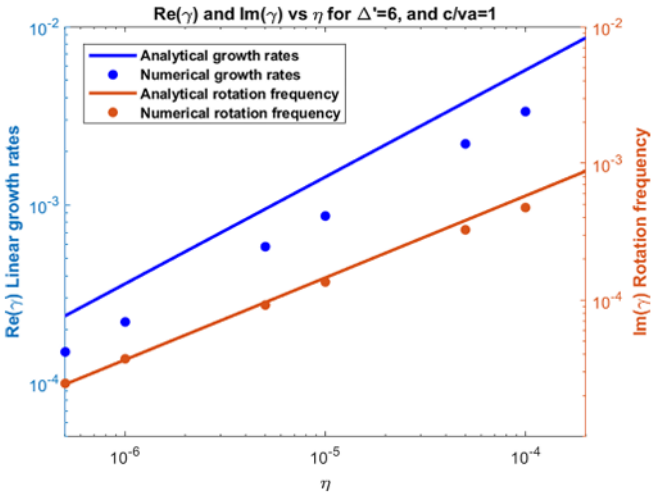


Fig. 5.5 Analytical growth rate, $Re(\gamma)$ (blue line) and rotation frequency, $Im(\gamma)$ (rust curve) given by Eq. 3.38 compared with the numerical growth rate (blue points) and rotation frequency (rust points) for η in the $[1\times10^{-3}, 5\times10^{-7}]$ interval, $\Delta' = 6.057$ and $c/v_A = 1$, $d_e = 0$, $\rho_s = 0$. Reproduced from [7].

The modulus of the linear eigenfunctions for mode $m = 1$ of the total current (blue curve), RE current (red curve), and thermal current (green curve) are shown in Fig. 5.6 as a function of the radial direction to show the characteristics of the inner layer on the RE current at different c/v_A ratio. In the left panel, the simulation results conducted with $c/v_A = 1$ are shown, while in the right panel, the results of the simulation with $c/v_A = 10$ are depicted. In both cases $\eta = 1\times10^{-4}$, $\Delta' = 6.057$. In both panels, the presence of a resistive layer, δ_1, on the thermal current profile and of an inner layer, δ_2, on the RE current profile is highlighted. For convenience, in the text, the width of the layers is expressed in terms of their half-width. With $c/v_A = 1$ (left panel), the inner layer is much narrower than the resistive one, and the thermal current profile dominates the runaway current profile. However, with $c/v_A = 10$ (right panel), the RE peak is higher than the thermal current's. This is a result of the RE conservation, which causes the RE to distribute over a smaller area in the case of a thinner layer and reach a maximum higher than the thermal electrons' peak value.

In the left panel of Fig. 5.7, the numerically obtained inner layer widths, δ_2, are compared with the results of Eq. 3.37 at $c/v_A = 1$ (blue and green curves for

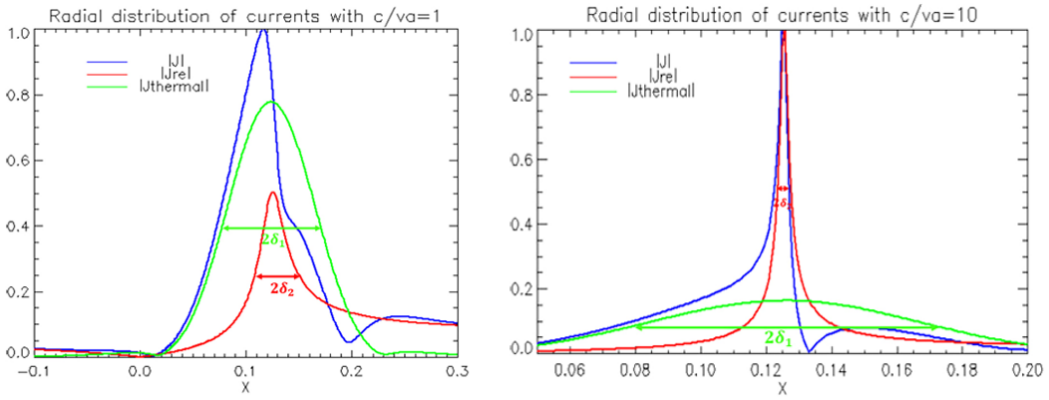


Fig. 5.6 Eigenfunction of mode 1 for total current (blue curve), runaway current (red curve) and thermal electrons current (green curve) profiles showing the inner layer δ_2 on the runaway current profile and the resistive layer δ_1 on the thermal electrons profile for $\eta = 1 \times 10^{-4}$, $\Delta' = 6.057$ and $c/v_A = 1$, $d_e = 0$, $\rho_s = 0$ in the left panel and $\eta = 1 \times 10^{-4}$, $\Delta' = 6.057$ and $c/v_A = 10$, $d_e = 0$, $\rho_s = 0$ in the right panel. Reproduced from [7].

numerical and analytical results, respectively) and $c/v_A = 10$ (red and magenta curves for numerical and analytical results, respectively). As can be observed in the figure, there is an order-of-magnitude difference between the two numerical curves following the Eq. 3.37. Moreover, a good agreement is found for both values of the c/v_A ratio. However, with $c/v_A = 10$ the simulations are limited to a resistivity interval between $[1 \times 10^{-4}, 5 \times 10^{-5}]$ due to computationally unfeasible high resolution required for resistivity values below this interval.

Meanwhile, in the right panel, the numerically obtained resistive layer widths, δ_1, are compared with the results of Eq. 3.20 at $c/v_A = 1$ (blue and green curves for numerical and analytical results, respectively) and $c/v_A = 10$ (red and green curves for numerical and analytical results, respectively). A good agreement is found between the simulation and theoretical results. Moreover, results from the higher ratio simulations show a better agreement with the theory since the simulation is more asymptotic in this case.

So far, the results presented were related to purely resistive cases based on the single fluid approach. If a two-fluid model is considered to account for the electron inertia effects through the electron skin depth, d_e, a change in the evolution of the system takes place. For this investigation, small values of d_e are considered to not significantly modify the linear growth rates observed in the purely resistive case. This was done to analyze the changes in the current distribution without altering the

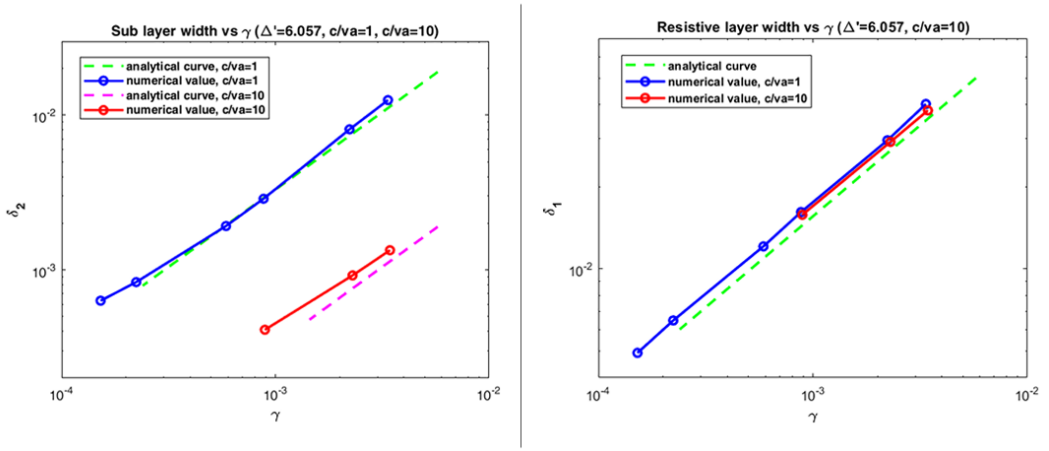


Fig. 5.7 Numerically obtained inner layer widths, δ_2 in a purely resistive case compared with the analytical derivation given in Eq. 3.37 in the left panel and numerically obtained resistive layer widths, δ_1 compared with the analytical derivation given in Eq. 3.20 in the right panel for different values of γ corresponding to η in the $[1\times10^{-4}, 5\times10^{-7}]$ interval, $c/v_A = 1, 10$ and $\Delta' = 6.057$. The green dashed line corresponds to the analytical curve for $c/v_A = 1$ and the magenta dashed line to the analytical curve for $c/v_A = 10$, while the blue curve represents the numerical results for $c/v_A = 1$ and the red curve for $c/v_A = 10$. The magenta curve in the right panel is absent since δ_1 is independent of c/v_A ratio Reproduced from [7].

growth rate of the tearing instability. The electron inertia effects on the modulus of the eigenfunction of mode $m = 1$ for the total (blue curve), runaway (red curve) and thermal (green curve) currents are shown in the left panel of Fig. 5.8. The current distributions are obtained for a case with $\eta = 1\times10^{-4}$ and $d_e = 0.05$, which is of the same order of magnitude as the expected d_e in a post-disruptive plasma.

As shown in the left panel of Fig. 5.8, electron skin depth does not affect the total and RE current distribution when $c/v_A = 10$. However, the thermal current distribution is no longer characterized by the characteristic Gaussian profile of width δ_1 as in the purely resistive case ($d_e = 0$). Instead, an oscillatory distortion appears around the rational surface. As depicted in the right panel of Fig. 5.8, the amplitude of this oscillation grows linearly with the d_e value (red curve, $d_e = 0.05$ and blue curve, $d_e = 0.1$).

As mentioned earlier, the presence of d_e does not modify the RE profile. Nevertheless, the rise of the oscillatory distortion strongly depends on the c/v_A ratio, i.e. the speed of RE. Indeed, with $c/v_A = 1$, this behaviour of the thermal current

was not observed. Consequently, the electron inertia effects may become even more important in realistic regimes characterized by $c/v_A \approx 100$.

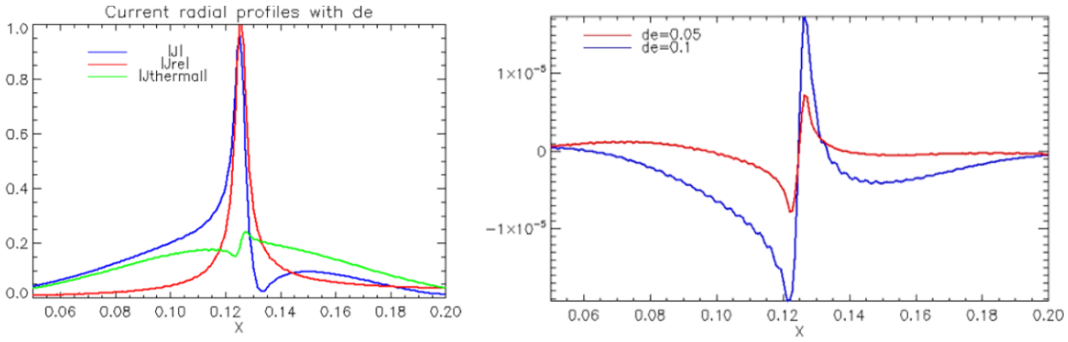


Fig. 5.8 Left panel: radial profile of the modulus of the $m = 1$ mode eigenfunction for total current (blue curve), runaway current (red curve) and thermal electrons current (green curve) for $\eta = 1e-4$, $\Delta' = 6.057$ and $c/v_A = 10$. $d_e = 0.05$, $\rho_s = 0$. Right panel: Radial profile of the eigenfunction distortion of thermal electrons current observed for $d_e = 0.05$ (red line) and $d_e = 0.1$ (blue line). The curves have been obtained by the difference $J_{th}(x) - A\exp(-(x-x_s)^2/2\delta_1^2)$ where $A = 3.28e-5$ when $d_e = 0.05$ and $A = 3e-5$ when $d_e = 0.1$. In both cases, $\eta = 1e-4$, $\Delta' = 6.057$ and $c/v_A = 10$. Reproduced from [7].

5.2.2 Non Linear analysis

In the absence of runaway electrons, according to magnetic reconnection theory, the transition to the nonlinear phase occurs when the width of the magnetic island becomes larger than the linear, radial scale of variation of the electron current, which corresponds to δ_1 in the formula 3.20. The situation becomes more complex when considering the impact of runaway electrons in an asymmetric configuration, as a new length scale, δ_2 in the formula 3.37, characterizing the runaway current, comes into play. In this scenario, the behaviour of runaway electrons becomes nonlinear when the magnetic island width exceeds δ_2. Since, as demonstrated in the linear analysis, δ_2 can be significantly smaller than δ_1, the transition to the nonlinear phase occurs earlier. This is illustrated in Figure 5.9, where the temporal evolution of the $m = 1$ mode eigenfunction modulus of the runaway (green) and thermal (blue) currents, along with the width of the island (rust colour) for a purely resistive case, is depicted. The vertical dashed lines mark the instants when the runaway (t_2) and thermal electron (t_1) currents deviate from linear growth. At these times, the size of the magnetic island is equal to δ_2 and δ_1 (horizontal dashed lines).

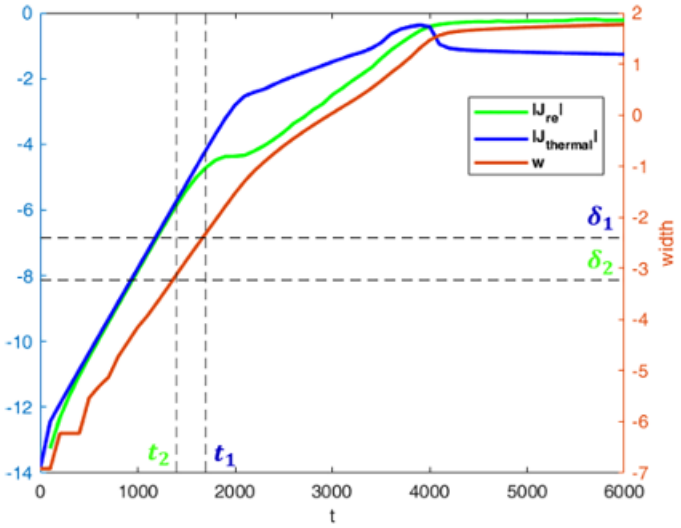


Fig. 5.9 Temporal evolution of the eigenfunction modulus of mode m=1 associated with the runaway (green) and thermal (blue) current, and the width of the islands (rust) for a purely resistive regime $\eta = 1 \times 10^{-4}$, $c/v_A = 1$ and $\Delta' = 6.057$. The vertical dashed lines identify the time instants when the transition to the nonlinear stage occurs for runaway ($t_2 = 1400$) and thermal electrons ($t_1 = 1700$). The dashed horizontal lines identify the magnetic island widths corresponding to these times. The sizes of the island at t_1 and t_2 are comparable with δ_1 and δ_2, respectively. Reproduced from [7].

When the runaway electrons reach the non-linear evolution, the radial distribution of j_{re} changes. This change is illustrated in Fig.5.10, which shows the eigenfunction modulus of the $m = 1$ mode for the RE current at two different time points within the range $t_2 < t < t_1$. At time t=1500, the radial profile resembles a Gaussian shape with width δ_2, while at t=1800, it transforms into a structure with two small-scale peaks. In physical space, this leads to a concentration of the perturbed RE current along the separatrices of the magnetic island, unlike in the linear phase where j_{re} peaks at the $X-$point.

As the thermal electrons become nonlinear, the combined effect of magnetic island growth and displacement along the y direction causes the RE current to spread out in a spiral pattern around the island O-point. This is illustrated in Fig. 5.11, where the left panel shows a contour of the perturbed RE current distribution and the corresponding magnetic island for the purely resistive case at $t = 2500$ with $\eta = 1 \times 10^{-4}$, $c/v_A = 1$, and $\Delta' = 6.057$. The right panel highlights the small-scale formation on the RE radial profile through a radial cut across the magnetic island O-point.

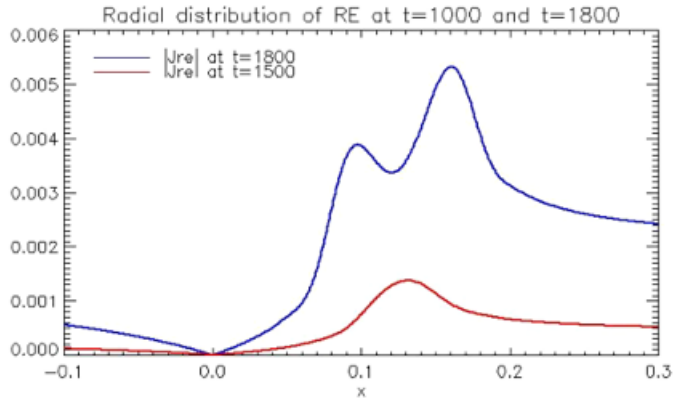


Fig. 5.10 RE radial profile distribution during the linear evolution (red) at t=1500 and during the runaways non-linear evolution at t=1800 for $\eta = 1 \times 10^{-4}$, $c/v_A = 1$ and $\Delta' = 6.057$, $d_e = 0$, $\rho_s = 0$. Reproduced from [7].

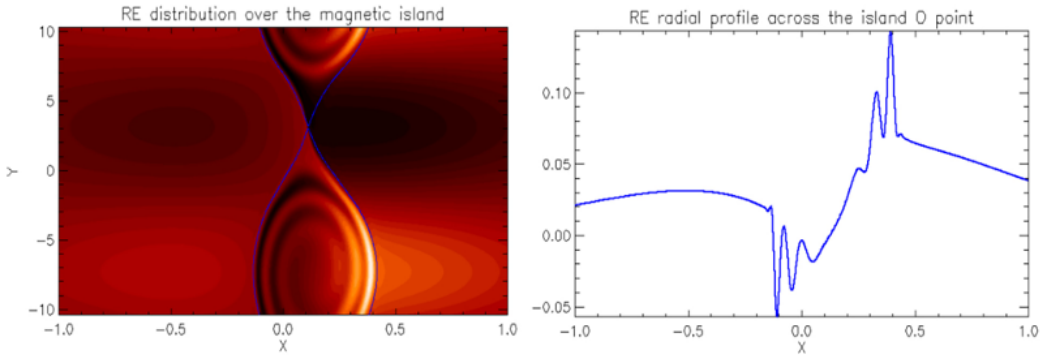


Fig. 5.11 Perturbed RE current distribution with the corresponding magnetic island (blue line) during the nonlinear phase (left) and RE radial profile (right) at t=2500 across the island $O-$point for $\eta = 1 \times 10^{-4}$, $c/v_A = 1$ and $\Delta' = 6.057$, $d_e = 0$, $\rho_s = 0$. Reproduced from [7].

The spiral-like structure disappears as the magnetic island reaches the saturation stage. During this phase, the rotation of the poloidal island slows down and eventually stops, as shown in Fig. 5.12 with the time evolution of the island's X-point position (green line). The displacement predicted by the dispersion relation (3.38) (blue curve) aligns with the simulation results in the linear growth phase of the island, but deviates once the system transitions to the nonlinear phase. Due to plasma resistivity, the small scales are removed, and it tends to equalize j_{RE} within the island. Furthermore, a slight displacement along the x-direction (rust line) is observed in the nonlinear regime. It tends to shift the island X-point towards the centre of the domain $x = 0$, which has been previously observed in simulations of asymmetric magnetic reconnection [97].

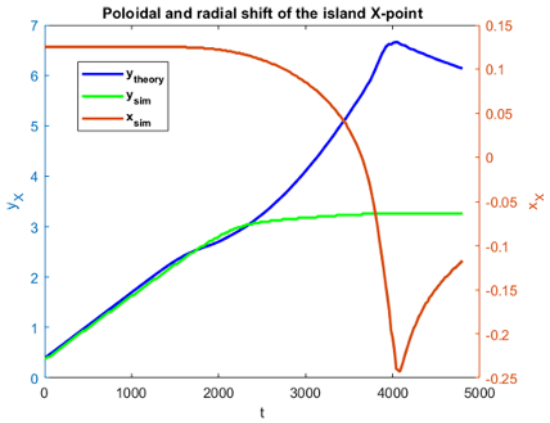


Fig. 5.12 Temporal evolution of the X-point position of the magnetic island in a purely resistive case with $\eta = 1 \times 10^{-4}$, $c/v_A = 1$ and $\Delta' = 6.057$, $d_e = 0$, $\rho_s = 0$. The green line shows the numerical poloidal shift (y_{sim}) while the blue line corresponds to the theoretical prediction (y_{theory}) according to the formula (3.38). The rust line represents the displacement along the x direction. Reproduced from [7].

When the island width at saturation was examined with a value of $\Delta' = 6$, it was discovered that the presence of a RE current did not result in a 50% increase in the saturated island width compared to the width in the absence of runaways, as observed in Fig. 5.2. A comparison of simulations with and without runaways revealed that when $\Delta' > 3$, the saturated island width in both cases was similar in size. This is due to a different nonlinear evolution of the island, as evidenced by the temporal evolution of ψ'_x in Fig. 5.13. The growth of ψ'_x, which closely approximates the island growth even in the nonlinear phase, is more pronounced without RE, as shown in the left panel of Fig. 5.13 where the temporal evolution of ψ'_x without RE (blue curve) and with RE (rust curve) is depicted. This burst in the island growth is characteristic of the case without RE and compensates for the 50% larger island observed in the presence of RE.

The burst in the island growth is caused by the transition to a different regime with increasing Δ'. In this regime, an X-point-collapse leads to a Sweet-Parker-like current sheet, a dynamic characteristic of the transition to a fast reconnection regime, as explained in [98]. This change results in a magnetic island at saturation without RE that is similar in size to the island with RE, as shown in the right panel of Fig. 5.13. For completeness, the same plots are also shown for the case $\Delta' = 3$ in Fig. 5.14. In this case, the nonlinear evolution of ψ'_x characteristic of the small Δ' regime is observed and the magnetic island width at saturation is approximately 50% higher

in the presence of RE compared to the case without RE, as predicted by the theory in [3].

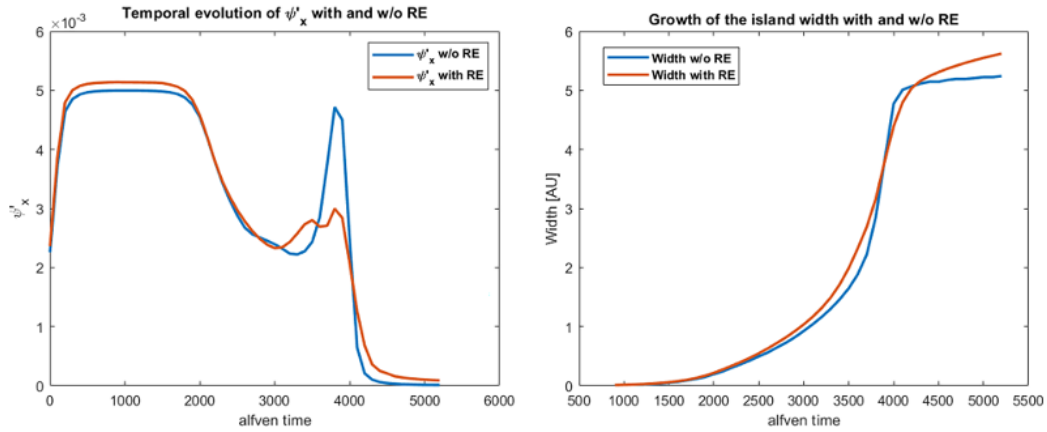


Fig. 5.13 Temporal evolution of ψ'_X w/o (blue curve) and with RE (rust curve) at the left panel and temporal evolution of island area w/o (blue curve) and with RE (rust curve) at the right panel for a purely resistive case with $\eta = 1e-4$, $c/v_A = 1$ and $\Delta' = 6.057$. Reproduced from [7].

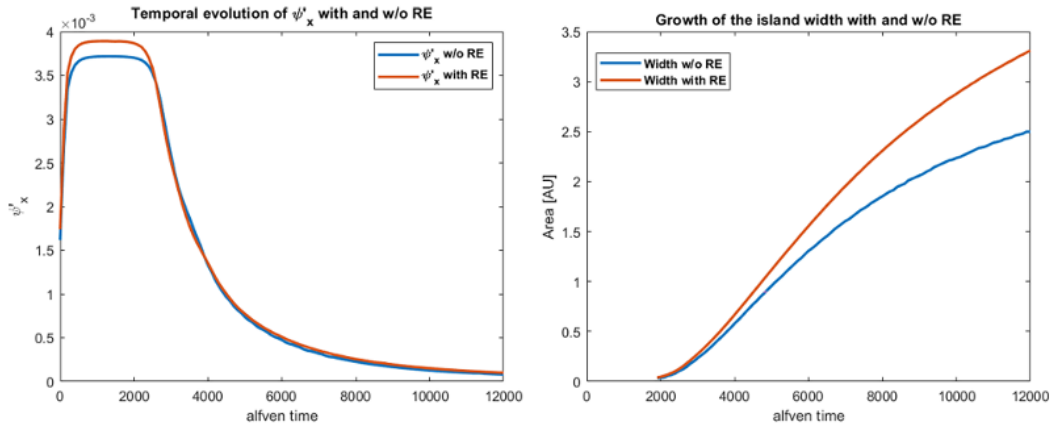


Fig. 5.14 Temporal evolution of ψ'_X w/o (blue curve) and with RE (rust curve) at the left panel and temporal evolution of island area w/o (blue curve) and with RE (rust curve) at the right panel for a purely resistive case with $\eta = 1e-4$, $c/v_A = 1$ and $\Delta' = 3$. Reproduced from [7].

When considering the nonlinear effects of electron inertia, the most significant change compared to the purely resistive regime is observed in the thermal current density. This change manifests as the development of small-scale patterns within the magnetic island, resembling a spiral structure centered at the O-point of the magnetic

island, similar to what occurs in the resistive case with runaways. In Fig. 5.15, the contour of the thermal current density demonstrates this spiral formation (left) and the profiles of the same quantity across the magnetic island for different values of d_e are shown in the right panel. For larger values of d_e, the amplitude of the small-scale oscillations inside the island increases. A detailed description of these dynamics in the highly nonlinear phase would require higher numerical resolution, which is deferred to future work.

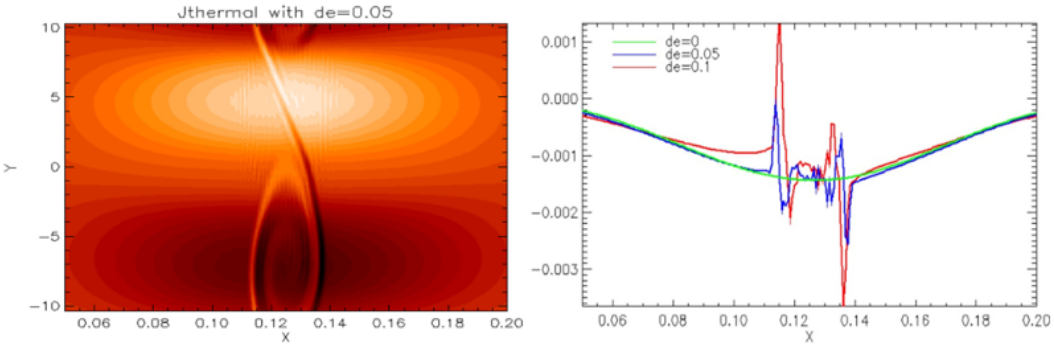


Fig. 5.15 Thermal electron current distribution over the magnetic island with $d_e = 0.05$ (left) and thermal electron radial profile across the island O-point at $d_e = 0$ (green), $d_e = 0.05$ (blue) and $d_e = 0.1$ (red) (right) for $\eta = 1e-4$, $c/v_A = 10$ and $\Delta' = 6.057$. Reproduced from [7].

5.3 Comparison between SCOPE3D and JOREK

In this work, SCOPE3D and JOREK are used to study the mutual influence between a RE current and tearing mode instabilities. Both codes are characterized by features that allow the investigation of specific aspects of the same problem. However, they differ in their implementation and simulation phases. Moreover, the first code was used in a slab geometry and single helicity regime (single magnetic island). This means that the equations are used in cartesian coordinates. On the other hand, JOREK was mainly used with a toroidal geometry in a multiple helicity regime (multiple magnetic islands), and the equations were implemented in toroidal coordinates. The relations between the toroidal (R,Z,ϕ) and cartesian coordinates (x,y,z) are $x = R\cos\phi$, $y = R\sin\phi$ and $z = Z$.

In SCOPE3D, the user provides the starting current equilibrium profile in analytical form, whereas in JOREK, the same profile is computed using the GS equation.

The GS equation can use analytical expressions or numerical values for the p' and FF' profiles and outputs the current profile. Once the equilibrium is defined, in SCOPE3D, the simulations are started with small perturbations on the modes of interest, e.g. (1,1), (1,2). In contrast, JOREK is initially run in axisymmetric mode to find the steady state, and after that, the toroidal harmonics of interest are initialized with small perturbations.

A significant difference between the two codes is that in SCOPE3D, in the multiple helicity regime, the user does not impose an upper limit to the toroidal harmonics to simulate. The upper limit is given by the number of grid points, nz, along the z direction, with $nz/4$ being the highest mode simulated. During the simulations, any mode can be generated through the coupling of the already existing modes. In JOREK, the user is supposed to define a finite set of toroidal harmonics to evolve, and higher toroidal modes are cut to make the simulation computationally feasible. Instead, the number of poloidal modes involved in both codes depends on the poloidal resolution.

In addition, in SCOPE3D, the RE kinetic energy is conserved throughout the simulation. It is impossible to define a computational domain where the loss of RE current can be investigated. Consequently, the code cannot study the effect of magnetic stochastization on the termination of RE. In this framework, JOREK represents the optimal code for these studies.

Since the two codes are structured differently (the numerical methods are described in sections 4.1 and 4.2.), a verification exercise was carried out with JOREK. This exercise studied the interaction between a RE current and a $(2,1)$ tearing mode to verify the linear growth rates and the magnetic island width at saturation. The FF' and p' were chosen to have a $q = 1.15(1 + r^2/0.61)$ profile which gives a $B_z = A\tanh(r/a)$ where r is the plasma minor radius. The adopted q profile is the same used in Ref. [4], whose results were reproduced using SCOPE3D.

Regarding the linear evolution, the scaling law as a function of the resistivity was verified in JOREK, and the results agree with the theory as shown in Fig. 5.16. The scaling law is derived from the FKR dispersion relation valid in the presence of RE, as seen in section 3.4.1.

For the magnetic island width at saturation, a comparison between the islands without (left panel) and with (right panel) is shown in Fig. 5.17. The width of the island in the absence of RE is $w = 0.104$, and in the presence of RE, is $w = 0.193$.

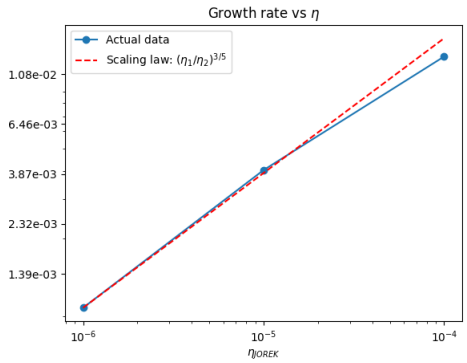


Fig. 5.16 Comparison between the scaling law and the numerical growth rates as a function of the resistivity. The resistivity interval is $[1 \times 10^{-4}, 1 \times 10^{-6}]$

The difference is higher than the 50% predicted by the theory. However, as seen in Fig. 5.2, for $\Delta' > 1$, the numerical width diverges from the theoretical prediction. In this case, $\Delta' \approx 3$

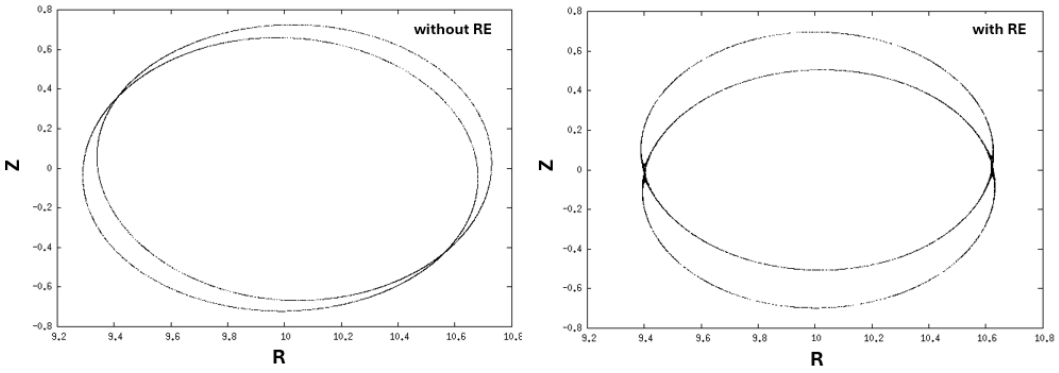


Fig. 5.17 Comparison between the islands without (left panel) and with (right panel) with $\eta = 1 \times 10^{-5}$.

5.4 Conclusions

In this part of the study, we looked at the stability of a post-disruption plasma in a symmetric and asymmetric configuration (equivalent to a cylindrical geometry). In the former case, the peak of the current radial profile is at the same location as the resonant surface. Whereas, in the latter case, the configuration is characterized by a mismatch between the current peak and the resonant surface. Like in the RE plateau phase, here, all the equilibrium plasma current is assumed to be carried by the RE

and the analysis is done through SCOPE3D which solves Eq. 3.27-3.30 in a 2D slab geometry. In addition to the purely resistive case, only the effect of the electron temperature was considered for the symmetric case. In contrast, in the asymmetric case, only the effect of the electron inertia was added to the purely resistive treatment of the problem.

We have confirmed the linear results on the growth rate of a reconnecting mode driven by an RE current in a symmetric configuration by adopting a new non-periodic equilibrium magnetic configuration. We have also verified the saturation width amplitude found in Ref. [3] up to values of the stability parameter of order 1, allowing the magnetic island to grow all the way to saturation in the small regime. Considering the electron temperature effects, we have found no substantial difference between the growth rate with and without RE. The saturation width amplitude is insensitive to the microphysics related to the ion sound Larmour radius, and the formula in Ref. [3] for the island saturation width is also valid in this regime.

In the asymmetric configuration, the RE do not change the linear growth of the island consistently with the symmetric case. However, they cause the island to rotate in the poloidal direction, as indicated in the analytical results presented in [4]. A notable difference in the asymmetric simulations is the presence of a microlayer on the RE current profile, which is much smaller than the resistive layer. It was observed that while the resistive layer governs the island transition from the linear to the nonlinear stage, the microlayer width causes the runaways to become nonlinear once the island size exceeds the microlayer width. This RE transition to the nonlinear phase gives rise to a spiral-like structure inside the island, altering the distribution of runaways compared to the symmetric case. Additionally, as the microlayer widths are comparable in size to the electron skin depths measured in a post-disruptive scenario, the effect of the presence of d_e during the linear evolution of the island was investigated. The study revealed that a Gaussian layer no longer accurately characterizes the thermal electron distribution in the presence of d_e, and an oscillatory distortion occurs in the magnetic island region.

The analysis in the resistive regime shows that the frequency does not follow the evolution of the equilibrium runaway current once this becomes nonlinear and tends to zero when the island reaches saturation. As long as we are consistent with a small Δ' regime, the island width at saturation is 50% larger than the corresponding island without runaways, which is consistent with the theory [3]. At higher Δ' ($\Delta' \geq 6$), the

magnetic island saturation width in the presence of RE becomes more similar in size to the width in the absence of RE. In this case, the rapid burst in the nonlinear island growth in the absence of RE, due to a Sweet-Parker-like current sheet, compensates for the 50% higher saturation width with RE.

The theoretically predicted linear growth rates and a higher magnetic island width were also reproduced with JOREK with a magnetic equilibrium of Harris type.

In the non-linear regime, the presence of electron inertia effects causes a concentration of thermal electron current in thin, spiralling structures within the magnetic island, similar to the RE population. In the case of weakly resistive plasmas with more realistic RE speed, such structures may influence the overall evolution of the system due to the introduction of strong gradients. However, an accurate description of this behaviour requires an extremely refined spatial resolution, which is the next step in this study.

The results obtained in this study highlight the importance of investigating the stability of a post-disruptive plasma in the presence of a RE current. Moreover, as demonstrated in section 3.3, in the presence of more than one helicity, the magnetic field undergoes a chaotic evolution. This magnetic stochasticity has a benign effect on the mitigation of the runaway current itself, as seen in section 3.4.2. Therefore, higher growth of the magnetic island during the nonlinear evolution of the system may significantly affect the evolution of the magnetic stochasticity in the presence of RE with direct consequences on RE population growth. These aspects of the RE-driven magnetic reconnection will be addressed in a future study.

Chapter 6

Runaway electron benign termination modelling in JET pulse 95135

The modelling of the RE benign termination observed in JET pulse 95135 has been carried out in Ref. [5], where the authors demonstrated the benign effect of the magnetic stochasticity on the RE loss. This numerical work used the nonlinear MHD code JOREK (described in section 4.2).

As described in section 3.4.2, the magnetic field stochastization was initiated by the interaction between magnetic islands with different poloidal mode numbers at the plasma edge. Afterwards, this stochasticity moves inward, leading to a core shrinkage caused by the generation of instabilities with high poloidal numbers.

The study in Ref. [5] used diffusion as the RE transport mechanism instead of advection. The choice of the diffusion process was given by the enormous computational time required by the fully advective simulations. At the same time, it has been demonstrated in Ref. [99] that the radial outward transport of RE caused by a stochastic magnetic field can also be modelled accurately through appropriate parallel and perpendicular RE diffusion coefficients. This is because during magnetic field stochasticity, the radial location of the field lines evolves diffusively, and the RE moving along these lines will also undergo a radial diffusion. Consequently, an advective or diffusive motion of RE moving along the filed lines causes the same physical radial diffusion of RE. However, recent developments in the JOREK RE module made using the advection process possible.

In addition, in Ref. [5], a fixed resistivity corresponding to a 10 eV plasma was assumed. However, this might be larger than the real value due to the recombination following massive deuterium injection. Therefore, in this work, different resistivity values were considered to investigate the influence of this plasma parameter on the system dynamics and RE advection was used to simulate RE transport.

The simulation setup and the inputs are reported in section 6.1. The results of the simulations are shown in section 6.2, and conclusions follow in section 6.3.

6.1 Simulation setup

The equilibrium current profile is obtained through the solution of the Grad-Shafranov equation (Eq. 4.12) by providing FF' and pressure profiles that give a hollow current profile as in Ref. [5]. The equilibrium current (red) and safety factor (blue)profiles given by the GS equation are shown in the left panel of Fig. 6.1. As can be observed in the figure, the q profile presents two $m = 4$ (DTM), two $m = 5$ rational surfaces responsible for the generation of magnetic stochasticity reported in section 3.4.2. The computational domain coloured by the normalized RE density number is presented in the right panel of Fig. 6.1. The hollow RE current profile obtained through the SOFT synthetic diagnostic is visible in the figure.

The interaction of RE with the plasma MHD activity is investigated through Eq. 3.39-3.42. Only the RE advection is considered in the RE density equation 3.41 while the diffusion coefficients are set to low values for numerical stability. The input parameters are summarized in Table 6.1. The resistivity values adopted are $\eta = 6.1 \times 10^{-4}\ \Omega m$, $\eta = 1.84 \times 10^{-4}\ \Omega m$, $\eta = 3.3 \times 10^{-5}\ \Omega m$ and $\eta = 6.1 \times 10^{-6}\ \Omega m$. If the Spitzer resistivity is considered, these correspond to temperatures of $T = 1.42$ eV, $T = 3.18$ eV, $T = 10$ eV and $T = 30$ eV, respectively.

6.2 Results

As seen in chapter 5, the plasma background resistivity influences the growth of the MHD modes. Consequently, it influences the evolution of the magnetic field stochasticity as described in section 3.3.2, which causes the RE loss. Before analyzing the nonlinear phase responsible for the magnetic chaos, the linear growth rates of the

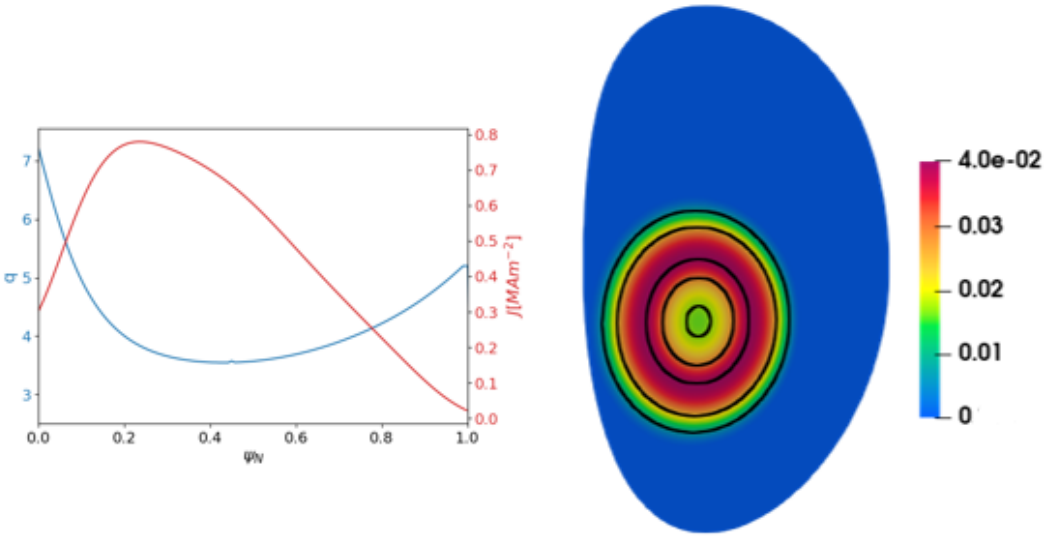


Fig. 6.1 Left panel: Current (red) and q (blue) profiles as a function of normalized poloidal flux ψ_N. Rightpanel: Simulations computational domain coloured by the normalized RE density number.

I_p	0.82 MA
B_0	3.49 T
n_e	1e19 m^{-3}
η	6.1 $\times 10^{-4}$, 1.84 $\times 10^{-4}$, 3.3 $\times 10^{-5}$, 6.1 $\times 10^{-6}$ Ωm
μ	1.6e-6 $kgm^{-1}s^{-1}$
$D_{r,\|\|}$	500 $m^2 s^{-1}$
n	0,...,5

Table 6.1 Simulations input parameters

$n = 1$, $\gamma_{numerical}$, are verified with the theory. A good agreement is found between $\gamma_{numerical}$ (blue curve) and the FKR scaling law (red dashed curve), as shown in Fig. 6.2.

The evolution of the RE current for the different resistivities is shown in Fig. 6.3.

As can be observed, the crash of the RE current occurs at a certain time which is determined by the pace of the plasma MHD activity evolution at various resistivities. Once the RE crash occurs, the duration of the current loss phase is governed by the resistivity. That is, apart from the lowest value (magenta curve), a higher resistivity value leads to a shorter loss phase and a lower amplitude of the current at the end of

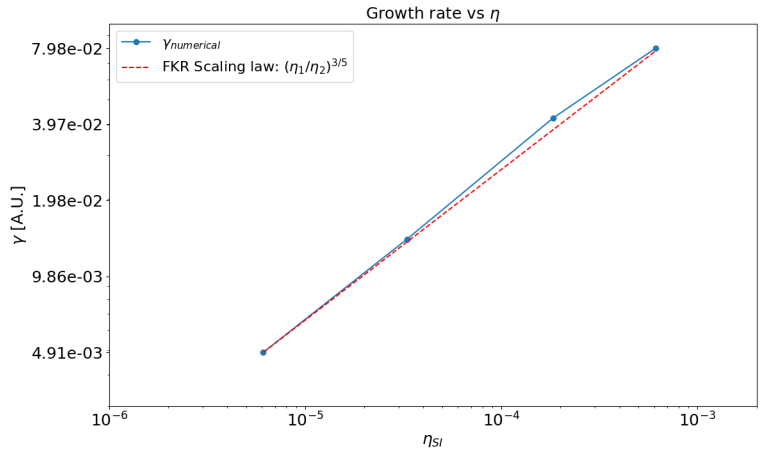


Fig. 6.2 Comparison between the numerical growth rates $\gamma_{numerical}$ (blue curve) and the FKR scaling law (red dashed curve).

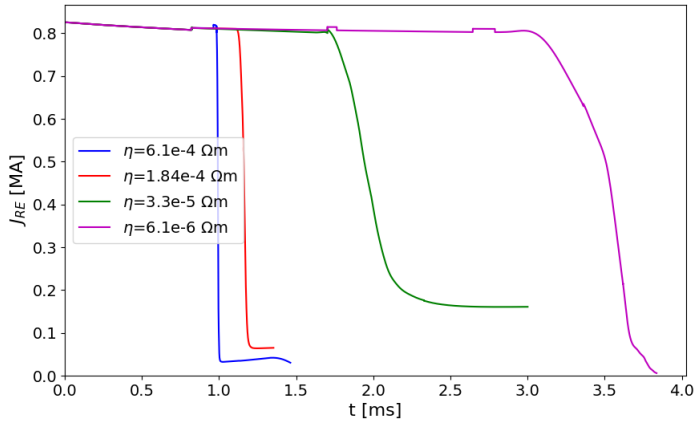


Fig. 6.3 Temporal evolution of the RE current amplitude with $\eta = 6.1 \times 10^{-4}$ Ωm (blue), $\eta = 1.84 \times 10^{-4}$ Ωm (red), $\eta = 3.3 \times 10^{-5}$ Ωm (green) and $\eta = 6.1 \times 10^{-6}$ Ωm (magenta).

the loss phase. The reasons for the different dynamics at the lowest resistivity case are explained in the following.

In Fig. 6.4, the toroidal modes $n = 1,...,5$ magnetic energies growth during the nonlinear phase are compared at different resistivities. The vertical dashed line underlines the start of the nonlinear phase, which is taken as a reference for the comparison of the different dynamics occurring in the various cases. In all cases, the dominant mode is the $(m,n) = (4,1)$ double tearing mode (DTM), whose evolution triggers the growth of the secondary modes starting from $n = 2$ until saturation.

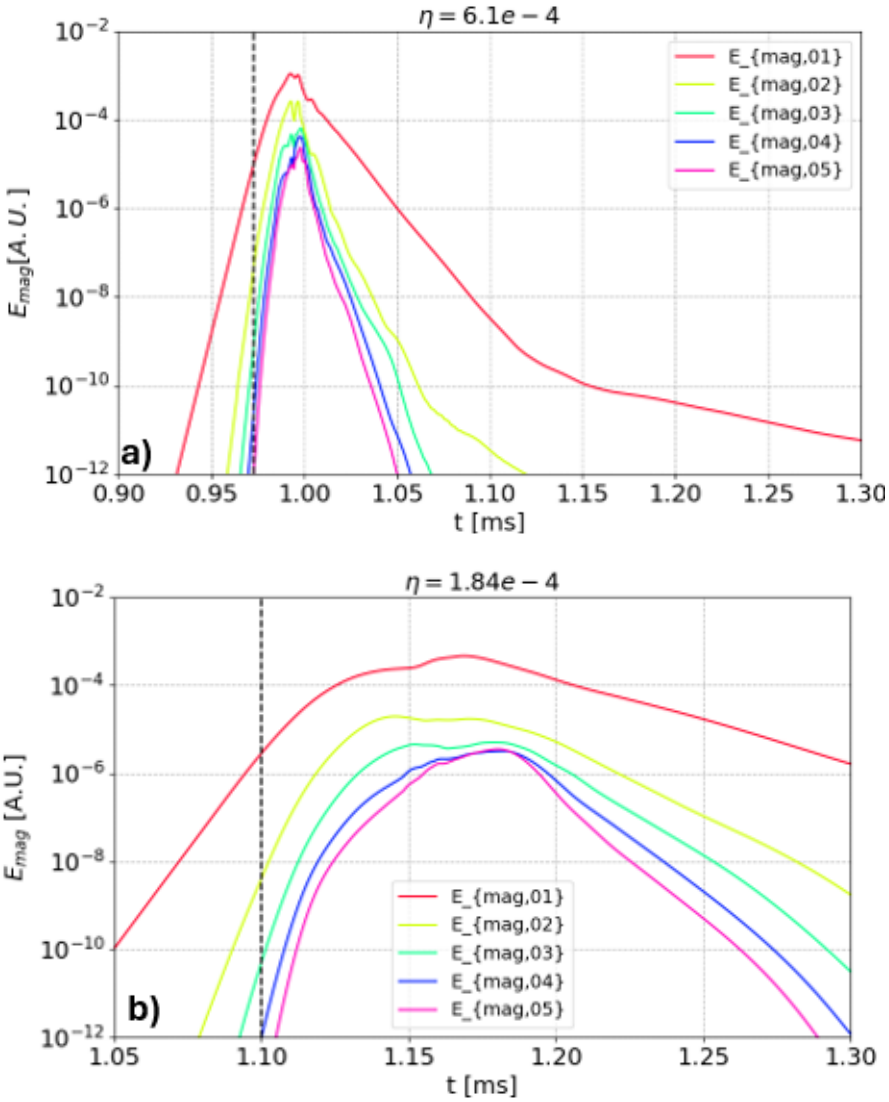


Fig. 6.4 Temporal evolution of the $n = 1$ (red), $n = 2$ (yellow), $n = 3$ (cyan), $n = 4$ (blue) and $n = 5$ (magenta) magnetic energy for a) $\eta = 6.1 \times 10^{-4}$ Ωm and b) $\eta = 1.84 \times 10^{-4}$ Ωm. The vertical dashed line underlines the start of the nonlinear phase.

A high resistivity results in stronger growth of the dominant mode. This can be observed by comparing the peaks of the magnetic energy growth of the modes in different cases in Fig. 6.4. As a consequence, the peak of the $n = 1$ magnetic energy governs the dynamics of the RE loss phase, as shown in Fig. 6.5 where the magenta and the green dashed vertical lines underline the start and the end of the RE loss phase, respectively. A stronger peak of the $n = 1$ E_{mag} (blue curve) leads to a weaker final RE current amplitude (red curve), as can be observed by comparing frames

a) ($J_{RE,end} = 0.03$ MA) with c) ($J_{RE,end} = 0.193$ MA). In addition, a more gentle nonlinear phase causes a higher duration of the RE loss phase, with the RE loss phase reaching its end when the peak region is crossed, as observed by comparing frames a) ($\Delta t_{RE,loss} \approx 20\mu s$) with b) ($\Delta t_{RE,loss} \approx 80\mu s$) and c) ($\Delta t_{RE,loss} \approx 550\mu s$). The duration of the loss phase is computed as the difference between the time points of the dashed vertical lines.

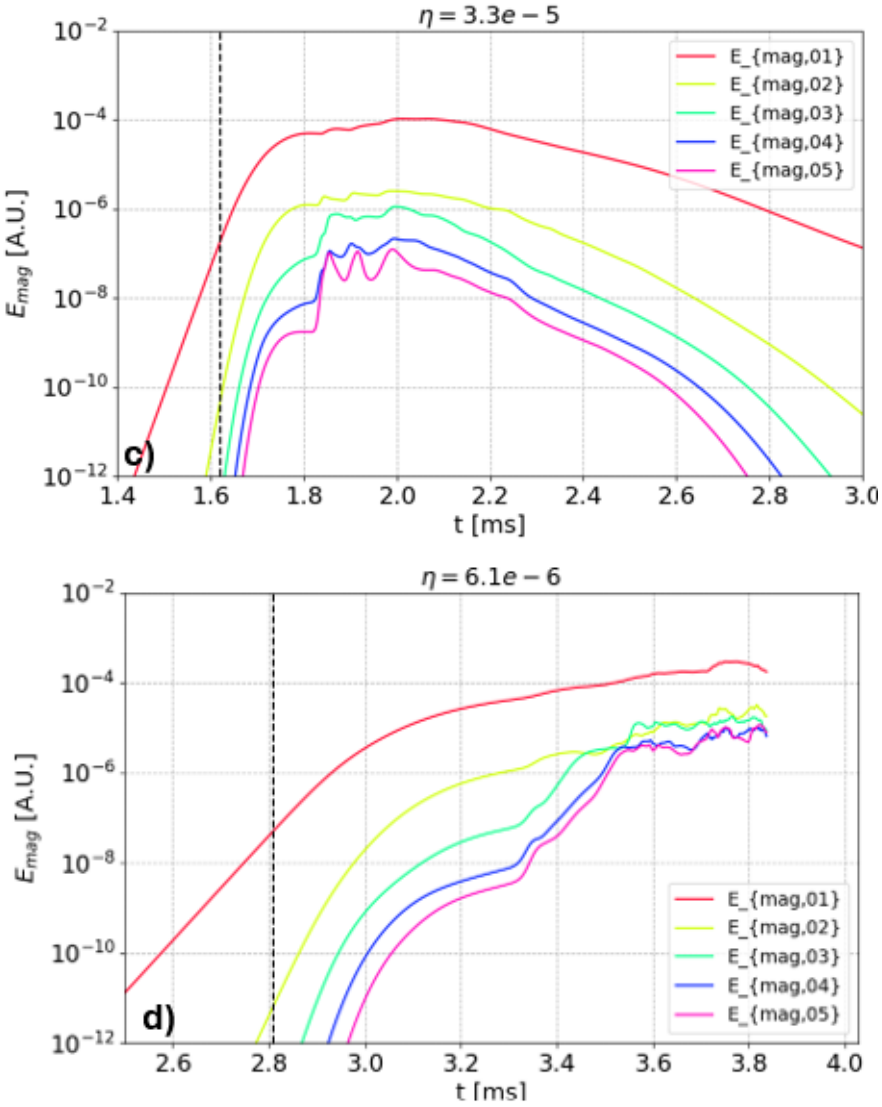


Fig. 6.4 Temporal evolution of the $n = 1$ (red), $n = 2$ (yellow), $n = 3$ (cyan), $n = 4$ (blue) and $n = 5$ (magenta) magnetic energy for c) $\eta = 3.3 \times 10^{-5}$ Ωm and d) $\eta = 6.1 \times 10^{-6}$ Ωm. The vertical dashed line underlines the start of the nonlinear phase.

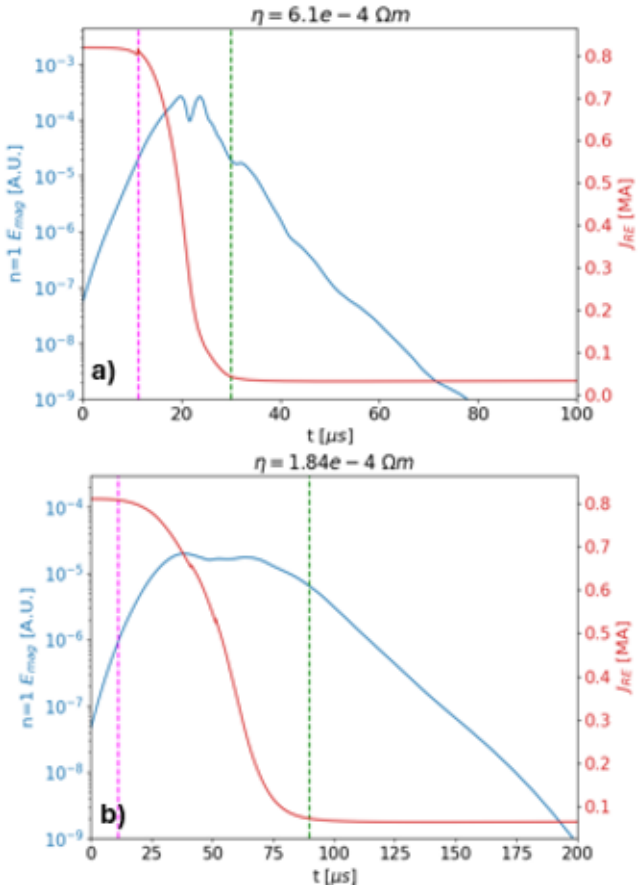


Fig. 6.5 Temporal evolution of the $n = 1$ E_{mag} (blue curve) and RE current amplitude (red curve) with a) $\eta = 6.1 \times 10^{-4}$ Ωm and b) $\eta = 1.84 \times 10^{-4}$ Ωm. The magenta and green vertical dashed line underlines the RE loss phase start and end.

The RE loss dynamics differ in the lowest resistivity, frame d) of Fig. 6.5. Indeed, at the end of the RE loss phase, the RE current amplitude is the lowest of all the cases. Moreover, a change in the slope of the loss phase occurs around ($t = 500\mu s$), which reduces the total duration of the phase. This time point corresponds to $t = 3.3ms$ in frame d) of Fig. **??** at which a sudden burst of the plasma MHD activity occurs, causing a further increase of the toroidal modes magnetic energies E_{mag} and leading to a lower RE current amplitude at the end.

In this section, the RE losses observed at different resistivities were correlated with the growth of the dominant mode. In particular, a higher resistivity leads to a stronger growth of the dominant mode resulting in a shorter duration of the RE current loss event.

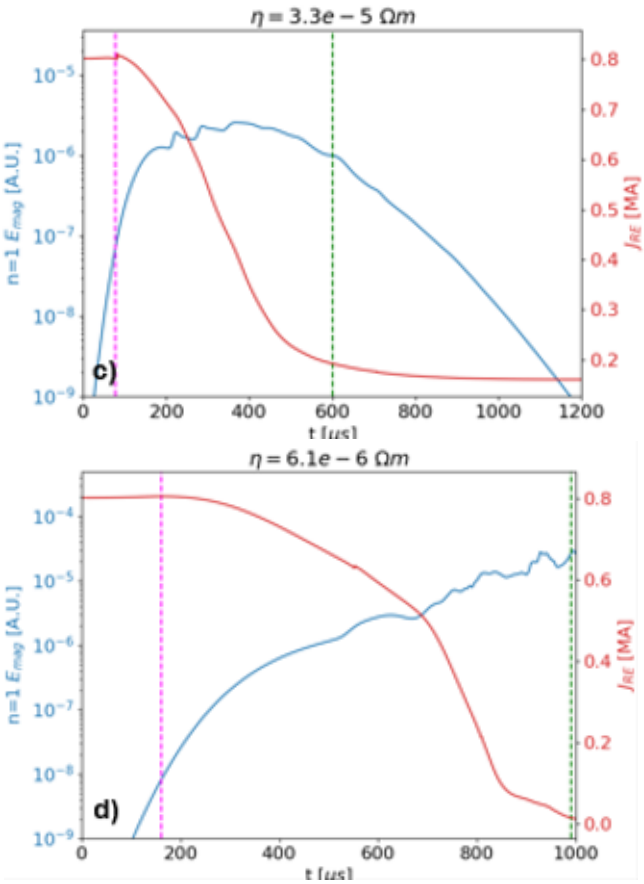


Fig. 6.5 Temporal evolution of the $n = 1$ E_{mag} (blue curve) and RE current amplitude (red curve) with c) $\eta = 3.3 \times 10^{-5}$ Ωm and d) $\eta = 6.1 \times 10^{-6}$ Ωm. The magenta and green vertical dashed line underlines the RE loss phase start and end.

The RE loss observed in Fig. 6.3 and 6.5 are caused by the nonlinear interaction between the dominant and secondary modes. Indeed, this interaction triggers the evolution of magnetic field stochasticity, whose intensity depends on the resistivity. The intensity of the magnetic stochasticity is measured through the magnetic field lines connection length presented in subsection 6.2.3.

The role of this nonlinear interaction in causing RE current loss in the two higher resistivity cases is investigated in subsection 6.2.1. Whereas, in subsection 6.2.2, first a comparison between results with $\eta = 3.3 \times 10^{-5}$ Ωm $\eta = 6.1 \times 10^{-4}$ Ωm is carried out and then the differences between the two lower resistivities are described.

6.2.1 Comparison between the two higher resistivity cases

The evolution of the stochasticity for $\eta = 6.1 \times 10^{-4}$ Ωm is shown in Fig. 6.6, starting from the nonlinear phase occurring at $t = 0.973$ ms taken as reference. In particular, at $t = 0$ μs (panel a), two $m = 4$ magnetic island chains appear at a radial location corresponding to $q = 4$ in the right frame of Fig. 6.1. At $t = 13$ μs (panel b), the plasma edge becomes stochastic due to the interaction between the outer $m = 4$ and $m = 5$ (not visible in the figure) magnetic island chains. Afterwards, the stochasticity moves inward through the evolution of secondary islands with high poloidal mode numbers ($m = 5$ in panel b and $m = 6$ in panel c). In the end, the reformation of the magnetic flux surfaces occurs. This strong plasma stochastization leads to the rapid loss of RE current.

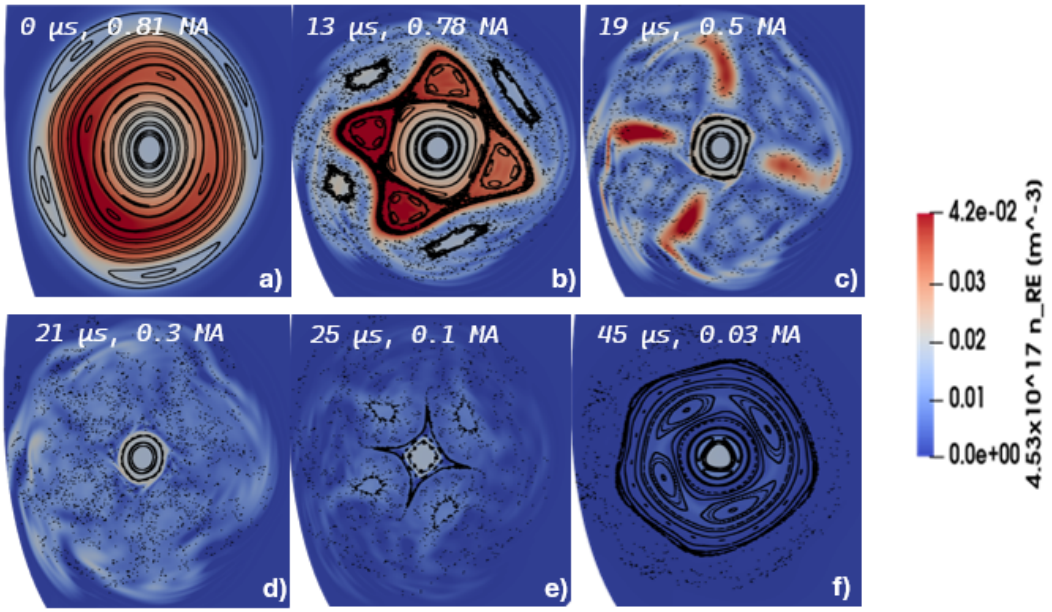


Fig. 6.6 Poincaré cross sections at different time points for $\eta = 6.1 \times 10^{-4}$ Ωm showing magnetic island formation, magnetic field stochastization and the reformation of the magnetic flux surfaces. The cross sections are coloured by the RE density and the RE current amplitude is also shown at different time points a) t=0 μs, b) 13 μs, c) 19 μs, d) 21 μs, e) 25 μs and f) 45 μs ($t = 0.973$ ms is taken as reference).

A lower value of the $n = 1$ E_{mag} for $\eta = 1.84 \times 10^{-4}$ Ωm leads to a lower stochasticity. Indeed, the plasma core is characterized by a lower level of stochastization as shown in Fig. 6.7. As in the $\eta = 6.1 \times 10^{-4}$ Ωm case, the plasma becomes stochastic at the edge in frame b) where the $m = 5$ and $m = 4$ islands chains interact. However,

the pace and degree of the stochastization are lower due to the weaker growth of $n = 1$ E_{mag}. Consequently, for the entire duration of the RE loss phase, the inner chain of $m = 4$ islands shows a weaker interaction with secondary islands ($m = 5$ in frame b) and $m = 6$ in frame d)) and is not entirely broken. The remanents are visible up to the time point shown in frame e) and are characterized by a high concentration of n_{RE} as these magnetic structures slow down the loss of RE as reported in section 3.4.2. Therefore, the amount of RE current lost is lower than $\eta = 6.1 \times 10^{-4}$.

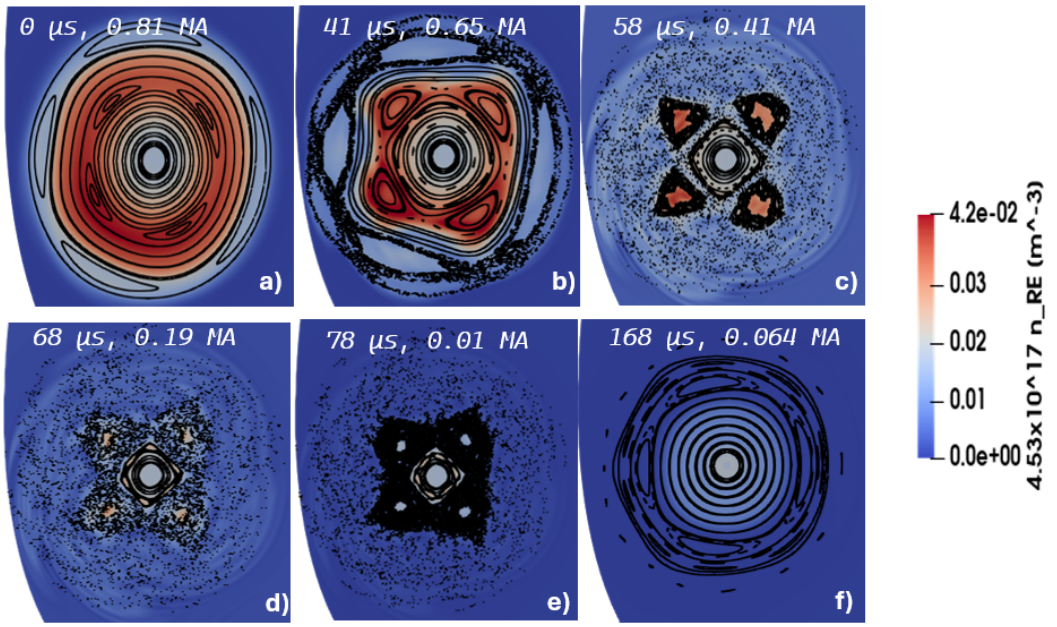


Fig. 6.7 Poincaré cross sections at different time points for $\eta = 1.84 \times 10^{-4}$ Ωm showing magnetic island formation, magnetic field stochastization and the reformation of the magnetic flux surfaces. The cross sections are coloured by the RE density and the RE current amplitude is also shown at different time points a) t=0 μs, b) 41 μs, c) 58 μs, d) 68 μs, e) 78 μs and f) 168 μs ($t = 1.1$ ms is taken as reference).

The difference between the level of stochasticity seen in the two cases is related to the growth of the dominant mode. This is because the secondary modes play a marginal role in the evolution of magnetic stochasticity with $\eta > 6 \times 10^{-5}$ Ωm, as demonstrated in Ref. [64]. In the paper, the authors have demonstrated that the secondary modes are less important in the evolution of magnetic stochasticity above this threshold. An evidence of this is reported in subsection 6.2.2.

A high resistivity leads to stronger growth of the dominant mode, which causes a global magnetic reconnection event. An evidence of the global magnetic reconnection event occurring with $\eta = 6.1 \times 10^{-4}$ is given by the flattening of the current

profile [100] shown in the left panel of Fig. 6.8 at $t = 21\ \mu s$. The figure shows the temporal evolution of the total current (left frame) and safety factor (right frame) profiles at different time points, taking the start of the nonlinear phase as the starting time point. Moreover, the inward shift of the current profile peak and the formation of high shear in the q profile over time leads to the core shrinkage observed in Fig. 6.6 due to the interaction of instabilities with high poloidal mode numbers with the inner $m = 4$ magnetic island chain which now have rational surfaces close to each other.

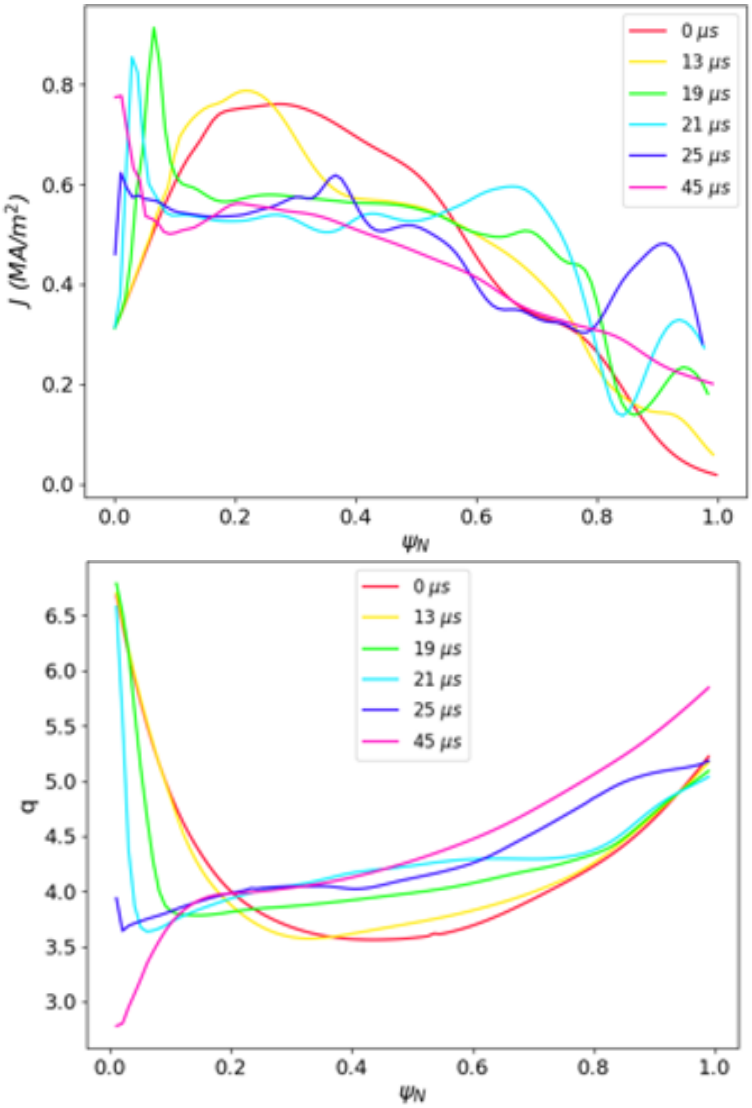


Fig. 6.8 Temporal evolution of the total current (top) and q profile (bottom) as a function of ψ_N for $\eta = 6.1 \times 10^{-4}\ \Omega m$

With $\eta = 1.84 \times 10^{-4}$ Ωm, the primary mode is characterized by a weaker growth. As a consequence, the $(4,1)$ inner chain does not grow enough to interact with (6,1) as shown in the frame e) of Fig. 6.7. This correlates with the absence of strong gradients on the current and q profiles as depicted in Fig. 6.9.

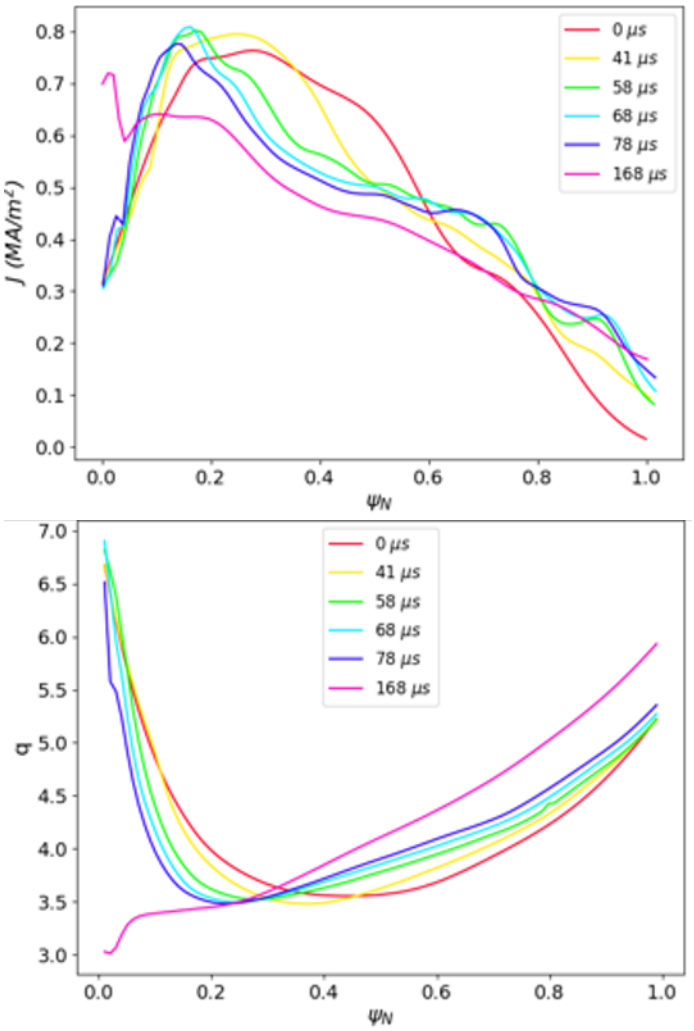


Fig. 6.9 Temporal evolution of the total current (top) and q profile (bottom) as a function of ψ_N for $\eta = 1.84 \times 10^{-4}$ Ωm

6.2.2 Comparison between the two lower resistivities cases

At high resistivity values, the dominant mode drives the stochasticity, whereas the secondary instabilities play a marginal role, consistent with the findings of Ref.

[64] described in subsection 3.3.2. At lower resistivities, however, the secondary instabilities become important.

The difference between the behaviour of the secondary modes at high and low resistivity can be appreciated by comparing Fig. 6.10 with Fig. 6.11. In Fig. 6.10, the growth of the magnetic energies in toroidal harmonics for $\eta = 6.1 \times 10^{-4}\ \Omega m$ (dashed curves) and $\eta = 1.84 \times 10^{-4}\ \Omega m$ (dash-dotted curves) are presented. The same mode is shown with the same colour in the two cases. The growth of the toroidal harmonics for the latter resistivity is plotted as a function of a rescaled time $t' = t/3.3 + 0.64\ ms$ where factor 3.3 comes from the resistivity ratio. The rescaling leads to a similar evolution for all the toroidal harmonics during the Rutherford phase. This is consistent with the theory as the dynamics during the Rutherford phase should be invariant by a transformation of the type $t \to \alpha t$, $\eta \to \eta/\alpha$ [64].

With $\eta = 6.1 \times 10^{-6}\ \Omega m$, the growth of the magnetic energies (plain curves) for the secondary modes is stronger than what is observed with $\eta = 1.84 \times 10^{-4}$ Ωm (dash-dotted curves), as shown in Fig. 6.11 where the magnetic energies of the toroidal modes are compared. The same mode is shown with the same colour in the two cases. even if the Rutherford phase (the slow algebraic non-linear phase) for the $n = 1$ is similar. In the figure, the growth for the lower resistivity is rescaled in the Rutherford-like way with $t' = t/30 + 1\ ms$. As a consequence, the secondary modes $n > 1$ grow earlier and faster for $\eta = 6.1 \times 10^{-6}\ \Omega m$. Similar dynamics are also observed in Fig. 3.5 where the secondary modes with $\eta = 6.1 \times 10^{-6}\ \Omega m$ (corresponding to a normalized $\eta = 1 \times 10^{-6}$ in the figure) grows earlier and faster than with $\eta = 6.1 \times 10^{-5}\ \Omega m$ (corresponding to a normalized $\eta = 1 \times 10^{-5}$ in the figure).

As demonstrated in Ref. [64] and described in section 3.3, at lower resistivities, the relative growth of the secondary mode is faster with respect to the dominant mode. This has been shown to be valid for $2 \times 10^{-5}\ \Omega m \leq \eta \geq 3 \times 10^{-6}\ \Omega m$. In particular, the authors have shown that the $n = 1$ mode reaches the nonlinear regime earlier than the secondary modes and its growth scales like η, whereas the growth rate of the secondary modes scales like $\eta^{3/5}$ (still in the linear regime). Therefore, the relative growth of the secondary modes with respect to the primary is $\eta^{-2/5}$, which is more prominent at lower resistivities. As a consequence, the secondary modes drive magnetic stochasticity for $2 \times 10^{-5}\ \Omega m \leq \eta \geq 3 \times 10^{-6}\ \Omega m$. The resistivity value $\eta = 6.1 \times 10^{-6}\ \Omega m$ adopted in our study falls into this interval.

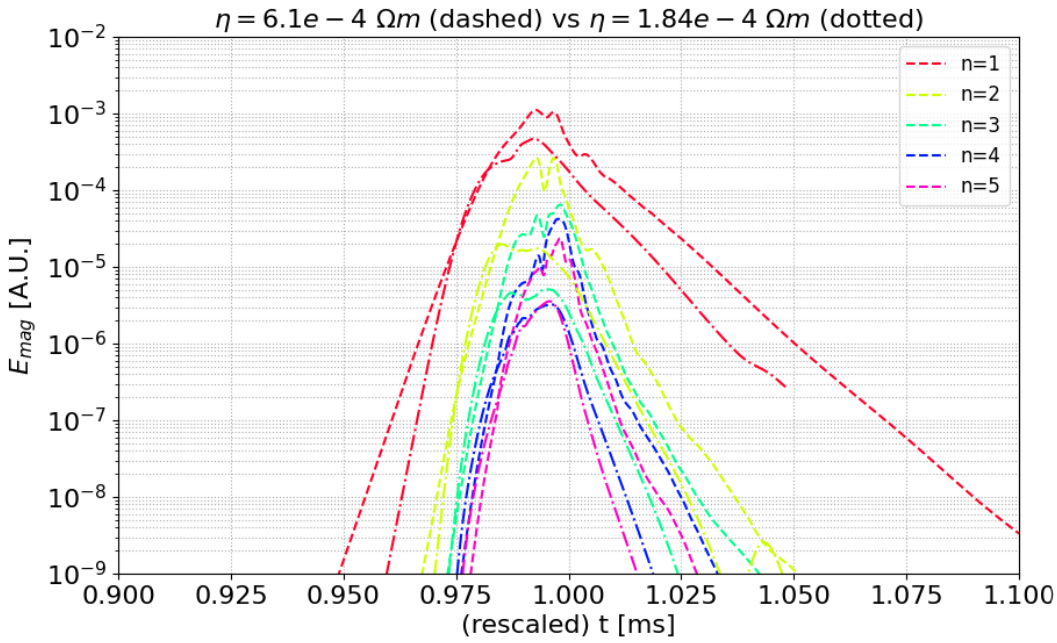


Fig. 6.10 Temporal evolution of the toroidal harmonics magnetic energy for $\eta = 6.1 \times 10^{-4}$ Ωm (dash curve) and $\eta = 1.84 \times 10^{-4}$ Ωm (dash-dotted curve). The time is rescaled, as explained in the text.

A resistivity value of $\eta = 3.3 \times 10^{-5}$ Ωm is lower than the threshold ($\eta = 6 \times 10^{-5}$ Ωm) above which the dominant mode is the main protagonist of the magnetic chaos. At the same time, it is outside the interval $2 \times 10^{-5} \leq \eta \geq 3 \times 10^{-6}$ in which the secondary modes drive magnetic stochasticity. Therefore, mixed dynamics are observed for this resistivity.

For $\eta = 3.3 \times 10^{-5}$ Ωm, the primary mode is characterised by a weak growth with respect to the higher resistivity value. The secondary instabilities (caused by $n > 1$), however, have enough time to grow with respect to the dominant mode $(4,1)$. This phenomenon is underlined in Fig. 6.12, where the Poincaré plots at different time points coloured with the RE density are shown. In frame b), a $m = 7$ island chain appears, which is not characterized by $n = 1$ toroidal mode number since a rational surface $(7,1)$ is not present in the q profile as shown in Fig. 6.13 at this time point. However, the growth of the secondary instability is not strong enough to interact with the dominant mode. Therefore, the overlap between the $m = 7$ and $(4,1)$ island chains does not take place, and only a local stochastic layer forms around the $m = 4$ inner island chain. Nevertheless, some of the RE population is lost from the plasma core due to the perturbation of the RE orbits caused by the presence

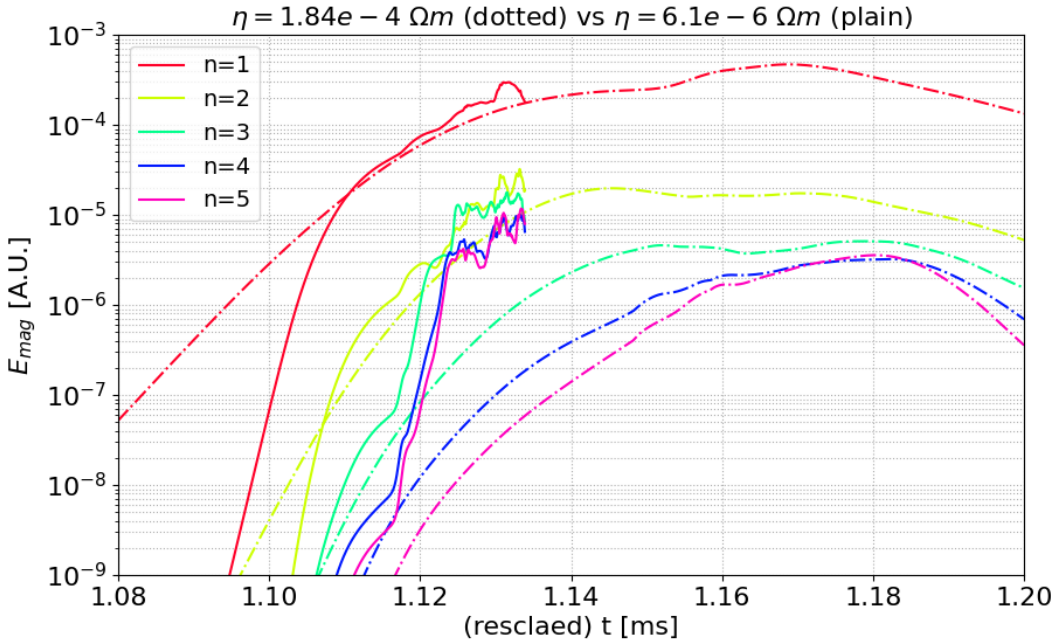


Fig. 6.11 Temporal evolution of the toroidal harmonics magnetic energy for $\eta = 1.84 \times 10^{-4}$ Ωm (dash-dotted curve) and $\eta = 6.1 \times 10^{-6}$ Ωm (plain curve). The time is rescaled as explained in the text.

of magnetic islands. In the end, the reformation of the flux surfaces occurs, and a $J_{RE} = 0.16\,MA$ is still present in the plasma.

In the lowest resistivity case, the growth of the secondary modes speeds up the dynamics and pushes the stochasticity further into the plasma core as shown in frame c) of Fig. 6.14. In the figure, the Poincaré plots at different time points coloured with the RE density are depicted. As in all cases, the plasma becomes stochastic at the edge due to the interaction between outer $m = 5$ and $m = 4$ island chains. In frame b), the $m = 7$ island chain appears as in the frame b) of Fig. 6.12. However, with a lower resistivity, the growth of the secondary instabilities is higher, and this causes the islands to reach a stage where the interaction between the various modes takes place, causing the core shrinkage as shown in frame f). As a consequence, almost no RE current survives in the plasma.

Comparing Fig. 6.12 with the results obtained by Bandaru et al. in [5] (. 3.9 in this thesis), significant differences were observed even if the simulations are carried out with the same resistivity. Moreover, Fig. 3.9 dynamics are similar to the highest resistivity case in this work (Fig. 6.6 with $\eta = 6.1 \times 10^{-4}$). Probably this is because the characteristic length of advection, $L_{adv} = \tau \cdot c = 1.3e4\ m$ with τ

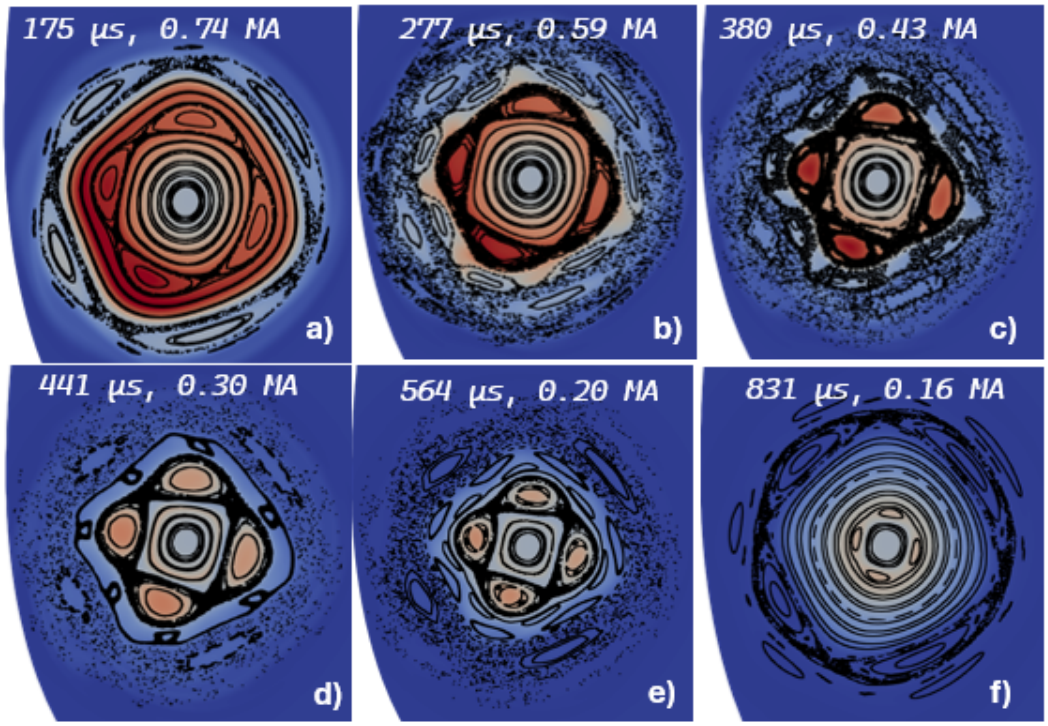


Fig. 6.12 Poincaré cross sections at different time points for $\eta = 3.3 \times 10^{-5}$ Ωm showing magnetic island formation, magnetic field stochastization and the reformation of the magnetic flux surfaces. The cross sections are coloured by the RE density and the RE current amplitude is also shown at different time points a) t=175 μs, b) 277 μs, c) 380 μs, d) 441 μs, e) 564 μs and f) 831 μs ($t = 1.6\,ms$ is taken as reference).

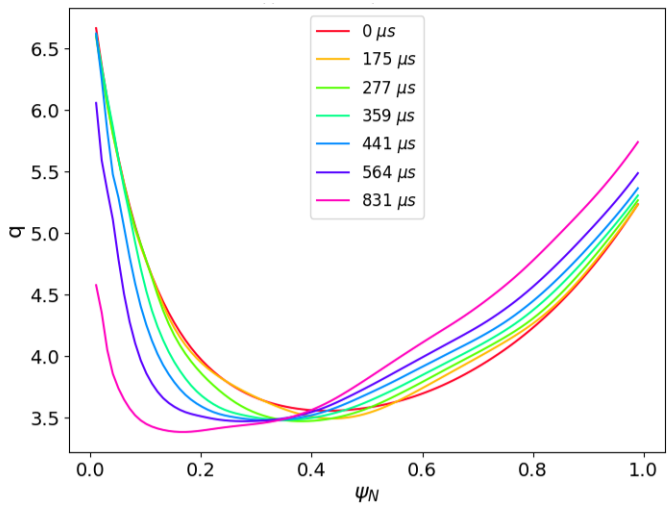


Fig. 6.13 Temporal evolution of the safety factor profile as a function of ψ_N for $\eta = 3.3 \times 10^{-5}$ Ωm

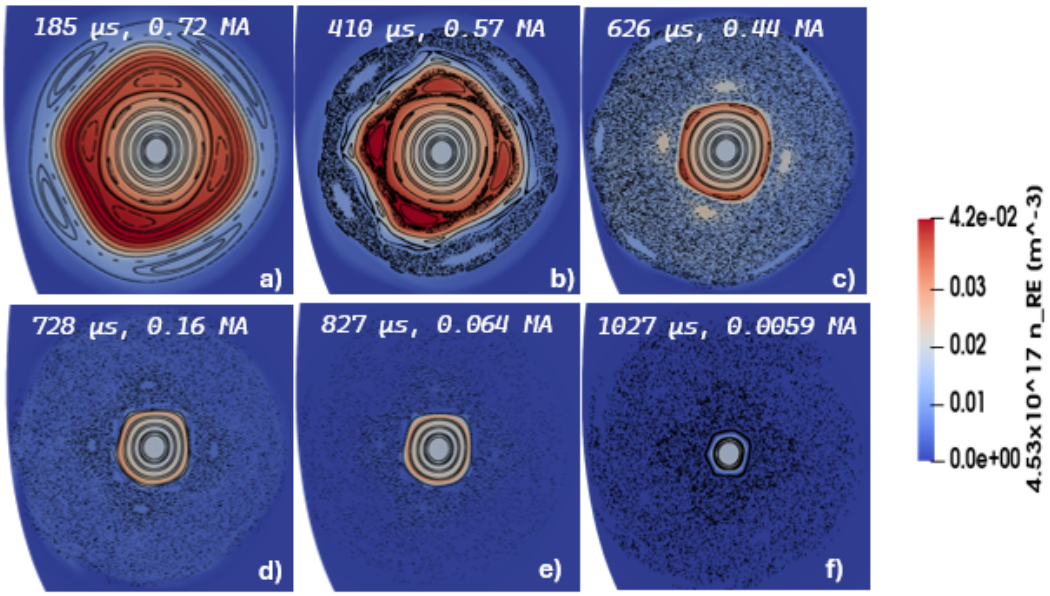


Fig. 6.14 Poincaré cross sections at different time points for $\eta = 6.1 \times 10^{-6}$ Ωm showing magnetic island formation, magnetic field stochastization and the reformation of the magnetic flux surfaces. The cross sections are coloured by the RE density and the RE current amplitude is also shown at different time points a) t=185 μs, b) 410 μs, c) 626 μs, d) 728 μs, e) 827 μs and f) 1027 μs ($t = 2.94$ ms is taken as reference).

being the duration of the nonlinear phase until the reformation of the magnetic flux surfaces and c speed of light, for $\eta = 6.1 \times 10^{-4}$ Ωm is similar to the characteristic length of diffusion, $L_{adv} = \sqrt{\tau \cdot D_{RE,\parallel}} = 1.3e3$ m, for the case present in Ref. [5]. Considering that, in our case, for $\eta = 3.3 \times 10^{-5}$ Ωm, $L_{adv} = 2.5e5$ m, L_{adv} is large enough that RE have the time to very significantly spread in the parallel and thus also radial directions over the timescale of evolution of the modes for the advective case. At the same time, this is not true for the diffusive case with L_{diff} two orders of magnitudes lower.

6.2.3 Heat loads

The level of stochastization reached in different resistivity cases is directly linked to the wall area on which the RE energy deposition occurs. The degree of chaos is quantitatively measured to compare the wall loads in the various cases and relate them to the plasma dynamics.

The chaos intensity is measured through the magnetic field line connection length. The connection length (CL) measures the distance a field line travels from the ψ_N location where it is initialized to the wall. A small CL value means the field line and the RE population travelling along it rapidly reaches the wall starting from a certain position. In Figures 6.15, 6.16, 6.17 and 6.18 the temporal evolution of the CL with $\eta = 6.1 \times 10^{-4}$, $\eta = 1.84 \times 10^{-4}$ $\eta = 3.3 \times 10^{-5}$ and $\eta = 6.1 \times 10^{-6}$ Ωm is reported. For the y-axis, the nonlinear phase starting time point is taken as reference ($t = 0$ μs). The CL for field lines initiated at different ψ_N is plotted as colour at each time point with an upper limit of 5 km. A dark shade means the CL is small. Some regions of the figures are white since the simulation results have been saved only for a few time points. Therefore, information about the CL is not reported for the entire interval considered.

In all cases, the CL values start to decrease first at the edge since the magnetic field becomes stochastic at the plasma edge, as pointed out in the Figures of the previous subsection. Once the edge becomes chaotic, the dynamics differ consistently from what was observed with the Poincaré cross-section. That is, the CL values rapidly decrease in Fig. 6.15 and around $t = 20$ μs also the plasma core becomes stochastic. This is consistent with the evolution of the stochasticity seen in the Poincarè plots for $\eta = 6.1 \times 10^{-4}$ Ωm. However, with $\eta = 1.84 \times 10^{-4}$ Ωm, the core experiences a mild stochastization.

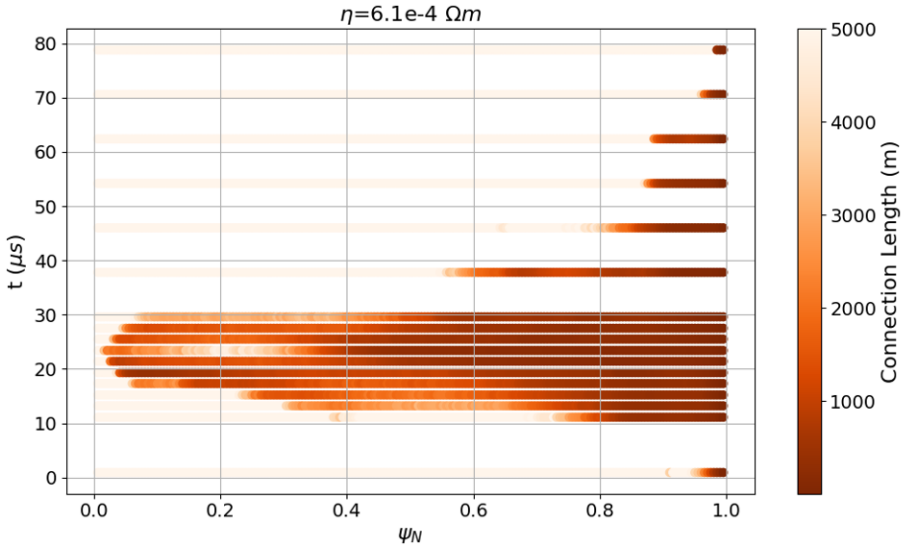


Fig. 6.15 Temporal evolution of the magnetic field lines connection length as a function of ψ_N for $\eta = 6.1 \times 10^{-4}$ Ωm

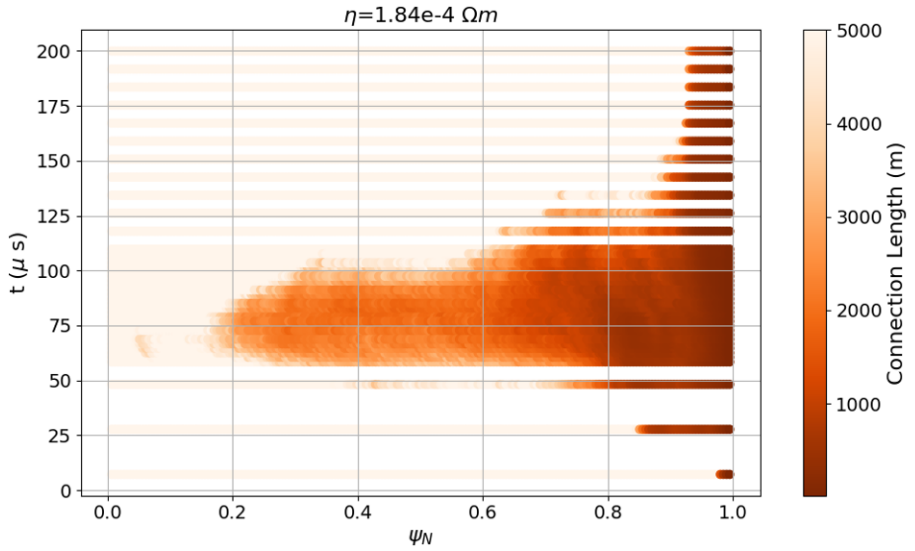


Fig. 6.16 Temporal evolution of the magnetic field lines connection length as a function of ψ_N for $\eta = 1.84 \times 10^{-4}$ Ωm

For $\eta = 3.3 \times 10^{-5}$ Ωm, weak growth of the dominant mode leads to localized magnetic field stochasticity. As represented in Fig. 6.17, the magnetic field becomes fully stochastic only at the edge.

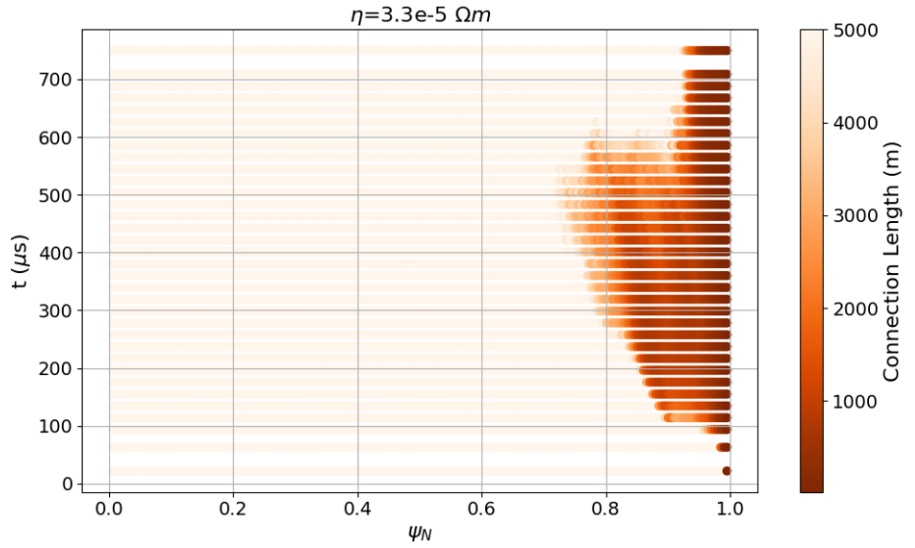


Fig. 6.17 Temporal evolution of the magnetic field lines connection length as a function of ψ_N for $\eta = 3.3 \times 10^{-5}$ Ωm

For $\eta = 6.1 \times 10^{-6}$ Ωm a violent stochastization take place as underlined in Fig. 6.18.

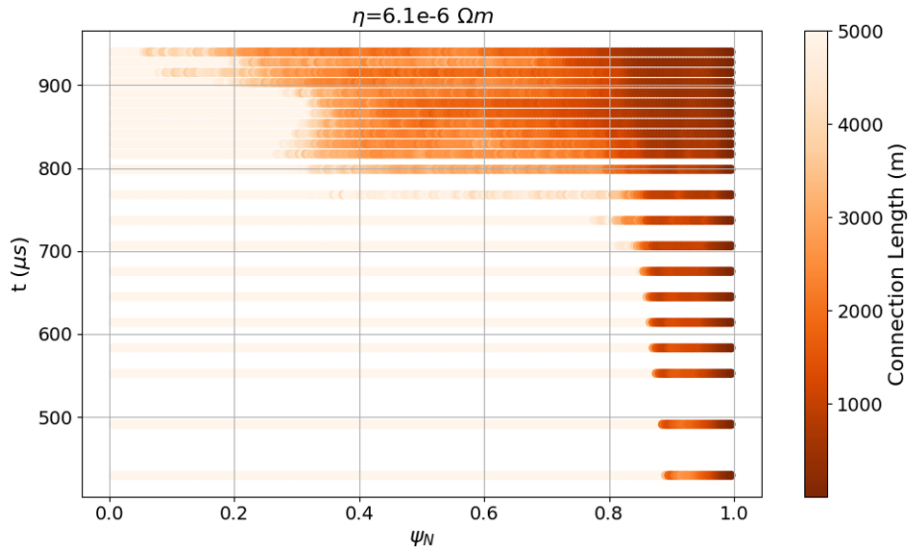


Fig. 6.18 Temporal evolution of the magnetic field lines connection length as a function of ψ_N for $\eta = 6.1 \times 10^{-6}$ Ωm

At $\eta = 6.1 \times 10^{-4}$ Ωm, the level of magnetic field stochasticity is high, and the duration of such an event is shorter (≈ 45 μs), as shown in Fig. 6.15. The duration of the stochastic phase is computed as the difference between the start of the nonlinear phase and the reformation of the magnetic fluxes in most of the plasma region. Therefore, a large amplitude of RE current (0.78 MA) is lost in a relatively small time interval. As the resistivity decreases, the chaos intensity gets weaker, but with a larger duration of the stochastic phase, $170\mu s$ with $\eta = 1.84 \times 10^{-4}$ Ωm and $831\mu s$ with $\eta = 3.3 \times 10^{-5}$ Ωm as depicted in Figures 6.16 and6.17. A low level of chaos leads to a weaker pace of the RE loss phase. However, due to a larger time interval, the amount of RE current lost does not significantly differ from the first case (0.75 MA and 0.66 MA for $\eta = 1.84 \times 10^{-4}$ Ωm and $\eta = 3.3 \times 10^{-5}$ Ωm, respectively).

With $\eta = 6.1 \times 10^{-6}$, the level of chaos is higher than with $\eta = 1.84 \times 10^{-4}$. However, the burst in plasma activity occurs when the amplitude of the runaway electron (RE) current still present in the plasma is 0.4 MA. In the end, almost all of the RE current is lost, with half lost due to weak stochastic effects and the other half due to strong chaotic behaviour.

The degree of chaos occurring during the RE loss phase strongly influences the wall area on which the RE energy is deposited. These heat loads are computed using

the JOREK particle tracing module first implemented in Ref. [101]. In particular, a test particle approach is used where these test particles or markers are not coupled with plasma MHD evolution. That is, the particles are evolved following the MHD dynamics of the plasma which, however, is not affected by the evolution of these markers.

Markers are sampled from the RE density obtained in the different fluid simulations. The markers are initialized at random spatial coordinates inside the computational domain that are sampled from the RE density number n_{RE} at a certain time point. The selected time point is the starting of the nonlinear phase in all the cases. All the markers are assigned the same weight, meaning each marker represents an equal number of physical particles. The weight is chosen so that the sum of all the markers equals the overall number of RE calculated from the fluid simulation, $N_{RE} = 2.65 \times 10^{17}$. The total number of markers selected for the tracing is $N_{markers} = 10^6$. Once initialized, the markers are traced through the solution of the guiding centre equations [102] using a Runge Kutta method (RK4).

The markers are traced until they are not lost to the wall or, if they are confined, until the end of the RE loss phase. Regarding the wall, an ideal wall corresponding to the computational domain boundary is chosen.

Since the MHD simulations provide no information about the RE distribution in the momentum space, each RE particle is assumed to have a kinetic energy of 10 MeV and a pitch angle of $\zeta = v_{\parallel}/v_{\perp} = -0.99$.

Fig. 6.19 shows the minimum heat loads resulting from the RE loss to the wall caused by the magnetic field stochasticity for a) $\eta = 6.1 \times 10^{-4}$, b) $\eta = 1.84 \times 10^{-4}$, c) $\eta = 3.3 \times 10^{-5}$ and d) $\eta = 6.1 \times 10^{-6}$. The frame a) characterized by the highest resistivity shows the largest area of deposition. In order to assess the deposition area, only the heat loads $> 10^3$ are considered since, below this threshold, the heat loads might be caused by the deconfinement of the markers already at the start of the tracing due to numerical artefacts. The deposition areas in the different cases are summarized in Tab. 6.2.

The widespread deposition seen in all cases is caused by the chaoticity that begins at the edge and then progresses inward. As a result, the outer region RE is lost first, followed by the release of RE from the core. If stochasticity only occurs in the core, RE deposition will only happen near the contact point between the plasma and the limiter, leading to smaller wetted areas.

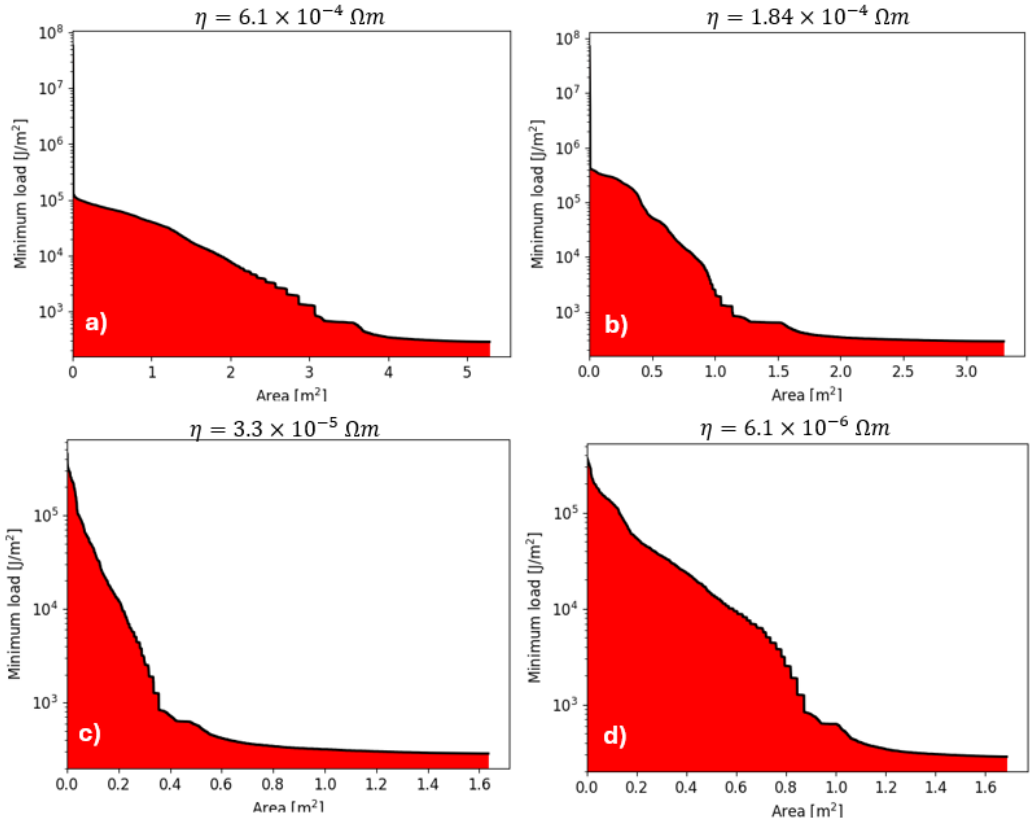


Fig. 6.19 Heat loads as a function of wall area for a) $\eta = 6.1 \times 10^{-4}\ \Omega m$, b) $\eta = 1.84 \times 10^{-4}\ \Omega m$, c) $\eta = 3.3 \times 10^{-5}\ \Omega m$ and d) $\eta = 6.1 \times 10^{-6}\ \Omega m$.

$\eta\,[\Omega m]$	A $[m^2]$
6.1×10^{-4}	3
1.84×10^{-4}	1.1
3.3×10^{-5}	0.35
6.1×10^{-6}	0.85

Table 6.2 RE energy deposition area as a function of the resistivity

In subsection 6.2.1, it was shown that the case with the highest resistivity (frame a in Fig. 6.19) exhibits the most chaotic evolution. This results in the largest area of energy deposition among all the simulated cases. As the resistivity decreases, the energy from the runaway electrons (RE) is deposited over a smaller area due to reduced stochastization. However, at the lowest resistivity, the deposition area is larger because of the violent MHD activity observed in the latter part of the RE energy loss phase.

In all cases, the amount of RE current lost to the wall is similar. In cases of high resistivity, the current is lost on a wetted area larger than in small resistivity cases. Therefore, the damage caused to the wall with high resistivity should be lower. Consequently, the colder the plasma (i.e., the higher the resistivity), the more benign the RE termination.

6.3 Conclusions

This study investigated the effect of the plasma background resistivity on the benign termination of RE observed in JET #95135. The RE termination is caused by the evolution of magnetic stochasticity driven by the interaction between the multiple magnetic islands, as observed in Ref. [5]. Such islands are a result of a hollow current profile resulting from the processing of the experiment data, as shown in the cited paper. In our investigation $\eta = 6.1 \times 10^{-4}$, $\eta = 1.84 \times 10^{-4}$, $\eta = 3.3 \times 10^{-5}$ and $\eta = 6.1 \times 10^{-6}$ Ωm resistivity values were used.

The results demonstrated the significant role of resistivity in the evolution of magnetic chaos causing the RE termination consistent with the findings of Ref. [64]. In particular, it was found that for resistivities $\geq 6 \times 10^{-5}$ Ωm, such evolution is governed by the growth of the dominant mode, which is the $(4,1)$ double tearing mode, whereas the secondary modes ($n > 1$) play only a marginal role. Indeed, a higher resistivity results in a more chaotic evolution of the plasma dynamics. This is because a higher resistivity leads to stronger growth of the dominant mode, as predicted by the FKR dispersion relation. Consequently, a strong core stochastization occurs, leading to a rapid loss of RE with a negligible amount of RE surviving in the plasma at the end of the stochastic phase. As the resistivity decreases, the stochastization becomes weaker, leading to a lower pace of the RE loss phase and a larger RE current at the end. However, the difference between the RE current amplitude is not dramatic due to the larger duration of the chaotic phase at lower resistivities.

In contrast, for resistivity below this threshold, the role of the secondary modes in the evolution of the stochasticity becomes fundamental. For $\eta = 6.1 \times 10^{-6}$, the stronger growth of the secondary modes with respect to the primary modes leads to a burst in the plasma stochasticity, accelerating the loss of RE. This results in a nearly complete loss of RE, which is not observed in the other cases. However, a

$\eta = 6.1 \times 10^{-6}$ is equivalent to a Spitzer resistivity with $T = 30\,eV$, which is far from the temperatures observed during a plasma disruption ($\sim 10\,eV$).

The impact of the RE loss from the plasma on the wall was computed through the JOREK particle tracing module. It was found that even if a similar RE current amplitude is lost from the plasma, the wetted area is quite different. Indeed, strong stochasticity results in a larger wetted area, which is more benign for the RE termination. This is because higher magnetic stochasticity leads to a higher radial diffusion of the magnetic field lines, causing an enlargement of the wetted area.

The study aims to investigate the benign termination strategy of the RE beam to effectively mitigate it. It demonstrates the role of resistivity in governing the evolution of stochasticity, which is a key aspect of this strategy. The next step involves analyzing the role of ion density and understanding the generation of a hollow current profile that leads to this evolution.

Chapter 7

Runaway electrons interaction with Plasma facing components

Disruptions-induced runaway electrons stand out among potential operational challenges for future fusion machines such as ITER and DEMO [103][104]. As seen in subsection 2.2.4, these electrons can deposit substantial energy within PFC, potentially compromising their structural integrity and inducing melting. Additionally, ITER recent decision to transition from Beryllium to Tungsten as the First Wall (FW) material carries implications for the interaction between the runaway electron beam and the material.

Several studies have numerically computed the damage induced by RE on PFC [104] [105]. Firstly, energy deposition (ED) profiles are generated using Monte Carlo codes such as FLUKA, introduced in section 4.3, and ENDEP, simulating the interaction between the RE beam and the material. These profiles serve as input for subsequent temperature evolution and erosion studies using tools like ANSYS and MEMOS-U. In our investigation, we have established a workflow utilizing FLUKA and FREEFEM++, described in section 4.4, to evaluate damage induced by realistic RE energy distribution functions [106]. This approach introduces a novel aspect to the work, as previous literature has primarily focused on either a monoenergetic beam or analytical energy distribution functions [104] [105].

The results from the FLUKA simulations are shown in section 7.1 where the energy deposition profiles obtained from the impact of a RE beam are shown. Firstly, a fixed impact angle was considered to analyze the influence of the different electron

transport mechanisms on the final energy deposition patterns. In particular, the effects of the delta ray production, Brehmsstrahlung and elastic scattering are studied. Afterwards, the parametric scan results demonstrate the significant dependence of the ED curves on the RE impact angle.

The analysis of the material thermal response to the RE impact is described in section 7.2, where the dependence of the material melting front and temperature temporal evolution on the RE current is studied as well. This part of the work was carried out in collaboration with a colleague from Politecnico di Torino.

7.1 Impact of Runaway electrons beam on First Wall tiles

A FLUKA simulation requires the definition of a geometry, a source, a grid resolution, and energy thresholds for electron and photon production transport.

The geometry consists of a tile representative of a Tokamak FW sample tile, measuring 10x10 cm along the toroidal (X) and poloidal (Y) directions and 3 cm thick in the radial (Z) direction. Two different tile materials were considered, which are Tungten (W) and Beryllium (Be).

The distributions utilized in this study are depicted in Fig. 7.1 for three distinct time steps. These energy distributions have been determined by deconvoluting the HXR energy spectrum [106]. Details about the numerical deconvolution technique can be found in Ref. [107]. The beam energy ranges from 5 to 10 MeV. Among the three energy distributions, the one corresponding to t=0.952 s (cyan) was selected to replicate the impact of a beam with the highest average electron energy E_{kin}=7.23 MeV.

Two different spatial distributions were considered for the RE beam that are a point beam and a square beam with an area of 10 cm^2. The point beam was chosen to concentrate the impact at a single point on the material surface. The focus here was to understand the effects of the different electron transport mechanisms. The square beam was selected for the thermal analysis since a point beam would have required an extremely high-resolution mesh near the point of impact, making the simulation unfeasible.

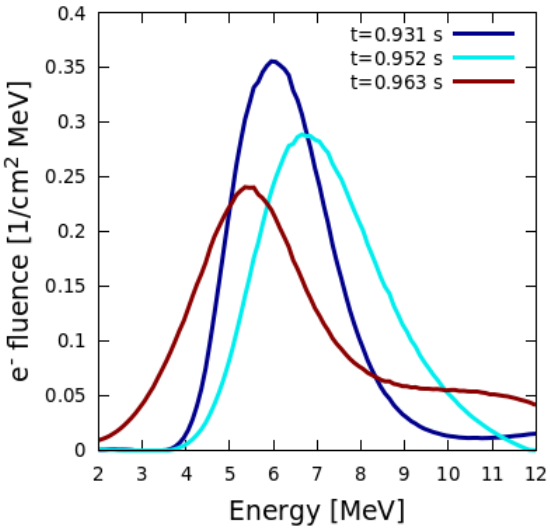


Fig. 7.1 RE energy distribution at t= 0.931s (blue), t=0.952s (cyan) and t=0.962s (red). Adapted from [8]

The beam impacts the tile at the centre of its surface, located at coordinates (X,Y,Z) = (5,5,0). An impact angle of 5 degrees was considered for the point and square beam. The results of this study are shown in subsection 7.1.1. However, in the point beam case, a parametric scan is also conducted to examine the effects of different impact angles within the range of (0,90) degrees on the ED profiles in Be and W and the results are reported in subsection 7.1.2. These impact angles are measured with respect to the tile surface along the toroidal direction as shown in Fig. 7.2.

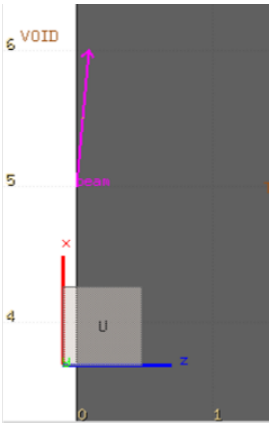


Fig. 7.2 2D representation of the tile geometry with the impact angle of the RE beam

To accurately measure the energy the RE deposits, the geometry has been divided into a spatial grid with bin dimensions of (X,Y,Z) = (0.02,0.02,0.006) cm. The grid resolution along the Z direction is lower than the CSDA range of 1e-2 cm, corresponding to the Beryllium 100 keV electron transport threshold. At the same time, it is comparable to the CSDA range of 1.6e-3 cm for Tungsten. Reducing the bin dimension for W along Z was impossible because the simulation became computationally unfeasible.

7.1.1 Fixed impact angle

An impact angle of 5 degrees was selected to compare the volumetric ED in Be and W. The 1D projection along the Z direction of the ED is shown in fig. 7.3. Without magnetic fields, a beam with an average energy of 7.23 MeV per electron deposits, 4.55 MeV per beam electron in Be(green), and 2.80 MeV in W (red), having an average statistical error below 3%. The remaining energy is carried by the electrons, which are scattered back from the material surface. Moreover, reducing the maximum fraction of energy to be lost in a single step to 5% causes a reduction of the deposited energy per electron of 2% only, which is negligible and allows to keep the default value of 20%.

The profiles combine the three electron transport mechanisms that take place in the energy range of interest: Bremsstrahlung and elastic scattering scaling as Z^2 and delta ray production (scaling as Z). Focusing on the near-surface region, photons generated through Bremsstrahlung make a negligible contribution to the deposited energy, whereas elastic scattering and delta-ray production play a major role. To describe how these mechanisms affect the ED profiles, the 2D projection of the ED density on the XZ plane is shown in Fig. 7.4, which depicts the ED for Be at the right panel and for W at the left panel for a beam impacting with an angle of 5 degrees. The deposited energy is reported in terms of MeV/cm^3 per primary by averaging over the third dimension Y.

Figures 7.3 and 7.4 illustrate that the deposition resulting from beam electrons is considerably more compact in W compared to Be, concentrating in the first few millimeters of the material. This is because the beam electrons experience significant attenuation in W compared to Be, leading to a reduction in energy by two orders of magnitude within the first 2 mm of material depth. This phenomenon is due to the

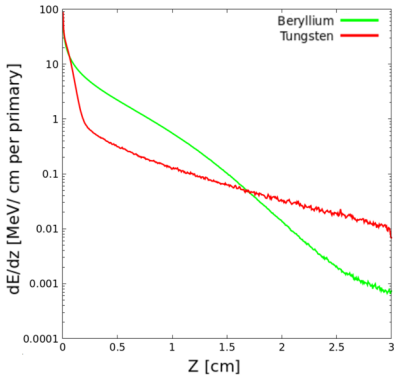


Fig. 7.3 1D projection of the ED along the Z direction for Be (green) and W (red) with a point beam impacting at (X,Y,Z)=(5,5,0) cm with 5 degrees impact angle with respect to the tile surface. Reproduced from [8]

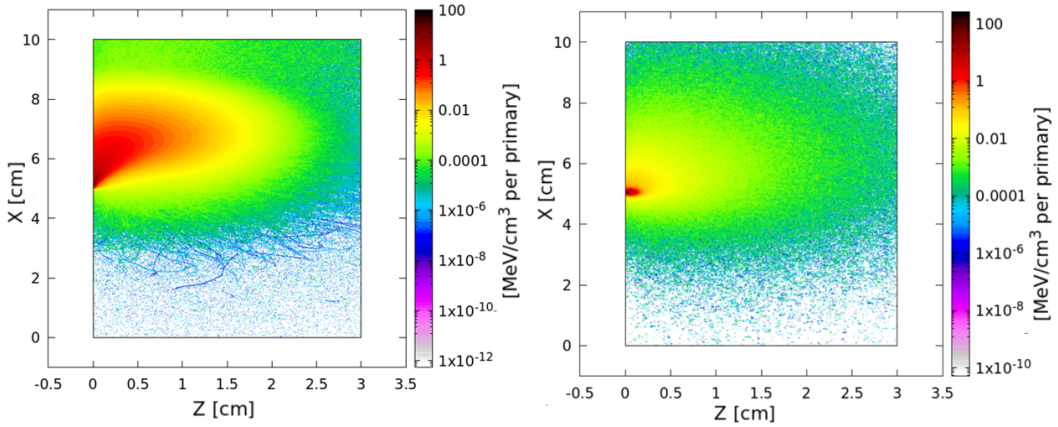


Fig. 7.4 2D projection of the ED on the XZ plane for Be at the left panel and W at the right panel with a point beam impacting at (X,Y,Z)=(5,5,0) cm with 5 degrees impact angle with respect to the X direction. Reproduced from [8]

high atomic number of W (Z=74) compared to Be (Z=4), making inelastic collisions more effective in the former material. Therefore, the RE beam decelerates rapidly in W and loses energy near the surface.

Another significant difference evident from Figure 7.4 is that the electron shower in Be penetrates deeper into the material before losing information about its initial direction, whereas in W, the shower acquires an isotropic angular distribution after the first 2 mm. This disparity arises from the dependency of elastic scattering on the Z^2 of the material, with elastic scattering being two orders of magnitude more effective in W ($74^2/4^2$) compared to Be.

In Figure 7.4, it is evident that W exhibits a higher peak value of deposited energy per beam electron than Be. However, the average energy deposited in W per primary electron is lower due to the higher likelihood of electron back-scattering into the vacuum resulting from numerous collisions with atomic electrons near the surface[104]. As illustrated in Figure 7.5 through the 2D projection of electron fluence in the XZ plane for Be (left) and W (right) in the vacuum region, the number of back-scattered electrons from the W surface is notably higher (with a maximum of approximately 1000 cm^{-2} per primary electron) compared to Be (maximum of 100 cm^{-2} per primary electron). These electrons, both primary and secondary, retain a considerable fraction of the initial beam electron energy. Similarly, the maximum number of photons reflected by the W surface is two orders of magnitude higher than in Be. However, these reflected particles would be redirected toward the surface in the presence of magnetic fields. Consequently, the area affected by the RE beam impact would be enlarged beyond the initial beam impact area.

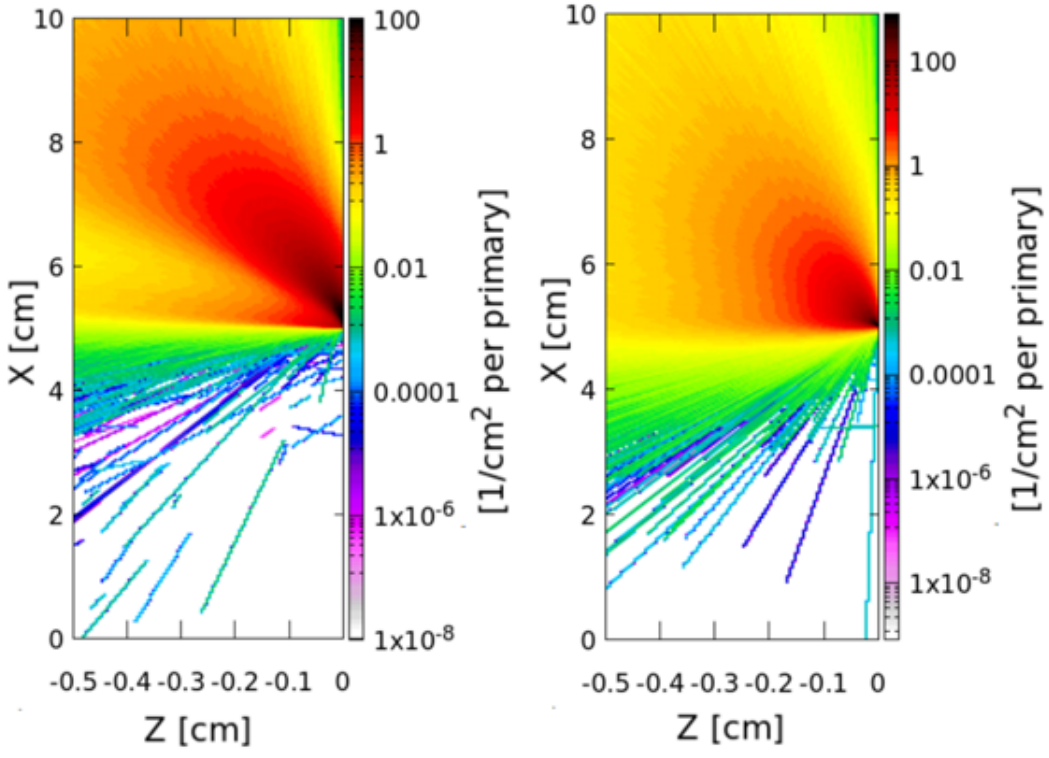


Fig. 7.5 2D projection of the electron fluence in the XZ plane for Be at left and W at right with an impact angle of 5° for both materials. Reproduced from Ref. [8]

While photons have a negligible influence on the energy deposition profiles near the impact surface, they become the primary energy carriers deeper in the material due to their high radiation length, as discussed in section 4.3. This is evident in Fig. 7.6 through the 1D projection of the ED profile in Be (left panel) and W (right panel) with default (blue) and high (red) photon production thresholds. The default photon production threshold in FLUKA is set to 33 keV [86]. That is, only the interaction of particles with energies above 33 keV can generate photons. However, a higher threshold of 1 GeV was imposed to investigate the energy deposition pattern of the beam in the absence of photon production. This is because no particle is assumed to have an energy of 1 GeV in this work, therefore, no photon is generated. In the case of Be, photons account for the tail of the energy deposition profile after 1.5 cm, where the deposited energies are lower than 10 keV/cm. Thus, Brehmsstrahlung does not significantly influence the impact of the RE beam on low Z materials. Conversely, in W, where electrons experience a rapid decrease, photons become the primary energy carriers after a few mm, where the deposited energy is still in the order of 1 MeV/cm for a RE beam with energy around 7 MeV per primary electron.

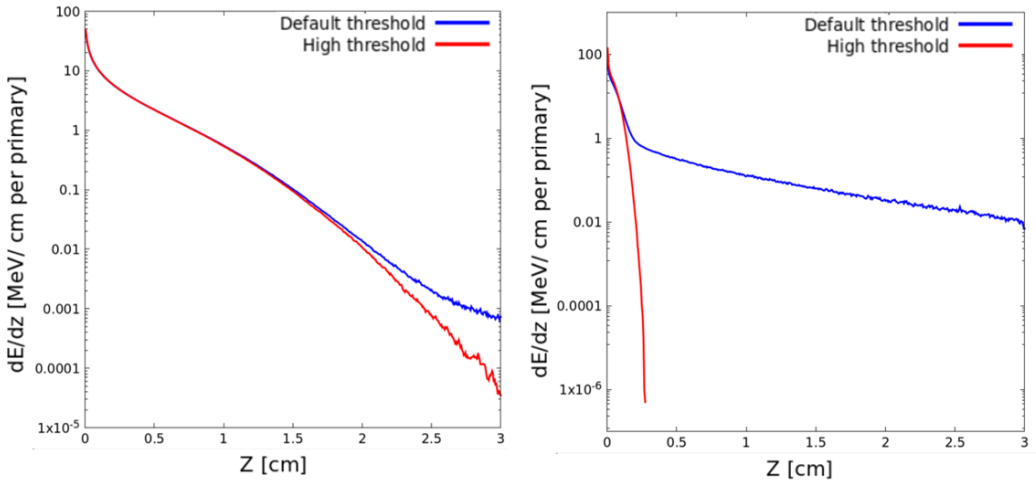


Fig. 7.6 1D projection of the ED in Be at the left panel and W at the right panel with default (blue) and high (red) photon threshold. Reproduced from [8]

The results obtained by considering the impact of a $10cm^2$ beam are similar to the case of a point beam. In particular, the 1D ED profiles and the deposited energy per beam particle are approximately the same for Be and W with the two beams. The primary difference lies in the intensity of energy deposition density, which is characterized by lower values in the case of a 10 cm^2 beam. This is because the

beam particles are distributed over a larger area than a point beam, and the energy deposition is less localized, as depicted in Figure 7.7.

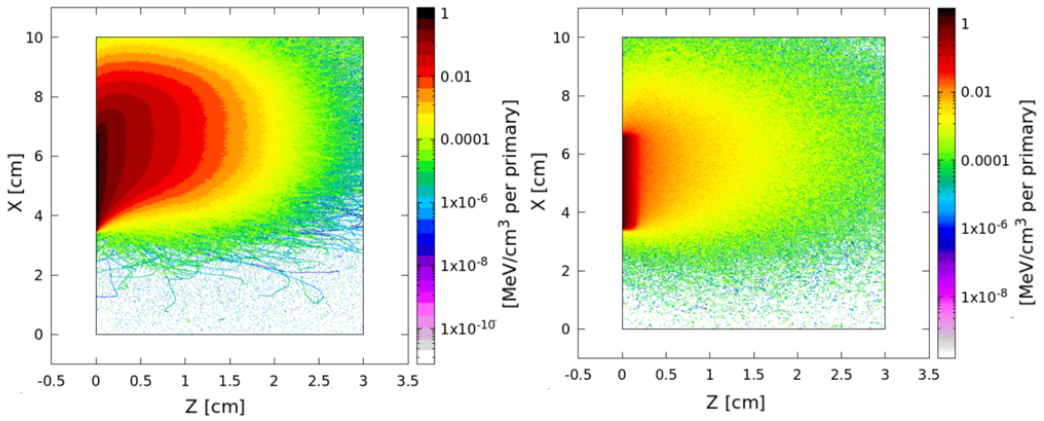


Fig. 7.7 2D projection of the ED on the XZ plane for Be at the left panel and W at the right panel with a $10cm^2$ beam impacting at (X,Y,Z)=(5,5,0) cm with 5 degrees impact angle with respect to the X direction. Reproduced from [8]

7.1.2 Parametric scan in the impact angle

In the previous subsection, a fixed impact angle was used to compare the ED profiles in Be and W and to underline the contribution of various electron transport mechanisms. However, electrons gyrate along magnetic field lines in plasma, resulting in the RE impacting the tile with different incident angles. While FLUKA does not offer an option to consider electron gyration, an analysis can be conducted to obtain ED profiles with varying impact angles to study their influence on the deposition pattern. In particular, the impact angle interval is [0,90] degrees.

As the impact angle increases, the maximum of the energy deposition curve decreases and shifts deeper into the material. This can be observed in Fig. 7.8 for Be, where the energy deposition curves are plotted for different angles over the full tile thickness in the left panel, and a zoom of the near-surface region is shown in the right panel. In contrast, in W, the maximum energy deposition initially increases until the angle of 45 degrees. Beyond this angle, the maximum decreases and shifts deeper into the material. This is shown in Fig. 7.9, which is the same as Fig. 7.8, but for W. In Be, a 90° angle causes the peak deposition to shift to 1 cm, whereas in W, the maximum is shifted to around 0.5 mm.

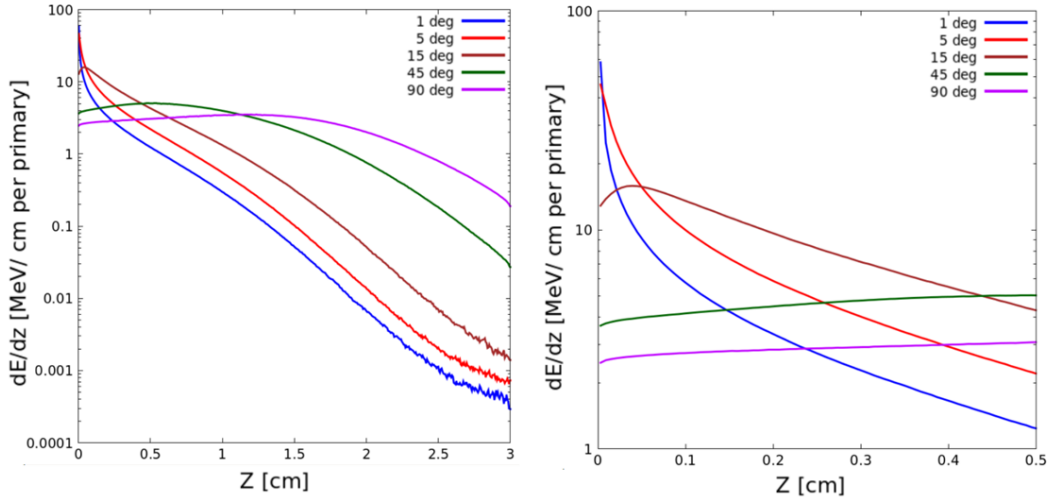


Fig. 7.8 1D projection of the ED in Be over the full thickness at the left panel and near the surface at the right panel for RE beam impact angles of 1 degree (blue curve), 5 degrees (red), 15 degrees (brown), 45 degrees (green) and 90 degrees (magenta). Reproduced from [8]

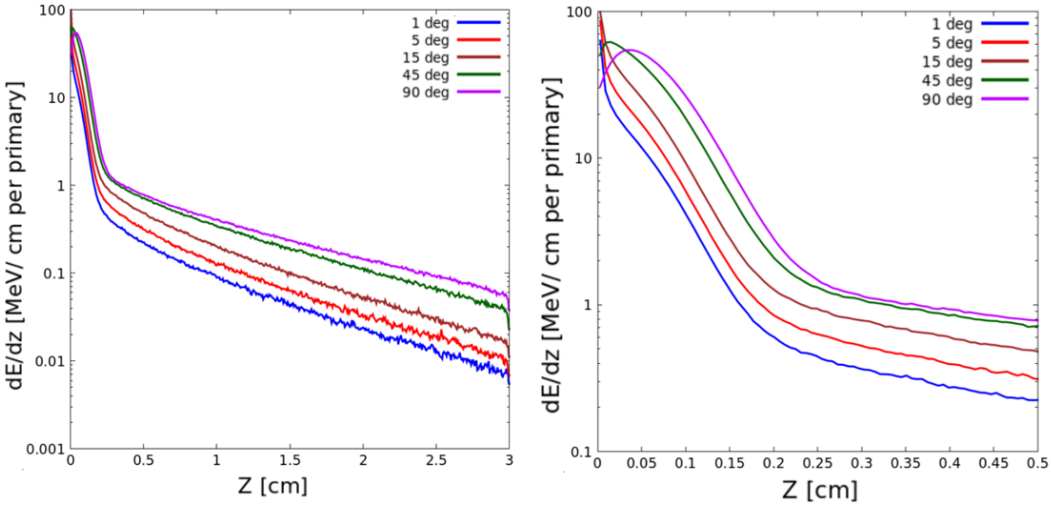


Fig. 7.9 1D projection of the ED in W over the full thickness at the left panel and near the surface at the right panel for RE beam impact angles of 1 degree (blue curve), 5 degrees (red), 15 degrees (brown), 45 degrees (green) and 90 degrees (magenta). Reproduced from [8]

The shift of the ED maximum for Be (and for W at higher angles) is attributed to the blob, representing the region where the energy deposition is the highest, around the initial direction of the RE beam. Precisely, at a 5° impact angle, the blob is symmetrically cut by the X-axis, leading to a monotonously decreasing ED profile,

Impact angle [deg]	E_C [MeV/cm3 primary]	E_W [MeV/cm3 primary]
1	2.60	1.93
5	4.19	2.80
10	5.34	3.49
15	6.01	4.06

Table 7.1 Energy deposited in C and W per primary electron at different beam incident angles. Reproduced from Ref. [8]

as observed in Figure 7.10. Conversely, at a 15° impact angle, the blob is entirely within the material, causing the maximum to shift to greater depths. Moreover, the reduction in the maximum is due to the inclination of the most intensive blob at a 15° angle, which now covers a larger area compared to the case where it is almost vertical with a 5° impact angle.

The average volumetric energy deposition increases as the impact angle increases because more electrons can penetrate the material, as reported in Tab. 7.1. This is due to a lower number of electrons being reflected from the surface, as demonstrated in Figure 7.11 for Be. Consequently, at 15°, Be exhibits a volumetric ED of around 6.30 MeV/cm^3 per primary, while W shows 4.06 MeV/cm^3 per primary.

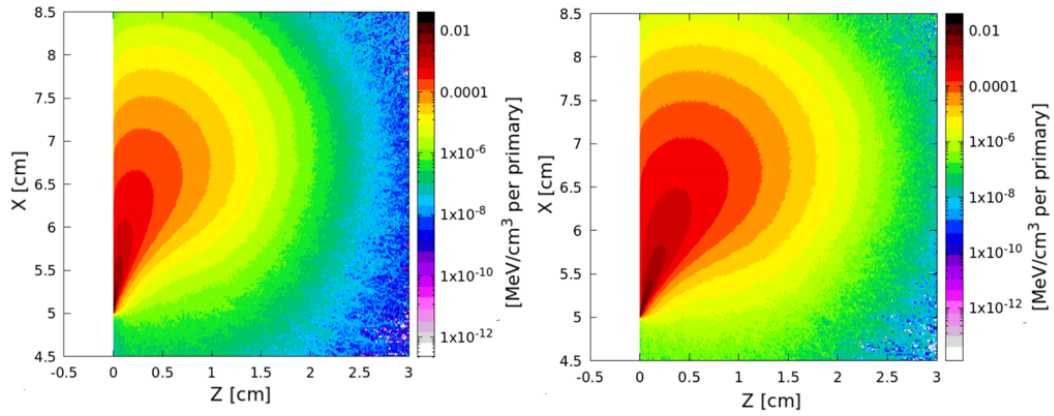


Fig. 7.10 2D projection of the ED on the XZ plane for Be with 5° at the left panel and with 15° at the right panel. Reproduced from [8]

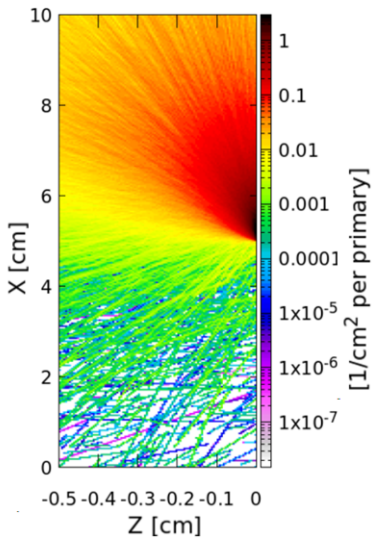


Fig. 7.11 2D projection of the electron fluence in the XZ plane for Be with 15° impact angle. Reproduced from [8]

7.2 Material thermal response to the RE beam impact

Once the model capability to adequately describe the involved physics was validated through the benchmark shown in the section 4.4, it was applied to simulate the thermal evolution of tiles under the effect of RE beams.

The energy deposition distributions obtained in section 7.1 using the FLUKA code were used as input to the thermal model, using the 5-degree square beam case as a reference scenario. The energy deposition distribution obtained with FLUKA is intrinsically 3D, depending on the beam geometry and inclination. However, based on what is reported below, it was demonstrated that a 2D model could be enough to assess the damage arising from possible material melting.

Indeed, comparing the duration of the RE impact (assumed to be approximately 100 ms in this study) and the characteristic time of the heat diffusion, $\tau = lw/\alpha$, (l is the length and w the width of the tile and α the thermal diffusivity), it is possible to realize that the latter is several order of magnitudes larger than the first one in the entire temperature range. The characteristic times of the heat diffusion for Be (left panel) and W (right panel) at different temperatures up to the melting are shown in Fig. 7.12.

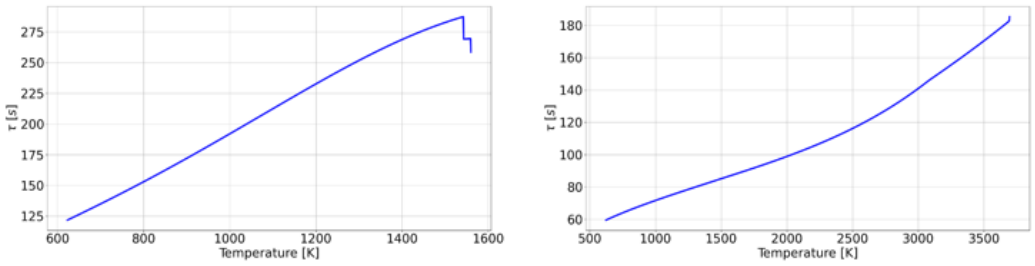


Fig. 7.12 Characteristic times of the heat diffusion for Be (left panel) and W (right panel) at different temperatures up to the melting. Reproduced from Ref. [8]

This means that the damage will be produced in a region extremely close to the beam contact area, and the diffusion will play a secondary role. According to this statement, in the case of a beam perpendicular to the tile, even a 1D model along the beam axis would be enough to estimate the melting thickness. To generalize the approach, a 2D model has been adopted to make it suitable for analyzing inclined beam effects and the beam boundary region in which some diffusion-related effects may be macroscopically detected.

7.2.1 Simulation setup

In the analyzed cases, with 10 cm^2 square 5 degrees inclined beam considered, the cutting plane was fixed at the beam centre parallel to the beam itself to appreciate the small inclination effect. The impacting beam is represented by an arrow in Fig. 7.13 with the impact area represented by the blue square and the cutting plane by the blue rectangle.

To obtain the power deposition distribution, the energy per unit volume, per unit particle computed by FLUKA, was multiplied by the number of involved particles (function of the RE beam current) and divided by the RE impact duration. The obtained distribution was considered the only driver of the problem, imposing adiabatic boundary conditions on the tile sides. Only the deposition duration was considered in the analysis since after that, the deposition drops to zero, and the recooling phase begins, meaning that the end of the disruption is the point at which significant damage is eventually produced on the tile.

The tile is initially considered at the uniform initial temperature $T_0 = 623$ K. Material properties were taken from [108] and [109] respectively for Tungsten

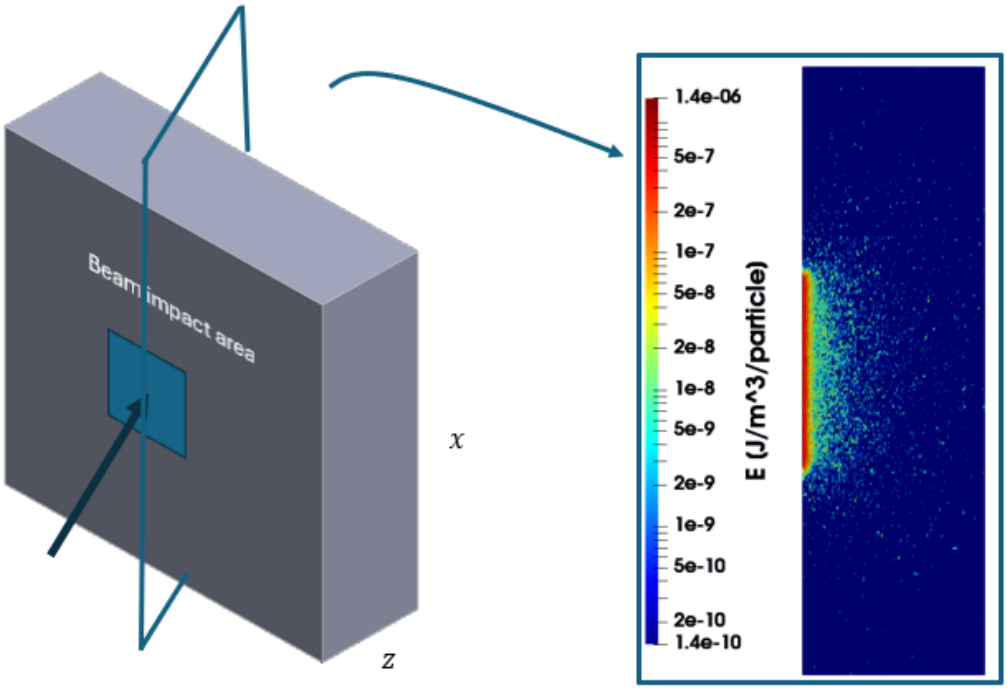


Fig. 7.13 Schematic representation of the tile with the RE beam (arrow) impacting at the centre with 10 cm^2 square area highlighted by the blue square. The results are shown on a cutting section (blue rectangle) parallel to the beam. Reproduced from Ref. [8]

and Beryllium. In table 7.2, the melting temperature and the latent heat of fusion considered in the analysis for both materials are reported.

Material	T_m **[K]**	Δh_f $\left[\frac{kJ}{kg}\right]$	ρ $\left[\frac{kg}{m^3}\right]$
Tungsten [108]	3695.0	271.98	19250.0
Beryllium [109]	1560.0	1643.8	1800.0

Table 7.2 Melting temperature, latent heat of fusion and density of the considered materials adopted in the simulation. Reproduced from Ref. [8]

The electron current was varied parametrically in the range of 100 - 500 kA while the event duration was fixed to 100 ms. Still, given the adiabatic condition considered and the energy deposition preserved, the discharge duration does not influence the damage to the tile. For this reason, all the results will be provided, normalizing the time on the discharge duration.

7.2.2 Thermal analysis results

The solid maximum temperature was analysed to monitor the thermal transient evolution since its evolution implicitly provides information on when the melting is, in case, started. Maximum solid temperature evolution is shown in Figure 7.14 for W (left panel) and Be (right panel) tiles, respectively, for RE current of 100 kA (blue curve), 200 kA (red curve), 300 kA (green curve), 400 kA (black curve) and 500 kA (magenta curve). As shown in the figure, W shows higher resistance to the beam exposure, reaching melting conditions only for currents larger than 200 kA. In contrast, Be approaches the melting temperature already with currents of the order of 100 kA. This difference in behaviour is linked to the material properties and the different interactions between the material and the electrons.

Indeed, with equation 7.1, it is possible to evaluate the amount of energy required to heat a material from T_0 to T_m and to complete the melting of a unit volume of material. This allows us to state that Tungsten requires almost double the energy of Beryllium to complete the process. The energy per cubic meter required to heat the material to the melting temperature and to complete the melting is reported in table 7.3.

$$E_m = \rho \cdot \left(\Delta h_f + \int_{T_0}^{T_m} c_p(T) dT \right) \tag{7.1}$$

Material	$\rho \cdot \int_{T_0}^{T_m} c_p(T)dT \left[\frac{GJ}{m^3}\right]$	$\rho \cdot \Delta h_f \left[\frac{GJ}{m^3}\right]$	$E_m \left[\frac{GJ}{m^3}\right]$
Tungsten	5.24	11.2	16.4
Beryllium	2.96	5.24	8.20

Table 7.3 Energy per unit volume to melt Tungsten and Beryllium (third column) given by the sum of the first two middle columns. Reproduced from Ref. [8]

Since Be is subjected to a higher energy deposition and is characterized by a lower energy per unit volume required to heat it to the melting, it is possible to conclude that the expected damage is larger in Beryllium than in Tungsten in the case of the same RE beam impacting the tile.

The tile damage is estimated by measuring the melting thickness at the center of the beam. This information is shown in figure 7.15 for W (blue curve) and Be (red curve) tile materials as a function of the beam RE current. The figure confirms that

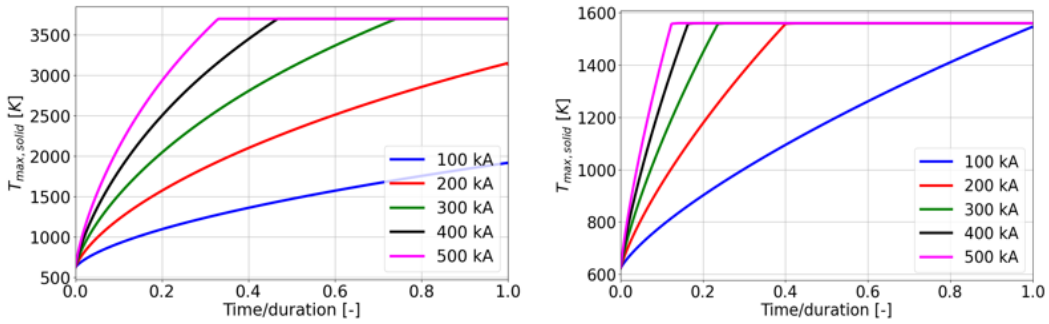


Fig. 7.14 Temporal evolution of the maximum solid temperature for W (left panel) and Be (right panel) at 100 kA (blue curve), 200 kA (red curve), 300 kA (green curve), 400 kA (black curve) and 500 kA (magenta curve) RE current Adapted from [8]

larger damage occurs in Be. The difference in damage can be seen in the temperature map in figure 7.16, which shows the location of the melting front after energy deposition at a beam current of 500 kA in W (left panel) and Be (right panel). The temperature map demonstrates that heat diffusion is slow compared to the duration of the energy deposition. The back of the tile, where power deposition is minimal, remains at the initial temperature, indicating that the deposited heat has not had enough time to diffuse to that location.

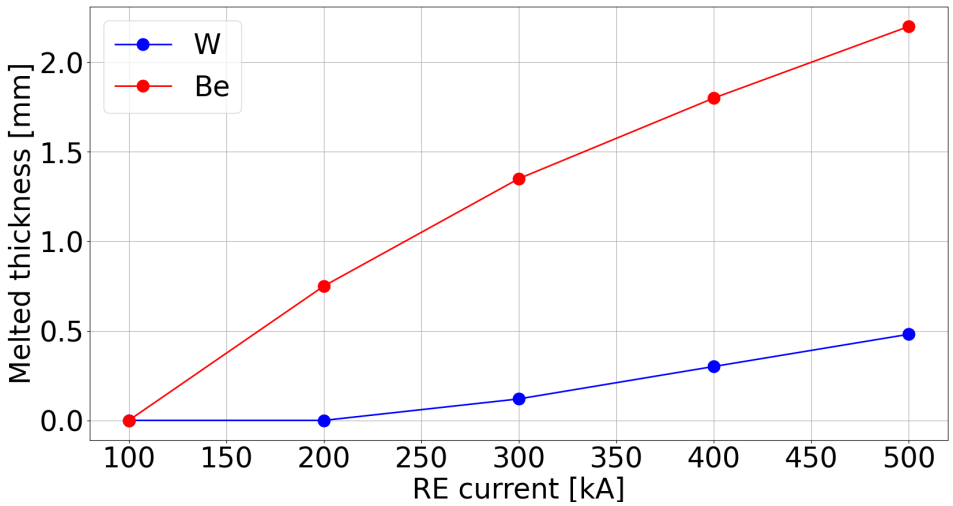


Fig. 7.15 Melted thickness as a function of the beam RE current for Be (red curve) and W (blue curve) tile materials. Reproduced from [8]

The negligible heat diffusion is further confirmed by the temperature profile plotted along a horizontal line passing through the centre of the beam in figure 7.17. This plot shows that beyond 1 cm of tile thickness, the temperature remains

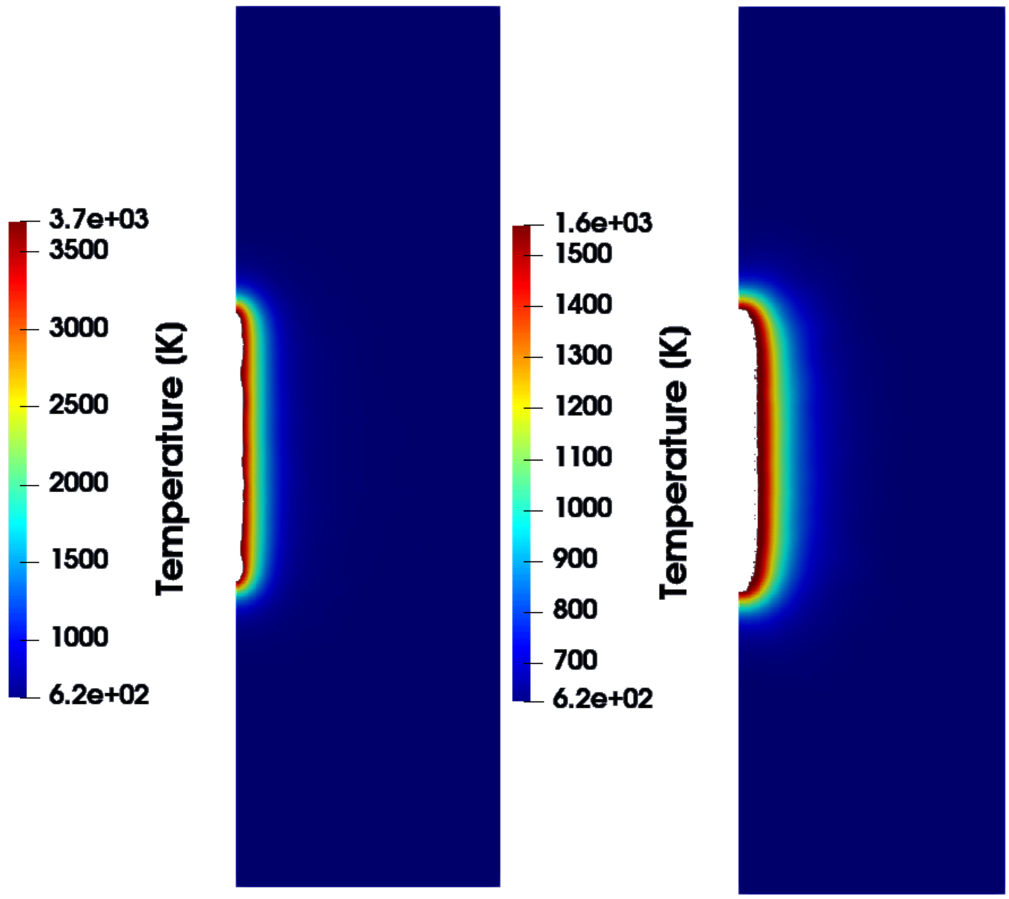


Fig. 7.16 Temperature map of the entire solid region at the end of the energy deposition for a beam current of 500 kA for Tungsten (left panel) and Be (right panel). Reproduced from [8]

unchanged from the initial temperature both for W (blue curve) and Be (red curve). Comparing the temperature profiles of the two materials helps us understand the qualitative difference in their energy absorption. Despite Tungsten reaching a higher peak temperature, the temperature of Be slowly decreases and becomes higher than W after the first few millimetres of thickness.

7.3 Conclusions

The assessment of the damage caused by a 7 MeV RE beam in fusion reactor FW materials such as Beryllium and Tungsten was carried out in this work. For this aim, FLUKA and FreeFEM++ simulation tools were used. In particular, FLUKA was used to compute the energy deposition profiles caused by the impact of a RE beam

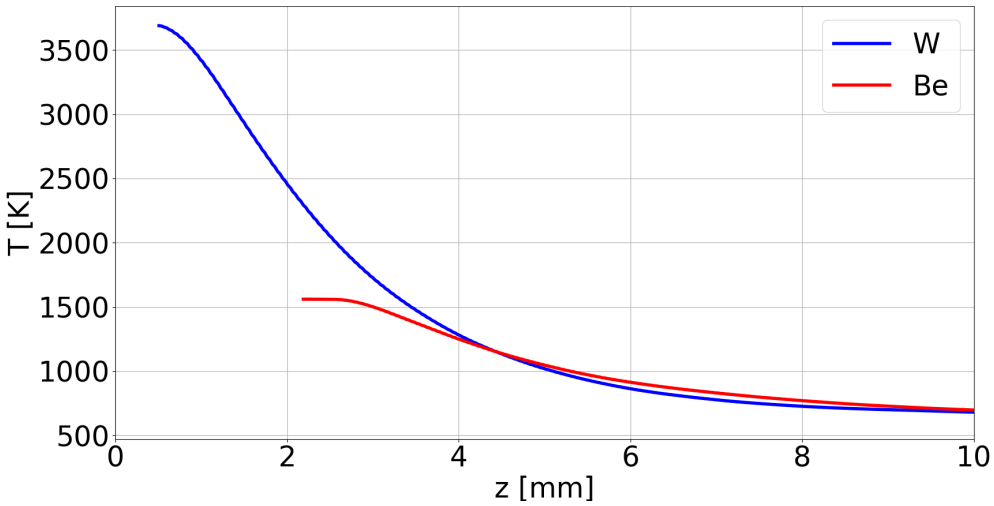


Fig. 7.17 Temperature profile within the solid domain for both Tungsten (blue curve) and Beryllium(red curve) in case of a 500 kA beam current. Only the first 10 mm of the total thickness are shown here, where relevant gradients can be observed. Reproduced from [8]

on generic Tokamak first wall tiles and the apparent heat capacity (AHC) formulation was implemented and benchmarked using FreeFem++ to assess the thermal response of the material. The AHC method was successfully validated through a benchmark problem. Afterwards, the model was used to compute the temperature and melting front evolution using the ED profiles from FLUKA as an input.

The study considered realistic energy distribution functions for Be and W materials, taking into account two different tile sizes. It assumed a point beam with an impact angle of 5 degrees to examine the effects of three transport mechanisms: elastic scattering, delta-ray production, and Bremsstrahlung. W is characterized by a higher stopping power than Be due to its high atomic number (Z). Consequently, in W a significant fraction of energy is deposited near the surface, where elastic scattering and delta-ray production play dominant roles. Furthermore, the study looked into the dynamics of photon transport by disabling Bremsstrahlung.

The energy deposited by photons becomes dominant near the opposite border of the Beryllium tile. In contrast, in Tungsten, photons become the main energy carrier after a few millimetres. This switch from electrons to photons significantly changes the energy deposition pattern. Photons, with their high radiation length, can carry their energy deeper into the material. Therefore, even though the deposited energy decreases rapidly near the surface of tungsten, it is higher than beryllium in terms of MeV/cm per primary electron, far from the surface. Since W is characterized by

good thermal properties, the penetration of photons may not be dramatic for this material. However, photons can affect other structural materials which are located beyond the initial tungsten protection.

Moreover, with increasing impact angles, the RE beam was observed to penetrate deeper into the material in Be while conserving a substantial amount of its initial energy. In W, this pattern is observed for a higher impact angle.

The thermal response of the material to the RE beam impact was analyzed through a 10x10 cm square RE beam with a 5-degree impact angle. This analysis confirmed W capability to limit the melting front to the near-surface region where a significant amount of energy is deposited. Moreover, a higher RE current is needed for W than for Be to initiate tile melting due to a higher energy required to heat a unit volume to the melting temperature in the case of W.

The thermal investigation was focused on assessing the most severe damage occurring to the wall during the RE impact. This approach allowed to adopt a 2D approximation of the problem since the heat diffusion is characterized by large time scales in comparison to the assumed duration of the RE impact. Nevertheless, after the impact, heat would slowly diffuse into the material. The high melting temperature of W causes heat to diffuse deeper into the material, while Be, with its low melting temperature, experiences limited heat diffusion due to the material's melting and evaporation processes. This challenges a thin W layer, as the interface between this layer and other structural materials would experience higher temperatures.

In the future, the thermal tool will be enhanced to address the issue through parallelization. This will enable the modeling of more complex beams and 3D geometries by increasing the number of degrees of freedom considered.

Chapter 8

Conclusions

The results obtained in this study highlight the importance of investigating the stability of a post-disruptive plasma in the presence of an RE current and its impact on the Tokamak FW.

The investigation first focused on the nonlinear evolution of tearing instabilities influenced by RE current and electron inertia. This analysis revealed that the RE microlayer width plays a crucial role in driving the transition of runaway current into the nonlinear phase. Once the island size surpasses this microlayer width, RE current enters the nonlinear phase and form a spiral-like structure within the island, fundamentally altering their distribution. Electron inertia, represented through the electron skin depth d_e, was found to shape the thermal current by concentrating it in thin spiral formations within the magnetic island. In plasmas with lower resistivity and more realistic RE speeds ($c/v_A \gg 10$), such structures could introduce significant gradients in the plasma overall behavior. However, a precise characterization of this behavior requires an exceedingly fine spatial resolution, which will be the subsequent focus of this research.

Magnetic stochasticity also emerged as a key element in RE dynamics. The presence of multiple magnetic islands results in magnetic field stochastization that mitigates runaway currents. This phenomenon, observed experimentally in JET experiment #95135, was simulated as part of this study, modeling benign RE termination. Our analysis showed that resistivity plays a pivotal role in governing magnetic stochasticity and RE loss rates. At higher resistivities ($\eta \geq 6 \times 10^{-5} \Omega m$, RE current losses are driven predominantly by the growth of dominant double tearing

modes, leading to a strong core stochastization. This stochastization drives RE out of the plasma quickly, resulting in a low remaining RE current. Lower resistivities reduce this stochastization, slowing RE losses but prolonging the stochastic phase.

When resistivity falls below the above threshold, secondary modes assume a more significant role, generating bursts of stochastization that hasten RE losses. This process reveals that, while RE amplitude loss are similar in all cases, the wetted area of the RE current impact differs considerably with the level of magnetic stochasticity. Higher stochasticity broadens the RE impact area, resulting in a more diffuse and less concentrated interaction with the FW, which is beneficial for managing RE termination.

The next stage of the analysis moves from the RE dynamics to their effects on the Tokamak structural materials, particularly on tungsten (W) and beryllium (Be) components of the FW. The energy deposition profiles showed that, due to its high atomic number, W absorbs a large fraction of energy near the surface through elastic scattering and delta-ray production. Photons in W, however, become primary energy carriers shortly after penetrating the surface and, due to their high radiation length, transport energy deep into the material. This photon penetration can impact the structural materials. Be, conversely, absorbs less energy at the surface due to its lower atomic number but faces a different set of thermal challenges due to its lower melting point. The angle at which RE impact these materials also significantly influences damage potential. As the impact angle increases, RE penetration and energy deposition in the material intensify, amplifying damage.

The thermal analysis showed that W can limit the melting front to the near-surface region where a significant amount of energy is deposited. However, the high melting temperature of W causes heat to diffuse deeper into the material, while Be, with its low melting temperature, experiences limited heat diffusion due to the material melting and evaporation processes. This challenges a thin W layer, as the interface between this layer and other structural materials would experience higher temperatures.

Looking ahead, this research will focus on enhancing the thermal tool through parallelization to simulate complex RE beams and model 3D geometries with greater detail. This development would allow a more integrated approach to RE termination modeling, directly linking RE termination in the plasma core with its impact on the

FW. Such integration is essential for advancing RE studies, ensuring we can predict and manage RE effectively in future fusion reactors.

Acronyms

AHC apparent heat capacity

Ar Argon

Be Beryllium

CL connection length

CQ current quench

CSDA continuous slowing-down approximation

DMS disruption mitigation system

DTM double tearing mode

ED energy deposition

FFT Fast Fourier transform

FW First Wall

GS Grad-Shafranov

HXR Hard X-ray

IR Infrared

MA mega Ampere

MGI massive gas injection

MHD magnetohydrodynamic

MR magnetic reconnection

Ne Neon

PFC Plasma Facing Components

RE runaway electrons

REMC runaway electron mitigation coli

RMHD reduced magnetohydrodynamics

RMP resonant magnetic perturbation

RR Rechester-Rosenbulth

SPI Shattered Pellet Injection

TQ thermal quench

VDE vertical displacement event

W Tungsten

References

[1] M.N. Rosenbluth and S.V. Putvinski. Theory for avalanche of runaway electrons in Tokamaks. *Nucl. Fusion*, 37:1355, 1997.

[2] Eurofusion Community. European Research Roadmap to the Realisation of Fusion Energy. 2018.

[3] P. Helander, D. Grasso, R.J. Hastie, and A. Perona. Resistive stability of a plasma with runaway electrons. *Phys. Plasmas*, 14:122102, 2007.

[4] C. Liu, C. Zhao, S.C. Jardin, A. Bhattacharjee, and et al. Structure and overstability of resistive modes with runaway electrons. *Phys. Plasmas*, 27:092507, 2020.

[5] V. Bandaru, M. Hoelzl, C. Reux, O. Ficker, and et al. Magnetohydrodynamic simulations of runaway electron beam termination in JET. *Plasma Phys. Control. Fusion*, 63:035024, 2021.

[6] D. Grasso, D. Borgogno, L. Singh, and F. Subba. Stability of a weakly collisional plasma with runaway electrons. *Journal of Physics: Conference Series*, 2397:012004, 2022.

[7] L. Singh, D. Borgogno, F. Subba, and D. Grasso. Post-disruption reconnection event driven by a runaway current. *Phys. Plasmas*, 30:122114, 2023.

[8] L. Singh and M. De Bastiani and R. Bonifetto and F. Subba and et al . Assessment of the runaway electrons induced damage to the tokamak first wall. *Journal of Nuclear Materials*, submitted.

[9] H. Knoepfel and D.A. Spong. Runaway electrons in toroidal discharges. *Nucl. Fusion*, 19:785, 1979.

[10] B.N. Breziman, P. Aleynikov, E.M. Hollmann, and M. Lehnen. Physics of runaway electrons in Tokamak. *Nucl. Fusion*, 59:083001, 2019.

[11] M. Hoppe. *Runaway-electron model development and validation in tokamaks*. PhD thesis, Department of Physics, Chalmers University of Technology, Goteborg, 2021.

[12] A.H. Boozer. Theory of Tokamak disruptions. *Phys. of Plasmas*, 19 (5):058101, 2012.

[13] A. N. James. *Investigations of runaway electron generation, transport, and stability in the DIII-D tokamak*. PhD thesis, University of California , San Diego, 2011.

[14] Y.A. Sokolov. Multiplication of accelerated electrons in a Tokamak. *JETP Letters*, 29:2018–221, 1979.

[15] L. Hesslow. *Effect of Partial Screening on Runaway-Electron Dynamics*. PhD thesis, Department of Physics, Chalmers University of Technology, Goteborg, 2018.

[16] H. M. Smith and E. Verwichte. Hot tail runaway electron generation in tokamak disruptions. *Phys. Plasmas*, 15:072502, 2008.

[17] J.R. Martin-Solis, A. Loarte, and M. Lehnen. Formation and termination of runaway beams in ITER disruptions. *Nucl. Fusion*, 57:066025, 2017.

[18] H. Dreicer. Electron and Ion Runaway in a Fully Ionized Gas. I. *Physical Review*, 115, 1959.

[19] L. Hesslow, L. Unnerfelt, O. Vallhagen, O. Embreus, M. Hoppe, G. Papp, and T. Fülöp. Evaluation of the Dreicer runaway generation rate in the presence of high-Z impurities using a neural network. *Journal of Plasma Physics*, 85:475850601, 2019.

[20] J.W. CONNOR and R.J. HASTIE. Relativistic limitations on runaway electrons. *Nucl. Fusion*, 15, 1975.

[21] L. Hesslow, O. Embreus, G.J. Wilkie, G. Papp, and T. Fülöp. Effect of partially ionized impurities and radiation on the effective critical electric field for runaway generation. *Plasma Phys. Control. Fusion*, 60:074010, 2018.

[22] H.H. Fleischmann R. Jayakumar and S.J. Zweben. Collisional avalanche exponentiation of runaway electrons in electrified plasmas. *Physics Letters A*, 172:447–451, 1993.

[23] L. Hesslow, O. Embreus, A. Stahl, T.C. DuBois, G. Papp, S.L. Nwton, and T. Fülöp. Effect of partially screened nuclei on fast-electron dynamics. *Phys. Rev. Let.*, 118:255001, 2017.

[24] L. Hesslow, O. Embreus, M. Hoppe, T.C. DuBois, G. Papp, M. Rahm, and T. Fülöp. Generalized collision operator for fast electrons interacting with partially ionized impurities. *J. Plasma Phys.*, 84:905840605, 2018.

[25] V. Bandaru and M. Hoelzl. Report for task D1.1: Code optimization. Technical report, Max Planck Institute for Plasma Physics, Boltzmannstr. 2, 85748 Garching b. M., Germany, 2020.

[26] F. Andersson, P. Helander, and L.G. Eriksson. Damping of relativistic electron beams by synchrotron radiation. *Phys. Plasmas*, 8, 2001.

[27] M. Hoppe, O. Embreus, C. Paz Soldan, R.A. Moyer, and T. Fülöp. Interpretation of runaway electron synchrotron and bremsstrahlung images. *Nucl. Fusion*, 58:082001, 2018.

[28] M. Hoppe, O. Embreus, R.A. Tinguely, R.S. Granetz, A. Stahl, and T. Fülöp. SOFT: a synthetic synchrotron diagnostic for runaway electrons. *Nucl. Fusion*, 58:026032, 2018.

[29] M. Bakhtiari, G.J. Kramer, M. Takechi, H. Tamai, Y. Miura, Y. Kusama, and Y. Kamada. Role of Bremsstrahlung Radiation in Limiting the Energy of Runaway Electrons in Tokamaks. *Phys. Rev. Let.*, 94:215003, 2005.

[30] M. Bakhtiari, Y. Kawano1, H. Tamai1, Y. Miura1, R. Yoshino1, and Y. Nishida. Fast plasma shutdown scenarios in the JT-60U tokamak using intense mixed gas puffing. *Nucl. Fusion*, 42:1197–1204, 2002.

[31] A. Stahl, E. Hirvijoki, J. Decker, O. Embreus, and T. Fülöp. Effective Critical Electric Field for Runaway-Electron Generation. *Phys. Rev. Let.*, 114:115002, 2015.

[32] G. Papp, M. Drevlak, G.I Pokol, and T. Fulop. Energetic electron transport in the presence of magnetic perturbations in magnetically confined plasmas. *J. Plasma Phys.*, 81:475810503, 2015.

[33] L. Zeng, H.R. Koslowski, Y. Liang, A. Lvovskiy, M. Lehnen, D. Nicolai, J. Pearson, M. Rack, H. Jaegers, K.H. Finken, K. Wongrach, Y. Xu, and the TEXTOR team. Experimental Observation of a Magnetic-Turbulence Thresholdfor Runaway-Electron Generation in the TEXTOR Tokamak. *Phys. Rev. Let.*, 110:235003, 2013.

[34] P. Helander, L.-G. Eriksson, and F. Andersson. Suppression of runaway electron avalanches by radial diffusion. *Phys. Plasmas*, 7:4106, 2000.

[35] G Papp, M Drevlak, T.Fulop, P. Helander, and et al. Runaway electron losses caused by resonant magnetic perturbations in ITER. *Plasma Phys. Control Fusion*, 53:095004, 2011.

[36] H.-W. Bartels. Impact of runaway electrons. *Fusion Engineering and Design*, 23:323–328, 1993.

[37] V.P. Budaeva, Yu.V. Martynenkoa, S.A. Grashina, R.N. Giniyatulinc, and et al. Tungsten melting and erosion under plasma heat load in tokamak discharges with disruptions. *Nuclear Material and Energy*, pages 1–5, 2016.

[38] R. Granetz, D.G. Whyte, V.A. Izzo, T. Biewer, and et al. Gas jet disruption mitigation studies on Alcator C-Mod. *Nucl. Fusion*, 46:1001–1008, 2006.

[39] M. Bakhtiari, H. Tamai, Y. Kawano, G.J. Kramer, and et al. Study of plasma termination using high-Z noble gas puffing in the JT-60U tokamak. *Nucl. Fusion*, 45:318–325, 2005.

[40] M. Lehnen, K. Aleynikova, P.B. Aleynikov, D.J. Campbell, and et al. Disruptions in ITER and strategies for their control and mitigation. *Journal of Nuclear Materials*, pages 39–48, 2015.

[41] G. Pautasso, D. Coster, T. Eich, J.C. Fuchs, and et al. Disruption studies in ASDEX Upgrade in view of ITER. *Plasma Phys. Control. Fusion*, 51:124056, 2009.

[42] S.A. Bozhenkov, M. Lehnen, K.H. Finken, M.W. Jakubowski, and et al. Generation and suppression of runaway electrons in disruption mitigation experiments in TEXTOR. *Plasma Phys. Control. Fusion*, 50:105007, 2008.

[43] C. Reux, J. Bucalossi, F. Saint-Laurent, and C. Gil. Experimental study of disruption mitigation using massive injection of noble gases on Tore Supra. *Nucl. Fusion*, 50:95006, 2010.

[44] Y. Li, Z.Y. Chen, W. Yan, Y.N. Wei, and et al. Comparison of disruption mitigation from shattered pellet injection with massive gas injection on J-TEXT. *Nucl. Fusion*, 61:126025, 2021.

[45] R. Sweeney, A.J. Creely, J. Doody, T. Fülöp, and et al. MHD stability and disruptions in the SPARC tokamak. *J. Plasma Phys.*, 86:865860507, 2020.

[46] N. Commaux, L.R. Baylor, S.K. Combs, N.W. Eidietis, and et al. Novel rapid shutdown strategies for runaway electron suppression in DIII-D. *Nucl. Fusion*, 51:103001, 2011.

[47] V.A. Izzo, I. Pusztai, K. Särkimäki, A. Sundström, and et al. Runaway electron deconfinement in SPARC and DIII-D by a passive 3D coil. *Nucl. Fusion*, 62:096029, 2022.

[48] R. Yoshino and S. Tokuda. Runaway electrons in magnetic turbulence and runaway current termination in tokamak discharges. *Nucl. Fusion*, 40:1293, 2000.

[49] M. Lehnen, S.A. Bozhenkov, S.S. Abdullaev, M.W. Jakubowski, and et al. Suppression of Runaway Electrons by ResonantMagnetic Perturbations in TEXTOR Disruptions. *Phys. Rev. Let.*, 100:255003, 2008.

[50] R. Yoshino and S. Tokuda. On the minimum transport required to passively suppress runaway electrons in SPARC disruptions. *Plasma Phys. Control. Fusion*, 65:034002, 2023.

[51] P.B. Aleynikov, A.A. Ivanov, R.R. Khayrutdinov1, S.V. Konovalov, and et al. Simulations of Runaway Electrons in ITER, in: Proceedings of the 37th EPS Conference on Plasma Physics, P1.1004., Dublin, Ireland. 2010.

[52] G Papp, M Drevlak, T.Fulop, and G.I. Pokol. The effect of resonant magnetic perturbations on runaway electron transport in ITER. *Plasma Phys. Control Fusion*, 54:125008, 2012.

[53] A.H. Boozer. Two beneficial non-axisymmetric perturbations to tokamaks. *Plasma Phys. Control. Fusion*, 53:084002, 2011.

[54] H. M. Smith, A.H. Boozer, , and P. Helander. Passive runaway electron suppression in tokamak disruptions. *Phys. Plasmas*, 20:072505, 2013.

[55] F. Maviglia, C. Bachmann, G. Federici, T. Franke, and et al. Integrated design strategy for EU-DEMO first wall protection from plasma transients. *Fusion Engineering and Design*, 177:113067, 2022.

[56] J.H. You, C. Bachmann, V.G. Belardi, M. Binder, and et al. Limiters for DEMO wall protection: Initial design concepts technology options . *Fusion Engineering and Design*, 174:112988, 2022.

[57] M.L. Richiusa, A. Cardella, A. Cufar, A. Froio, and et al. The integrated engineering design concept of the upper limiter within the EU-DEMO LIMITER system. *Fusion Engineering and Design*, 202:114329, 2024.

[58] C. Paz-Soldan, N. W. Eidietis, Y.Q. Liu, D. Shiraki, and et al. Kink Instabilities of the Post-Disruption Runaway Electron Beam at Low Safety Factor. *Plasma Phys. Control. Fusion*, 61:054001, 2019.

[59] C. Reux, C. Paz-Soldan, P. Aleynikov, V. Bandaru, and et al. Demonstration of Safe Termination of Megaampere Relativistic Electron Beams in Tokamaks. *Phys. Rev. Let.*, 126:175001, 2021.

[60] G. Bateman. *MHD instabilites*. The MIT Press, 1978.

[61] L.G. Eriksson, P. Helander, F. Andersson, D. Anderson, and et al. Current Dynamics during Disruptions in Large Tokamaks. *Phys. Rev. Let.*, 92:205004, 2004.

[62] G. Colonna and A. D'Angola. *Plasma Modeling*. 2053-2563. IOP Publishing, 2016.

[63] R.D. Hazeltine, M. Kotschenreuther, and P.J. Morrison. A four-field model for tokamak plasma dynamics. *Phys. Fluids*, 28:8, 1985.

[64] E. Nardon, V. Bandaru, M. Hoelzl, F.J. Artola, and et al. Non-linear dynamics of the double tearing mode. *Phys. Plasmas*, 30:092502, 2023.

[65] M. Ottaviani and F. Porcelli. Nonlinear collisionless magnetic reconnection. *Phys. Rev. Lett.*, 71:3802, 1993.

[66] D. Biskamp. *Magnetic Reconnection in Plasmas*. Cambridge Monographs on Plasma Physics. Cambridge University Press, 2000.

[67] E.G. Harris. On a plasma sheath separating regions of oppositely directed magnetic field. *Nuovo Cim*, 23:115–121, 1962.

[68] C. Chiuderi and M. Velli. *Fisica del Plasma*. UNITEXT. Springer, 2012.

[69] H.P. Furth, J. Killen, and M.N. Rosenbluth. Finite-Resistivity Instabilities of a Sheet Pinch. *Phys. Fluid*, 6:459, 1963.

[70] M. Ottaviani F. Militello, G. Huysmans and F. Porcelli. Effects of local features of the equilibrium current density profile on linear tearing modes. *Phys. Plasmas*, 11:125, 2004.

[71] P.H. Rutherford. Non linear growth of the tearing mode. *Phys. Fluids*, 16:1903, 1973.

[72] F. Porcelli D. Borgogno, D. Grasso, F. Califano, and et al. Aspects of three-dimensional magnetic reconnection. *Phys. Plasmas*, 12:032309, 2005.

[73] F. Pegoraro D. Borgogno, D. Grasso and T.J Schep. Barriers in the transition to global chaos in collisionless magnetic reconnection. I. Ridges of the finite time Lyapunov exponent field. *Phys. Plasmas*, 18:102307, 2011.

[74] S. Abdullaev. *Magnetic Stochasticity in Magnetically Confined Fusion Plasmas*. Springer Series on Atomic, Optical, and Plasma Physics 78. Springer, 2014.

[75] P. Maget, G. T. A. Huysmans, X. Garbet, M. Ottaviani, and et al. Nonlinear magnetohydrodynamic simulation of Tore Supra hollow current profile discharges. *Phys. Plasmas*, 14:052509, 2007.

[76] C. Reux, C. Paz-Soldan, N. Eidietis, M. Lehnen, and et al. Physics of runaway electrons with Shattered Pellet Injection at JET. *Plasma Phys. Control. Fusion*, 64, 2022.

[77] K. Särkimäki, E. Hirvijoki, J. Decker, J. Varje, and et al. An advection–diffusion model for cross-field runaway electron transport in perturbed magnetic fields. *Plasma Phys. Control. Fusion*, 58:125017, 2016.

[78] E.M. Hollmann, I. Bykov, N.W. Eidietis, J.L. Herfindal, and et al. Study of argon expulsion from the post-disruption runaway electron plate following low-Z massive gas injection in DIII-D. *Phys. Plasmas*, 27:042515, 2020.

[79] A. Loarte, V. Riccardo, J.R. Martin-Solin, J. Paley, and et al. Magnetic energy flows during the current quench and termination of disruptions with runaway current plateau formation in JET and implications for ITER. *Nucl. Fusion*, 51:073004, 2011.

[80] M. Hoelzl, G.T.A Huijsmans, S.J.P. Pamela, M. Becoulet, and et al. The JOREK non-linear extended MHD code and applications to large-scale instabilities and their control in magnetically confined fusion plasmas. *Nucl. Fusion*, 61:065001, 2021.

[81] A. Ferrari, P.R Sala, R. Guaraldi, and F. Padoani. An improved multiple scattering model for charged particle transport. *Nuclear Instruments and Methods in Physics*, 71:412, 1992.

[82] F. Hecht. New development in freefem++. *J. Numer. Math.*, 20:251, 2012.

[83] S.K. Lele. Compact Finite Difference Schemes with Spectral-like Resolution. *J. Comput. Phys.*, 103:16, 1992.

[84] Francisco Artola Such. *FREE-BOUNDARY SIMULATIONS OF MHD PLASMA INSTABILITIES IN TOKAMAKS*. PhD thesis, Université Aix Marseille, 2018.

[85] J.P. Goedbloed, R. Keppens, and S. Poedts. *Advanced magnetohydrodynamics: with applications to laboratory and astrophysical plasmas*. Cambridge University Press, 2010.

[86] A. Ferrari, J. Ranft, P.R. Sala, and A. Fassò. *FLUKA: A multi-particle transport code (Program version 2005)*.

[87] S. M. Seltzer L. Kim, R. H. Pratt and M. J. Berger. Ratio of positron to electron bremsstrahlung energy loss: An approximate scaling law. *Phys. Rev. A*, 33:3002, 1986.

[88] Stopping powers and range tables for electrons. https://physics.nist.gov/PhysRefData/Star/Text/ESTAR.html. Accessed: 2023-07-27.

[89] M. Zerroukat and C.R. Chatwin. *Computational Moving Boundary Problems*. Research Studies Press LTD, Taunton, Somerset, England, 1964.

[90] R.S. Gupta and D. Kumar. Variable time step methods for one-dimensional Stefan problem with mixed boundary condition. *International Journal of Heat and Mass Transfer*, 24(2):251–259, 1981.

[91] J. Caldwell, S. Savovic, and Y.Y. Kwan. Nodal integral and finite difference solution of one-dimensional Stefan problem. *J. Heat Transfer*, 125(3):523–527, 2003.

[92] J. Caldwell and Y.Y. Kwan. Numerical methods for one-dimensional Stefan problems. *Communications in numerical methods in engineering*, 20(7):535–545, 2004.

[93] M.L. Richiusa, P. Ireland, F. Maviglia, J. Nicholas, and et al. Advances in material phase change modelling approach for EU-DEMO limiter's plasma-facing components. *Fusion Engineering and Design*, 189:113477, 2023.

[94] *COMSOL Documentation. Version 6.1 - Heat Transfer Module User's Guide*.

[95] F. Porcelli. Collisionless m=1 tearing mode. *Phys. Rev. Lett.*, 66:425, 1991.

[96] W. Daughton, V. Roytershteyn, H. Karimabadi, L. Yin, and et al. Role of electron physics in the development of turbulent magnetic reconnection in collisionless plasmas. *Nature Physics*, 7:539, 2011.

[97] D. Grasso, D. Borgogno, E. Tassi, and A. Perona. Asymmetry effects driving secondary instabilities in two-dimensional collisionless magnetic reconnection. *Phys. Plasmas*, 27:012302, 2020.

[98] N.F. Loureiro, S.C. Cowley, W.D. Dorland, M.G. Haines, and et al. X-Point Collapse and Saturation in the Nonlinear Tearing Mode Reconnection. *Phys. Rev. Lett.*, 95:235003, 2005.

[99] V. Bandaru, M. Hoelzl, F.J. Artola, G. Papp, and et al. Simulating the nonlinear interaction of relativistic electrons and tokamak plasma instabilities: Implementation and validation of a fluid model. *Phys. Rev. E*, 99:063317, 2019.

[100] A. H. Boozer. Flattening of the tokamak current profile by a fast magnetic reconnection with implications for the solar corona. *Phys. Plasmas*, 27:102305, 2020.

[101] D.C. Van Vugt. *Nonlinear coupled MHD-kinetic particle simulations of heavy impurities in tokamak plasmas*. PhD thesis, Eindhoven University of Technology, 2019.

[102] X. Tao, A. A. Chan, and Al. J. Brizard. Hamiltonian theory of adiabatic motion of relativistic charged particles. *Phys. Plasmas*, 14:9, 2007.

[103] Yu. Igitkhanov and B. Bazylev. The PFC Erosion in DEMO due to Runaway Electrons. *Fusion Science and Technology*, 60(1):349–353, 2011.

[104] Yu. Igitkhanov, B. Bazylev, and I. Landman. Calculation of runaway electrons stopping power in ITER. *Journal of Nuclear Materials*, 415:S845–S848, 2011.

[105] G. Maddaluno, G. Maruccia, M. Merola, and S. Rollet. Energy deposition and thermal effects of runaway electrons in ITER-FEAT plasma facing components. *Journal of Nuclear Materials*, 313-316:651–656, 2003.

[106] Ondrej Ficker. Private comunication. 2022.

[107] C. Reux, V. Plyusnin, B. Alper, D. Alves, and et al. Runaway electron beam generation and mitigation during disruptions at JET-ILW. *Nucl. Fusion*, 55:093013, 2015.

[108] P. Tolias, EUROfusion MST1 Team, and et al. Analytical expressions for thermophysical properties of solid and liquid tungsten relevant for fusion applications. *Nuclear materials and energy*, 13:42–57, 2017.

[109] P. Tolias. Analytical expressions for thermophysical properties of solid and liquid beryllium relevant for fusion applications. *Nuclear Materials and Energy*, 31:101195, 2022.